ANISOTROPIC AND HYPERBOLIC METAMATERIALS IN THE CYLINDRICAL GEOMETRY

A Thesis Submitted
in Partial Fulfilment of the Requirements
for the Degree of
Doctor of Philosophy

by
DHEERAJ PRATAP

to the
DEPARTMENT OF PHYSICS
INDIAN INSTITUTE OF TECHNOLOGY KANPUR
September 2015

To My Parents

STATEMENT

I hereby declare that the matter manifested in this thesis entitled ***"Anisotropic and Hyperbolic Metamaterials in the Cylindrical Geometry"***, is the result of research carried out by me in the Department of Physics, Indian Institute of Technology Kanpur, India under the supervision of Prof. S. Anantha Ramakrishna.

In keeping with the general practice of reporting scientific observations, due acknowledgement has been made wherever the work described is based on the findings of other investigators.

Dheeraj Pratap

Dheeraj Pratap
Y9109063
Department of Physics
I.I.T. Kanpur

September, 2015

CERTIFICATE

It is certified that the work contained in the thesis entitled ***"Anisotropic and Hyperbolic Metamaterials in the Cylindrical Geometry"*** by ***Dheeraj Pratap***, has been carried out under my supervision and that this work has not been submitted elsewhere for a degree.

S. Anantha Ramakrishna

Prof. S. Anantha Ramakrishna
Department of Physics
I.I.T. Kanpur

September, 2015

Acknowledgments

It has been long time of six years since I started my thesis work. Over this long period of time, my experiences and associations are innumerable and now that I am writing, I want to use this occasion to express my sincere thanks to all those who have supported and helped me in this endeavor.

First and foremost, I would like to express my gratitude to my thesis supervisor Prof. S. Anantha Ramakrishna for providing me the opportunity to work under his guidance and for his continuous support and encouragement throughout the research work. It is he who introduced me to various issues explored in this thesis work, in particular, his simplifying but systematic approach towards the cylindrical metamaterial problems has motivated me a lot.

I thank my collaborators Dr. Ashwin K. Iyer of University of Alberta, Canada for his continuous support and discussion on the waveguide problems, and Prof. Sameer Khandekar of IIT Kanpur, India for his support and thermal problems.

I am also grateful to Prof. H. Wanare and Prof. R. Vijaya for their invaluable comments and suggestions during the semester evaluation of my thesis work. I am also thankful to Prof. Sutapa Mukherjee, Prof. V. Subramanium and Prof. Avinash Singh for teaching various foundation and advanced topics during the course work.

I acknowledge to Dr. Chandan Srivastava and his students Rohit and Mahander of IISc Bangalore to help me for the nanowires deposition. I thank Mechanical Engineering, BSBE, Nanoscience Center, ACMS of IIT Kanpur for SEM imaging because without it my thesis work never would be completed.

I am thankful to the Physics Department for providing me an excellent laboratory and other facilities, and for the opportunity of teaching exposure during teaching assistant in Prep, PHY 101, MSc. Optics, MSc. 2 year and AFM labs. I also appreciate the assistance in computer related problems by Arvind Mishra, and acknowledge the staff members of Physics Office including Narayanan G, Arvind Verma, Puja Shahoo, and M. Khan for their help.

I also acknowledge the CSIR, DST, department of physics and DORA of Indian Institute of Technology Kanpur for financial support.

I thank my seniors: Lipsa nanda, Sanggeta Chakravarti, Ashwath Babu, Neeraj Shukla, Dudh Nath Patel, Shyamlal, and friends: Hemnadhan Mayeni, Upkar Kumar, Dushyant Kumar, Gopal, Gyanendra Kumar, Lalruatfela, Nikhil Kumar, Prabhakar Tiwari, Pranati Kumari Rath, Shubhankar Das, Sunil Kumar, Seema Devi, Vandana Yadav, Bahadur Singh, Nimisha Raghuvanshi, Reeta Pant, Shraddha Sharma, Ashu Choudhary, Sushma Yadav who provided me a enjoyable company and enriching experiences during my stay here.

I am extremely grateful to my colleagues and lab-mates Prasanta Mandal, K. Jeyadheepan, Rajneesh Kumar, Sriram Guddala, Govind Dayal, Gangadhar Behera, Jhuma Dutta, Prince Gupta, Nadeem Akhtar, Naorem Rameshwari, Raghawendra Kumar, Rajesh Kumar, Jitendra Pradhan, Justin Pollock, Sanchit K. Singh, Rohan Nemade, Mahendra Arya, Ankush Panwar, Prabhanshu Pavecha and Shobhit Yadav for their love and support.

A special thanks for our Taekwondo coach Mr. Balram Yadav and Taekwondo Club for their enthusiastic love and support which kept me always active and happy.

I would like to acknowledge the tremendous support and unconditional love from my family members with unfailing conviction, particularly in difficult times, which provided me the necessary strength and patience to carry out this work. I am especially indebted to my father because it is he who procured the initial foundation which was beyond his economic reach. Although inexpressible in words, a special thanks to my wife Jyoti for her love and encouragement, and to my little son Keshav whose sole job was to keep us happy, which proved vital in focusing me to accomplish this thesis work.

Lastly but definitely not the least, I owe a debt of gratitude to the Almighty to sail the journey and made this possible by being with me all the time.

I seek pardon for all whose names are missed out unintentionally in spite of their immense and persistent support. While grateful to the people who have bring this thesis to fruition, all the mistakes and flaws that remain are my own.

September, 2015 Dheeraj Pratap

Synopsis

Name:	**Dheeraj Pratap**
Roll No.:	**Y9109063**
Degree for which submitted:	**Doctor of Philosophy**
Department:	**Physics**
Thesis Title:	**Anisotropic and Hyperbolic Metamaterials in the Cylindrical Geometry**
Thesis Supervisor:	**Prof. S. Anantha Ramakrishna**
Month and year of submission:	**September, 2015**

Metamaterials are artificially structured composite materials made of natural materials, and obtained by periodically repeating in space a unit cell termed a “meta-atom” that is analogous to the atom in natural materials. The properties of the metamaterials depend on the resonances of the geometrical structure as well as the constituent materials. For a fixed set of constituent materials, the metamaterials properties can be completely changed by changing merely the structural geometry. Metamaterials show some unusual electromagnetic/optical properties and light-matter interaction phenomena, which are not easily observed in natural materials. In natural materials, the optical anisotropy is usually very small and crystals usually possess orthorhombic symmetry. There are no natural materials having optical anisotropy with cylindrical or the spherical symmetries. The development of metamaterials break down these limitations. Incorporating such anisotropic metamaterials in waveguides or optical fibers give rise to very interesting novel properties compared to conventional waveguides or conventional optical fibers. In this thesis, we principally develop such nanostructured optical anisotropic fibers made of metamaterials

and study the electromagnetic modes in such waveguides filled or clad with anisotropic materials.

To design the metamaterials, in different frequency ranges of the electromagnetic spectrum, different kinds of fabrication techniques such as mechanical machining, optical lithography, chemical, deposition techniques, focused ion beam (FIB), electron beam lithography (EBL), laser micro-machining etc. are available. Fabrication of metamaterials for the visible range of frequencies is difficult because of the requirement of sub-micron size of the unit cell that arises from requirements of homogenization. There are few methods such as FIB, EBL by which nano structuring can be carried out at these length scale. But using these methods, only a very small area can be structured in costly and time consuming manners. Template methods are very good processes to fabricate nanostructures. To fabricate one dimensional nanostructures such as nanowires, nanoporous alumina can be used as templates. Using this method very high aspect ratio nanowires of metals, nonmetal, polymers materials including ordered carbon nanotubes, nano particles can be made over large areas of few centimeter squares to meters squares quickly, which is probably unachievable by any other technique. Nanoporous alumina are aluminium oxides having nanopores and obtained by anodization of the aluminium metal in an acidic environment. Anodization of a planar aluminium sheet gives planar nanoporous alumina in which the nanopores have hexagonal arrangement on the sheet surface and oriented perpendicular to the sheet surface. The nanopore organization, diameter or size, interpore distance, orientation and uniformity depend on various parameters such as the purity of aluminium sheet, surface roughness, anodization electrolyte, anodization voltage or current, solution temperature etc. We have used nanoporous alumina for our metamaterial fabrication in the planar and the cylindrical geometries, and we studied their optical properties of the resulting metamaterial structures. We present unique microwires made of nanoporous alumina with continuous pores that are oriented radially outwards, which can also be filled with plasmonic metals.

This thesis introduces a truly three dimensional nanostructured cylindrical metamaterial optical fiber, possibly for the first time in the field of metamaterials. These metamaterials are radially inhomogeneous with cylindrical anisotropy, and easy to fabricate in a cost effective manner over large scales quickly. These can be made to operate over a very wide range of electromagnetic spectrum from terahertz to optical frequencies, and have potential applications across branches of physics, engineering and biology. These nanoporous metamaterials are comparatively simple to fabricate, but have elegant properties. We have investigated the properties of the anisotropic metamaterial waveguides, and inhomogeneous and anisotropic metamaterial waveguides formed by such nanoporous alumina microtube that could also be embedded with plasmonic nanowires. We show that our cylindrical metamaterials can be used as anisotropic metamaterial waveguides or optical fibers that can support novel kinds of modes described by Bessel functions with imaginary or complex orders. Optical scattering of these systems and fluorescence from molecules placed in them also have been investigated. Our development can now enable many theoretical proposals in the area of metamaterials that have otherwise remained only hypothetical. The chapter wise summary of the thesis is given below.

The Chapter 1 gives an introduction to the subject matter of the thesis and covers the basic concepts of metamaterials and optical anisotropy including cases of extreme anisotropy when hyperbolic dispersion results. We discuss the classification of the electromagnetic metamaterials and the fabrication techniques used by us, namely, the nanoporous alumina template method in details. We introduce and discuss small amount of the previous theoretical and experimental works that try to implement metamaterials within waveguides and optical fibers, and suggest that systems may give rise to very interesting properties that are not possible in the ordinary fibers or waveguides. Since in our thesis, we use the finite element method (FEM) based COMSOL Multiphysics modeling software, therefore, we briefly introduce the FEM numerical technique and its implementation in the COMSOL multiphysics software to model electromagnetic problems. At the end of this chapter, we discuss the organization of the other chapters.

Chapter 2 is dedicated to describing the fabrication techniques for the cylindrical metamaterials that are central to the thesis. Anodization of planar aluminium sheets of high purity at optimized parameters to give planar nanoporous alumina with highly hexagonal ordered and uniform nanopores is described. Changing the organization of the nanopores arrangement using pre-textured aluminium sheets are discussed, and it is shown the nanopores can be easily forced to arrange linearly along meso-scale scratch marks on the aluminium sheet. In general, aluminium metal of any shape can be anodized and we adopted the process to the anodization of aluminium microwires of circular cross-sections of sub-hundred micron diameters to yield nanoporous alumina with radially emanating nanopores along the circular cross section that we term as cylindrical nanoporous alumina. Since the anodization of the aluminium microwire starts from the surface, therefore, in the cylindrical nanoporous alumina the nanopores are oriented along the radial direction of the microwire and the nanopore size and interpore separation distance decrease towards the axis of the microwire. The microwire can not be anodized completely up to the center, and an aluminium core is left behind which can be removed by chemical etching if necessary. We have also electrodeposited silver nanowires into the nanopores of the planar nanoporous alumina as well as in the nanopores of the cylindrical nanoporous alumina.

In Chapter 3, we discussed the homogenization of nanoporous alumina material for determination of a homogenized dielectric permiitivity tensor. Planar nanoporous alumina can be homogenized using the Maxwell-Garnett homogenization theory to obtain the effective dielectric permittivity. The fill fraction of the nanopore in planar nanoporous alumina is constant, and the system is effectively homogeneous and anisotropic for visible and infrared light. We model the structure of the cylindrical nanoporous alumina as an inhomogeneous and anisotropic medium due to the variation of the nanopore diameter and the interpores distance along the radius of the microwire. This necessitates the description by a local homogenization procedure. We homogenize the cylindrical nanoporous alumina by using the techniques of transformation optics and Maxwell-Garnett homogenization theory to obtain the effective dielectric parameters. Effectively, the cylindrical nanoporous alumina is an inhomogeneous as well as an anisotropic system for radiation with wavelengths greater than a few hundred nanometers.

In Chapter 4, we discuss the light guiding properties of the cylindrical nanoporous alumina. To see the effect of the anisotropy, we assume that the cylindrical nanoporous alumina are homogeneously filled and anisotropic. We derived the general mathematical modal analysis of the homogeneously filled and anisotropic waveguide in the coaxial geometry and develop the quantitative analysis of the cylindrical nanoporous alumina microtube as metamaterial waveguide. In the cylindrical nanoporous alumina waveguide, the modes are described by Bessel functions with integral, fractional, imaginary and complex orders while in the isotropic waveguides there are only integral order Bessel functions describe the solutions. The light confinement in the cylindrical nanoporous alumina waveguides are much higher than in the ordinary isotropic waveguides. In the case of the imaginary order modes, the mode fills out the whole volume while concentrating towards the center of the waveguide as the order increases. In contrast, it is well known that in the isotropic waveguides as the order increases the electromagnetic fields shift away from the center of the waveguide towards the periphery, which are whispering gallery modes. The modal dispersions of the cylindrical nanoporous alumina waveguides show backward wave propagation. The silver nanowire filled cylindrical nanoporous alumina waveguides are quite lossy due to the metallic inclusions.

In Chapter 5, we lift the approximation of homogeneously filling of the waveguide and study the light guiding properties of the inhomogeneously filled and anisotropic waveguides. We shown analytically that in the inhomogeneous and anisotropic case, the modes are coupled even if there is perfect electric conductor (PEC) condition in the core and at the outer region. The analytical solution can not be found in closed form in general and we carried out the FEM based COMSOL modeling of the inhomogeneous and anisotropic nanoporous alumina fiber. We found that there can be extremely high confinement of the modes.

Chapter 6 presents the light scattering properties of planar and cylindrical nanoporous alumina as well as studies on the fluorescence of molecules placed in these systems. The planar nanoporous alumina with linearly aligned nanopores show polarization sensitive scattering behavior with light. The darkfield and brightfield microscopy show that the gold coated planar nanoporous alumina with linearly organized nanopores are more scattering if the incident light polarization is along the nanopores alignment than if the light the polarization perpendicular to the nanopore alignment. Fluorescent dye molecules, Rhodamine-6G (R6G) doped in the poly-methyl-methacrylate (PMMA), were coated on planar nanoporous alumina (gold coated otherwise). We found that the fluorescence from the R6G coated planar nanoporous alumina get highly enhanced, while the fluorescence signal from R6G with gold coated planar nanoporous alumina was quenched because of the interaction with surface plasmons on the gold-nanoporous alumina interface. The silver nanowire deposited cylindrical nanoporous alumina show high scattering and plasmonic behavior. The nanopores of the cylindrical nanoporous alumina were filled with R6G molecule by immersing it into a solution of R6G in chlorobenzene. We measured the fluorescence properties and found a similar fluorescence characteristic like the planar nanoporous alumina. The fluorescence signal was much enhanced on the R6G coated cylindrical nanoporous alumina while it was quenched on the R6G coated on the silver nanowire filled cylindrical nanoporous alumina.

In the last Chapter 7, we summarize the thesis and discuss about the future scope of planar and the cylindrical nanoporous alumina. The cylindrical nanoporous alumina waveguides and fibers have structured nature, hence will always have scattering and absorbing losses and are not suitable for communication but have enormous potential for good couplers, sensors and non-linear applications. Some thermal applications such as wetting and evaporation dynamics of water on planar and cylindrical nanoporous alumina have been also investigated by us apart from the work in this thesis. We believe that such thin nanoporous alumina microtubes have been investigated for the first time. A lot of future work is required for the optimization of the synthesis, and applications of this very promising system.

List of Publications

Published:

1. *Wetting dynamics and evaporation of sessile droplets on nano-porous alumina surfaces*,
   S. K. Singh, S. Khandekar , **D. Pratap** and S. A. Ramakrishna,
   Colloids and Surfaces A: Physicochemical and Engineering Aspects, **432**, 71-81 (2013).

2. *Plasmonic properties of gold coated nano-porous anodic alumina with linearly organized pores*,
   D. Pratap, P. Mandal , and S. A. Ramakrishna,
   Pramana- Journal of Physics, **83**, 1025-1033 (2014).

3. *Anisotropic Metamaterial Optical Fibers*,
   D. Pratap, S. A. Ramakrishna, J. G. Pollock and A. K. Iyer,
   Optics Express, **23**, 9074-9085 (2015).

4. *Pool Boiling of Water on Nano-structured Micro-wires at Sub-atmospheric Conditions*,
   M. Arya, S. Khandekar, **D. Pratap** and S. A. Ramakrishna,
   Heat and Mass Transfer, (**Accepted, DOI 10.1007/s00231-015-1692-2**).

5. *A class of circular waveguiding structures containing cylindrically anisotropic metamaterials: Applications from radio frequency/microwave to optical frequencies*,
   J. G. Pollock, A. K. Iyer, **D. Pratap**, and S. A. Ramakrishna
   J. Appl. Phys., **119**, 083103-083110 (2016).

Preprints:

1. *Inhomogeneous and Anisotropic Nanoporous Alumina Metamaterial Optical Fiber*,
   D. Pratap, A. Bhardwaj and S. A. Ramakrishna,
   (To be submitted).

2. *Dropwise condensation of unsaturated humid air: Effect of nano-porous alumina surface treatments on flow condensation for fully developed turbulent flow*,
   F. Plourde, S. Khandekar, **D. Pratap**,
   (To be submitted).

Patents:

1. *Nanoporous Microfluidic Devices and Methods for their Preparation and Use in Heat Exchange Applications*,
   S. A. Ramakrishna, **D. Pratap**, S. Khandekar and J. Ramkumar,
   Intellectual Ventures, **ID: IN-875089**, (2014).
2. *Nanoporous Microtubes for Anisotropic Optical Fibers*,
   S. A. Ramakrishna and **D. Pratap**,
   SIDBI Innovation & Incubation Centre, IIT Kanpur, **Ref: 850/DEL/2014**, (filed).
3. *Compact Air Cooler with Nano- Structured Surfaces*,
   S. Khandekar, S. A. Ramakrishna, **D. Pratap**, A. Panwar, P. Pavecha and S. Yadav,
   SIDBI Innovation & Incubation Centre, IIT Kanpur, **Ref: 3246/DEL/2014**, (filed).

Table of Contents


भारतीय प्रौद्योगिकी संस्थान कानपुर
INDIAN INSTITUTE OF TECHNOLOGY KANPUR

List of Figures

List of Tables

Chapter 1

Introduction

1.1 Introduction to Metamaterials

The optical properties of various materials and crystals have been studied extensively and their optical phenomena such as refraction, polarization, birefringence, linear and non-linear effects etc. are well known [1–5]. The devices have to be designed according to the properties of the materials because the materials properties can not be changed. Most of the crystals are optically anisotropic with their optical properties arising from the atomic/molecular polarizabilities and the arrangement of the atoms in the materials [1, 3, 4]. The anisotropy in natural crystals is, however, very small and the optical anisotropy can be changed only to a small extent by applying external fields or stresses. Usually crystals have orthorhombic symmetries and there are no cylindrically or spherically symmetric anisotropies in the natural crystals. Over the last couple of decades, a new class of materials are called 'Metamaterials', whose electromagnetic or optical properties can be obtained according to the need [6–8] have been developed. Metamaterials are artificially designed structured composite materials that utilize resonances of the structure to control and manipulate the waves and the physical phenomena in them. Properties of the metamaterials depend on the constituent materials used in their construction as well as the geometrical structures. Metamaterials are typically obtained by periodically repeating a unit cell called *meta-atom* that is analogous to an atom or a molecule in natural materials. These metamaterials can show properties that usually are not found in natural materials. In general, metamaterials can be designed for any kind of waves such as electromagnetic waves, acoustic waves, seismic and magnetic spin waves or any other type of waves, but here in this thesis, our interest is only on metamaterials for electromagnetic waves with frequencies ranging from microwave (10^9 Hz) to optical waves (10^{15} Hz). Metamaterials are being used for sub-wavelength imaging, superlens, enhanced spontaneous emission, electromagnetic invisibility and in non-linear applications [7,8].

In metamaterials, the anisotropy can be changed literally at will. Some of them even show indefinite behavior for the response tensor [9], which we shall discuss in the next section. Most of the metamaterials are planar structured metamaterials and provide novel responses only for waves polarized or incident in specific directions. Thus, unless designed for isotropic responses, most metamaterials are intrinsically anisotropic. For example, unidirectionally oriented dilute arrays metal microwires function as a homogeneous medium which have very low plasma frequency (10^9 Hz) and this metal microwire array medium has uniaxial anisotropy, But if the microwires were uniformly oriented along all the three directions then the medium would become isotropic [10,11], but would also have a very small plasma frequency. Some researchers have demonstrated layered structured metamaterials in half-cylindrical shaped and rolled metamaterials that have cylindrical symmetry [12–15]. We also note that field cloaking devices mostly are with cylindrical symmetry [16–18], where these new structured materials play a central role. But these devices spanning along the longitudinal direction (cylindrical axis) are only a single meta-atom, and effectively, they appear as two dimensional circular objects due to the axis of invariance. An optical cloak in the visible frequency made of tiny prolate spheroids oriented along the radial direction in a cylindrical dielectric medium has also been theoretically discussed [17]. In a similar manner, an optical cloak, which was made of uniform metal nanowires embedded in a dielectric medium, was also shown theoretically only [18]. But no one has yet demonstrated practically radially oriented nanowires cylindrical system.

In this thesis, we report on the fabrication, characterization and some applications of radially structured anisotropic metamaterials with cylindrical symmetry. These metamaterials are truly nano-structured in a three dimensional sense and can be produced on very large scales in a cost effective manner. These cylindrical metamaterials are not be limited just to optical applications, but several other applications including thermal engineering applications, are possible. In the present chapter, we shall introduce the basic concepts and tools, which will be needed to understand the electromagnetic properties of cylindrical metamaterials that are the focus of our thesis. In the rest of the chapters, the fabrication, characterization, modeling and some applications of the radially structured cylindrical metamaterials are discussed.

1.1.1 Classification of Metamaterials

Since the metamaterials are composite materials, therefore, they are inhomogeneous at the subwavelength/micron/nano scale but can be described as a homogeneous medium on length-scales much larger than the wavelength. Homogenization techniques such as Maxwell-Garnett, Bruggeman formalism, field averaging etc. are deduce to get the effective parameters that describe the wave propagation in the metamaterials. For valid homogenization, the size of the unit cell of the metamaterials should be electrically or magnetically small. We will discuss the Maxwell-Garnett homogenization technique in the cylindrical geometry in Chapter 3. The effective permittivity and effective permeability are two possible parameters by which the metamaterials properties can be described. By designing the metamaterials with the possible the effective permittivity and effective permeability, the physical phenomena in the metamaterials can be controlled.

In general, the effective permittivity and effective permeability of an isotropic metamaterial are complex functions of frequency. In metamaterials, the numerical value of the real part of the effective material parameters may be positive or negative. For the

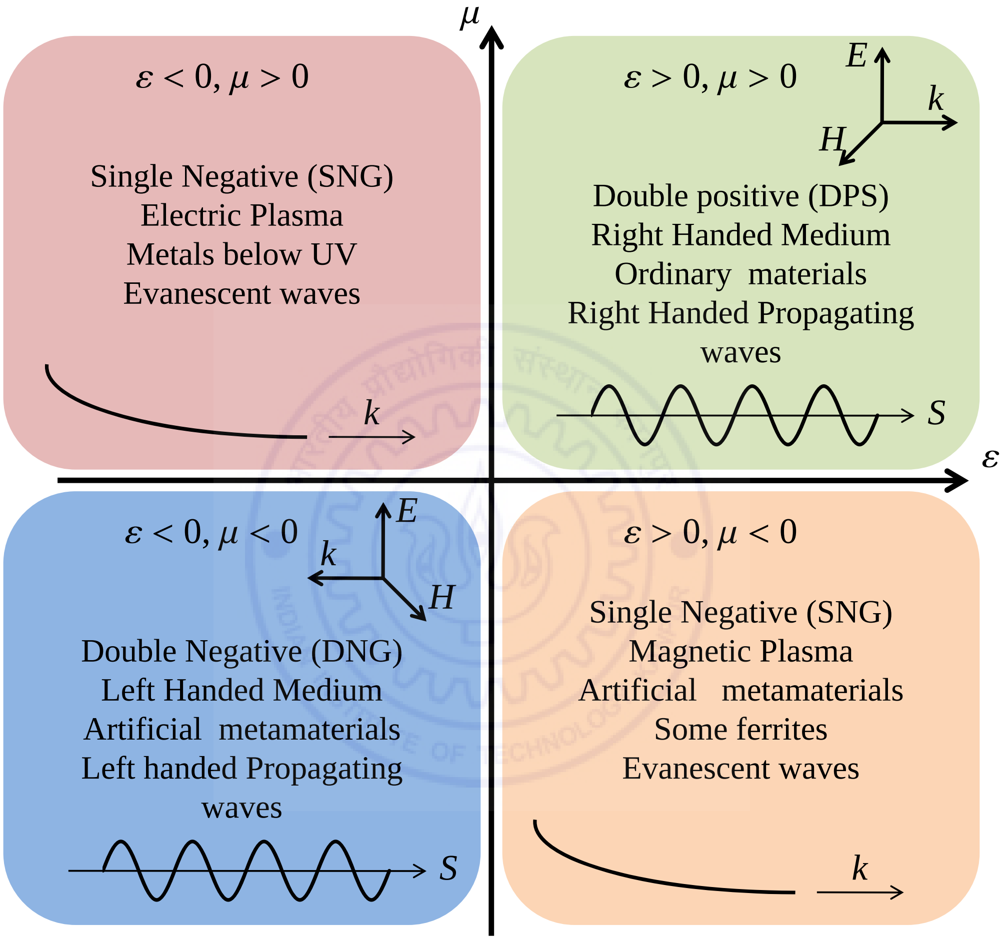

Figure 1.1: A schematic diagram to show the material classification based on the real parts of the material parameters ε and μ plotted along the x and y axes respectively. Here we only consider isotropic media. The decaying curved line represents the evanescent wave while the oscillatory line represents the propagating wave.

sake of simplicity to classify the materials, we here consider then to be isotropic and lossless when the imaginary part of the medium parameters may be considered to be negligible. Figure 1.1 show a general classification of materials based on the permittivity (ε) and permeability (μ) components. The first quadrant corresponds to media with both parameters being positive called *double positive* (DPS) media. Most of the natural materials lie in this region. The electric field ($\vec{E}$), magnetic field ($\vec{H}$) and propagation vector ($\vec{k}$) of the electromagnetic wave form a right handed triad. Hence, the materials that lies in this quadrant are called *right handed materials* (RHM) also. If either of the parameters, the permittivity or the permeability become negative, then the metamaterials are said to be *single negative metamaterials* (SNG) and these lie in the second and fourth quadrants of Fig. 1.1. The most interesting case occurs when both the parameters simultaneously become negative, then the metamaterials are said to be *double negative metamaterials*(DNG) and lie in the fourth quadrant as shown in the Fig. 1.1. If both the parameters become negative, then negative refraction is possible. In this region, the vectors E, H and k form a left handed triad, and are called *left handed materials* (LHM). Metamaterials can be designed to correspond to any one of these four quadrants.

In general, metamaterials are anisotropic too and their material parameters are described by second ranked tensors. We know that the anisotropic materials posses a large variety of interesting properties that are not present in isotropic materials. One classification that can be made for anisotropic metamaterials depends on the behavior of the dispersion relations or on the sign of the eigenvalues of the material parameter tensors. Since the dispersion of a wave in a biaxial anisotropic medium is quite complicated [19], we shall discuss this aspect in the case of uniaxial dielectric anisotropic metamaterials. Consider an uniaxial non-magnetic ($\bar{\bar{\mu}} = \mu_0(1,1,1)$) medium in which the permittivity tensor is $\bar{\bar{\varepsilon}} = \varepsilon_0(\varepsilon_x, \varepsilon_x, \varepsilon_z)$. In this medium the dispersion relation is given by the following expression

$$\frac{k_x^2 + k_y^2}{\varepsilon_z} + \frac{k_z^2}{\varepsilon_x} = \left(\frac{\omega}{c}\right)^2. \tag{1.1}$$

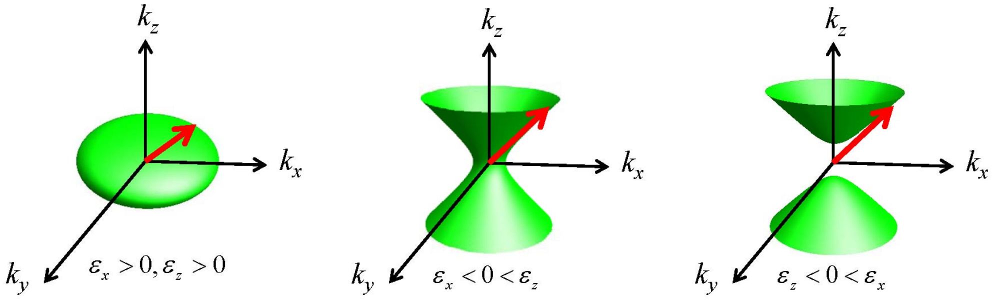

(a) (b) (c)

Figure 1.2: The iso-frequency surfaces of an uni-axial non-magnetic material. (a) The iso-frequency surface is an ellipsoid if $\varepsilon_x > 0$ and $\varepsilon_z > 0$. (b) The hyperboloid of one sheet for $\varepsilon_x < 0 < \varepsilon_z$. (c) The hyperboloid of two sheets for $\varepsilon_z < 0 < \varepsilon_x$.

If in Eq. (1.1), the $\varepsilon_x > 0$ and $\varepsilon_z > 0$, then the iso-frequency surfaces (ω=constant) would be ellipsoids as shown in Fig. 1.2(a). This happens in all natural materials and most metamaterials as well. If in Eq. (1.1), the metamaterial has $\varepsilon_x < 0$ and $\varepsilon_z > 0$, then the iso-frequency surfaces would be hyperboloids of one sheet (Fig. 1.2(b)). If $\varepsilon_x > 0$ and $\varepsilon_z < 0$ for the metamaterials, then the iso-frequency surfaces would be hyperboloids of two sheets (Fig. 1.2(c)). The second and third cases have an extreme anisotropy and the corresponding metamaterials are defined as *indefinite* metamaterials as the eigenvalues of the permittivity matrix have no definite sign, or as *hyperbolic* metamaterials [9] as the dispersion equation becomes hyperbolic. The hyperbolic metamaterials can be resonance free and typically exhibit lower losses than the resonant metamaterials.

In general, metamaterials can be fabricated over most of the applicable electromagnetic spectrum from microwaves to optical frequencies. Metamaterials can be classified on the basis of the wavelength or frequency regime also. Then the wavelengths are approximately 100 μm to 1 dm, the metamaterials are microwave metamaterials because their resonance frequencies lie in gigahertz range [10, 11]. In the far infrared regime (approximately 10 μm to 100 μm wavelengths) the resonance frequencies lie in terahertz region and the metamaterials are called terahertz metamaterials [20–22]. Up to the terahertz

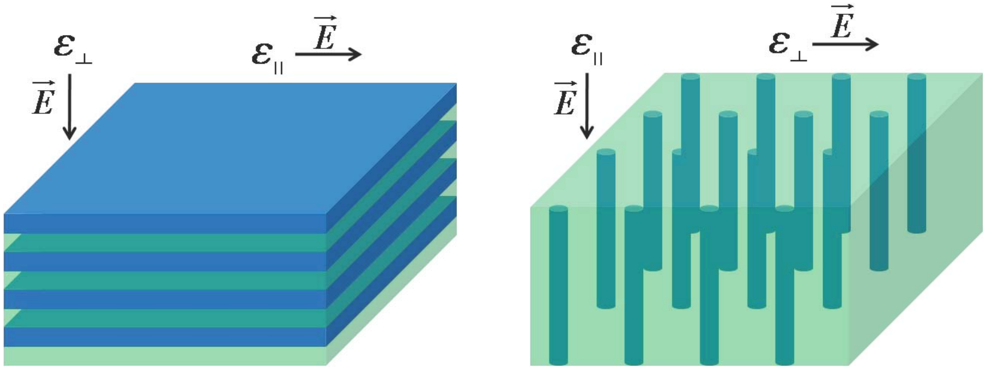

(a) (b)

Figure 1.3: The schematic of two types of the hyperbolic metamaterials. (a) The alternating electrically thin layers of metal and dielectric (b) the metal nanowires of electrically small diameters embedded in a dielectric host gives the metamaterial of non-resonant type.

frequencies, metals used in the construction of metamaterials can be considered as perfect or ohmic conductors. Infrared metamaterials are those with resonance frequencies at long wave infrared to the short infrared ($\lambda \simeq 20 - 2\mu$m). Metamaterials with smaller resonance wavelengths are known as *near-infrared* or *optical* metamaterials. At these large frequencies, the electronic inertia (mass) considerably affects the performance and the skin depth (δ) has to be properly accounted to describe the resonance. In the visible range, the resonances of metamaterials can occur due to surface plasmon excitations, and hence, such metamaterials are called *plasmonic* metamaterials [17,23,24]. In many cases, the metamaterial unit cell becomes comparable with the wavelength of the interacting radiation, and in those cases the metamaterials would be more aptly termed as *photonic* metamaterials [25–27]. Some very simple and practically possible examples of hyperbolic metamaterials are the layered metamaterials [12] and nanowire metamaterials [28]. In Fig. 1.3, these examples of hyperbolic metamaterials are schematically shown.

A metamaterial with alternating layers of a metal and a dielectric effectively behaves as a hyperbolic metamaterial as shown in Fig. 1.3(a). Consider a layered hyperbolic medium that is made of alternate layers of electrically thin films of silica (SiO_2) and silver metal with film thicknesses of d_1 and d_2 respectively. The effective permittivity can be obtained by noting the requirement of field continuity. If the layers are very thin, then the fields in them can be assumed to be effectively uniform. If the field is incident parallel to the interface of the thin films then the electric field components E_1 and E_2 in the two media on either side of an interface will be continuous. Therefore, averaging the displacement field across the interface, the parallel component of the relative effective permittivity can be written as

$$\varepsilon_{\parallel} = \frac{\varepsilon_1 + \varepsilon_2 \eta}{1 + \eta}, \tag{1.2}$$

where $\eta = d_2/d_1$. If the incident field is perpendicular to the thin films interface, then the displacement field components D_1 and D_2 will be continuous. Therefore, averaging the electric field components, the perpendicular component of the relative effective permittivity can be obtained as

$$\varepsilon_{\perp}^{-1} = \frac{\frac{1}{\varepsilon_1} + \frac{\eta}{\varepsilon_2}}{1 + \eta}. \tag{1.3}$$

The components $\varepsilon_{\parallel}$ and $\varepsilon_{\perp}$ with the frequency are plotted in Fig. 1.4. The data of silica has been taken from the optical constant handbook [1] and Drude-Lorentz model used for silver metal. We see a resonance in the permittivity, as shown in Fig. 1.4. Further, we note the hyperbolic dispersion that becomes possible for both frequencies below $(\varepsilon_{\parallel} < 0, \varepsilon_{\perp} > 0)$ and above $(\varepsilon_{\parallel} > 0, \varepsilon_{\perp} < 0)$ the resonance frequency.

Plasmonic nanowires embedded in a dielectric medium as shown in Fig. 1.3(b) show hyperbolic dispersion too. Now consider a medium in which silver metal nanowires of electrically small diameters are embedded, oriented along one direction in a silica matrix. Let f be the fill fraction of the nanowires in the silica matrix. Applying the similar approch of field averaging we shall find the effective permittivity components of the nanowire hyperbolic media. If the incident field is along the nanowires direction then the electric field components will be continuous at the interface of the silver nanowire and the silica matrix, therefore, averaging the electric displacement gives the parallel

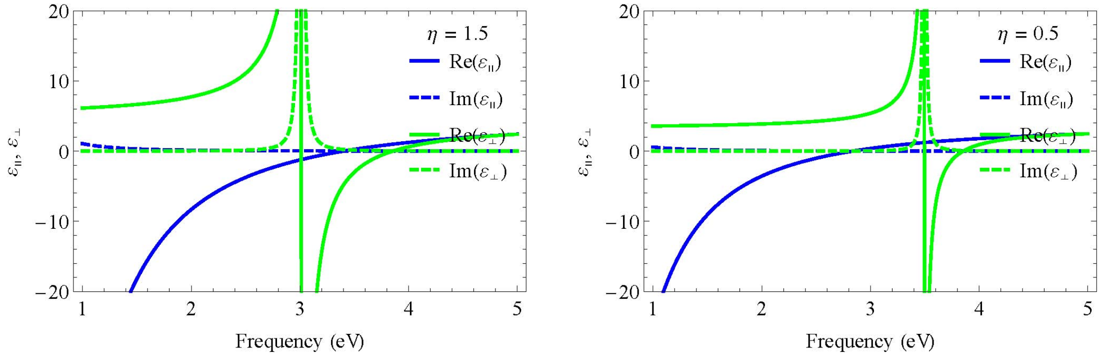

(a) (b)

Figure 1.4: Plots effective permittivity components $\varepsilon_{\parallel}$ and $\varepsilon_{\perp}$ of layered hyperbolic metamaterials made of alternate layers of silica and silver metal. (a) $\eta = 1.5$ and (b) $\eta = 0.5$. The data of the silica taken from optical constant handbook and Drude-Lorentz model used for silver metal.

components of the permittivity component as

$$\varepsilon_{\parallel} = (1 - f)\varepsilon_1 + f\varepsilon_2. \tag{1.4}$$

On the other hand, $\varepsilon_{\perp}$ can be obtained by some homogenization procedure (see Chapter 3). Figure 1.5 shows the dispersion of a nanowire metamaterials where the silver nanowires are embedded along one direction in silica matrix.

Up to here, we have discussed briefly about metamaterials and their classifications. Since the metamaterials are structured composite materials, therefore, the biggest challenges lie in the fabrication. In the next section, we shall discuss some techniques to fabricate metamaterials.

1.1.2 Fabrication of Metamaterials

Depending on the electromagnetic spectrum regime at which the metamaterial has to operate, different fabrication techniques need to be used. As we go from the microwave to the visible frequency region, the fabrication difficulty increases because of smaller unit

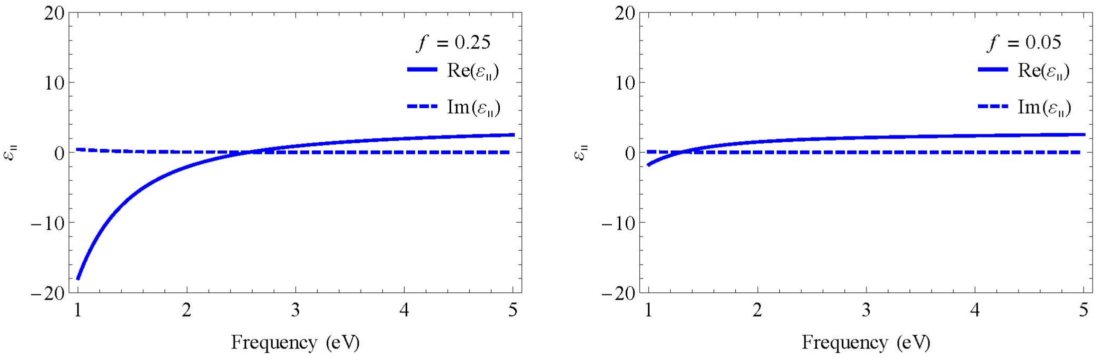

(a) (b)

Figure 1.5: Plots effective permittivity component $\varepsilon_{||}$ of nanowire hyperbolic metamaterials made of silver nanowire embedded in silica matrix. (a) $f = 0.25$ and (b) $f = 0.05$. The data of the silica taken from optical constant handbook and Drude-Lorentz model used for silver metal.

size and less availability of fabrication techniques that become more time consuming and less cost effective. At gigahertz frequencies, fabrication is easy due the large size of the meta-atoms that are nearly several of millimeters. In this range, conventional machining methods or printed circuit board (PCB) fabrication methods can be used to fabricate the metamaterials. For the terahertz range, the unit size becomes order of tens of micrometers and there are various techniques available such as laser micro-machining, optical lithography, electron beam lithography (EBL).

In the visible range, the fabrication difficulties increase enormously due to the very small sizes of the meta-atoms. In this range, the meta-atom unit cell size is sub-micron. There are very few techniques that work well in this size range. Focused ion beam (FIB) and EBL techniques are helpful for this purpose, but have the drawback that they can not be used to make structures on large areas and are also very time consuming and very expensive. Using optical lithography, this can be done quickly on larger scales, but there are other limitations of resolution and the thickness of the structures possible. In the visible range to make layered metamaterials, various thin film deposition techniques such as thermal vapor deposition, electron beam evaporation deposition, pulsed laser deposition, sputtering etc. are suitable. The template method, which will be discussed in later sections of this chapter, is one of the best method to fabricate nanostructured or nanowire metamaterials. Using this method highly organized nanomaterials and very high aspect ratio nanowire metamaterials can be fabricated on large scales. Nanoporous alumina templates are widely used to fabricate such nanowire metamaterials. In fact, this template technique is not only suitable for visible range metamaterial fabrication but may be suitable for near infrared metamaterials too by tuning the template structure using the fabrication parameters.

This thesis discusses the fabrication of the cylindrical metamaterials using nanoporous alumina templates, and their application as metamaterial waveguides and optical fibers by themselves. Hence, in the next section, we shall briefly introduce the development of metamaterial inclusions in waveguides and optical fibers.

1.2 Role of Metamaterials in Waveguides and Optical Fibers

Optical fibers form the backbone of optical communications systems worldwide. Their analogues in the microwave regime are hollow or coaxial metallic waveguides, which are indispensable in applications requiring field confinement, low losses, and high power-handling capability. The introduction of physical structure in the form of a periodic array of microscopic air holes running along the fiber axis in the photonic crystal fiber [29] gives rise to new possibilities. Light can even be confined within a hollow core or a core of lower refractive index due to confinement caused by a photonic band gap in the surrounding region containing a periodic array of holes. Alternatively for a solid core surrounded by microholes, the clad region with the microholes effectively creates a region with lower modal index for light propagating in the core and confines light by a modified total-internal-reflection effect. Birefringence of the modes in these fibers usually results from a two-fold asymmetry, and even small birefringence created by applied strain provides for many sensor applications [30]. However, these fibers usually have no structure or structural anisotropy perpendicular to the fiber axis.

Introducing the metamaterial in the design of the optical fiber or waveguide can give rise to some unique properties which can not be found in conventional optical fibers or waveguides. Interesting phenomena have been shown in microwave rectangular and circular waveguides loaded with metamaterials, including propagation at frequencies below the fundamental mode of the unfilled waveguide [31,32]. Similarly, the unprecedented control over the metamaterial properties as well as the enormous flexibility of applications possible with a fiber makes it attractive to combine them into a common platform. Theoretical discussions of fibers made of negative-refractive-index materials have indicated interesting properties such as sign-varying energy flux [33] and zero group-velocity dispersion [34]. Surface waves guided along a cylindrical metamaterial waveguide were discussed in [35]. Dispersion of modes in a fiber with anisotropic dielectric permittivity was also discussed recently [36]. However, the immense difficulty of practically assembling small nanostructured metamaterial units inside the micrometer sized fibers has essentially discouraged the discussion of such systems for optical frequencies. Only some cylindrically layered tubes, or those with coaxially oriented nanowires that are otherwise uniform along the axis, have been theoretically discussed [37, 38] as metamaterial optical fibers. These layered tubes due to the inherent anisotropy of the layered structure as explained in the section 1.1, provide an anisotropic waveguide with cylindrical symmetry. Recently, guided modes in a hollow core waveguide with a uniaxial metamaterial cladding have been theoretically discussed [39], where the metamaterial was proposed to consist of a layer of drawn split-ring resonators. The dispersion of the transverse components of the magnetic and dielectric properties of the metamaterial clad was found to dominate the behavior of the modes [40] and a drawn fiber with a single split-ring resonator at the fiber axis was demonstrated for terahertz frequencies in [41]. We note that all the proposals for metamaterial fibers so far have considered only designs that are invariant and homogeneous along the fiber axis, i.e., effectively the problem is only two-dimensional, presumably because only the drawing technique was considered for the fabrication of these fibers. This limits the discussion to a form of anisotropy with effective dielectric parameters $\varepsilon_r \simeq \varepsilon_\phi \neq \varepsilon_z$.

In the later chapters of this thesis, we shall show that application of anodization techniques [42] to aluminum microwires can result in a three-dimensionally radially structured cylindrical metamaterial and can be used as an anisotropic metamaterial optical fiber made of nanoporous alumina ($\mathrm{Al_2O_3}$). In the next section, we shall introduce about the anodization technique to form nanoporous alumina and its use as a template in fabrication of nanowire metamaterials.

1.3 Nanoporous Alumina

Nanoporous alumina are aluminium oxides having nanopores that self organize and get arranged in a hexagonal ordered lattice during anodization. These are obtained by anodization of aluminium sheets in an acidic environment [42]. While anodization, at the anode the liberation of hydrogen gas bubbles create nanopores and to minimize the energy of the system the nanopores arranged themselves in an hexagonal order. For the anodization of an aluminium sheet, various acids such as sulfuric acid, oxalic acid, phosphoric acid and many more can be used [43] to obtain nanopores with different size and spacing. The anodization starts from the surface of the aluminium sheet and the nanopores grow perpendicular to the surface [44]. Ideally, the nanopores are organized in a hexagonal pattern. The nanopore sizes, organization and interpore distances depend on the aluminuim purity, surface roughness, electrolyte nature, anodization voltage or current, temperature, number of anodization steps and time [43]. The organization of nanopores even for very pure aluminium sheet can be changed by pre-texturing the aluminium sheet surface [45,46]. Some typical acids and parameters of their anodized products under some typical conditions are listed in Table 1.1. Increasing the acid temperature and keeping all other parameters constant will increase the nanopore size, interpore distance as well as the ordering of the nanopores. But with increasing temperature, decreases the ordering

Table 1.1: The aluminium anodization conditions and the result at parameters of the nanoporous alumina for some frequently used acids and conditions (Adapted from Santos et al., Materials, **7**, 4297 (2014)).

Acid	Concentration (M)	V (V)	T ($^{\circ}C$)	d_p (nm)	d_{int} (nm)	Growth rate (μm.h^{-1})
H_2SO_4	0.3	25	5-8	25	63	7.5
H_2SO_4	0.3	40	0-1	30	78	85
$H_2C_2O_4$	0.3	40	5-8	50	280	3.5
$H_2C_2O_4$	0.3	140	0-1	30	100	50
H_3PO_4	0.1	195	0-1	160	500	2

of the nanopores. So to get higher ordered nanopores, the anodization should be carried out at lower temperatures. The optical transparency also depends on the fabrication parameters which we shall show in the Chapter 2. Nanopore size and interpore distance increase with acid concentration also.

1.3.1 The Two-Step Anodization

In the previous subsection, we mentioned that the nanopore ordering depends on the number of steps of anodization and its time. If the aluminium sheet is anodized once then the nanopores do not form as straight pores and not arranged in hexagonal order [42,47]. This anodization is called *first anodization*. Merging of nanopores or branching of a nanopore may happen in the nanoporous alumina obtained after the *first anodization*. This is due to the influence of surface inhomogeneities, stresses etc. If the alumina is subsequently etched off, the we get a nanosize concave pre-textured aluminium surface [47]. The re-anodization of alumina etched aluminium sheet at same parameters gives rise to highly ordered and straight nanopores as the original surface inhomogeneties have no effect now. This subsequent re-anodization is called the *second anodization*, and the whole process is called a *two-step anodization* process [42]. The Fig. 1.6 shows schematically the two-step anodization technique. At fixed parameters of the anodization, the size of nanopores and

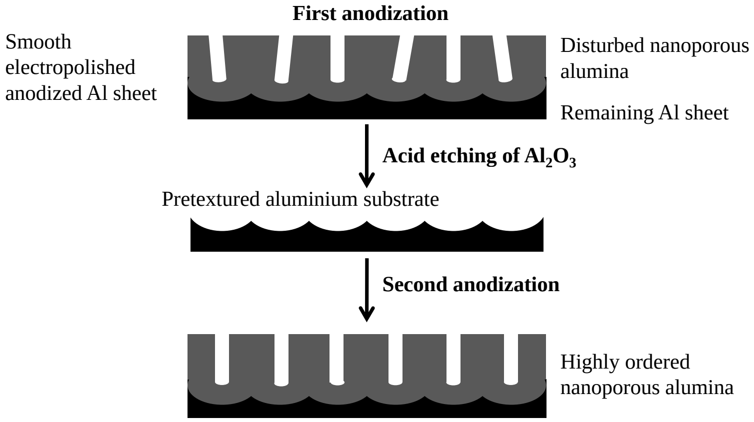

Figure 1.6: The schematic for the two step anodization. In this method nanopores become straight and more organized.

the lattice size are also fixed. But after the anodization, the size of the nanopores can be increased by widening the nanopores by slow dissolution in dilute phosporic acid. Pore widening can be carried out only up to the interpore distance otherwise the nanopores would merge into each other and the whole nanoporous alumina network would get dissolved by the phosphoric acid. In Fig. 1.7 the FESEM images of nanoporous alumina before and after pore widening in a 5% phosphoric acid are shown. The anodization time was 90 minutes at room temperature. It can be seen in Fig. 1.7(b) that if the pore widening would be carried out for more time, then the nanopores would merge with each other.

1.3.2 Barrier layer removal

After the anodization process, at the bottom of the nanoporous alumina, an impermeable insulating alumina barrier layer is left behind followed by conducting aluminium. To electrodeposit some metal into the nanopores, we have to remove the impermeable barrier layer and it can be removed by several methods. The common method is the wet chemical etching. It is carried out by putting the nanoporous alumina into dilute phosphoric

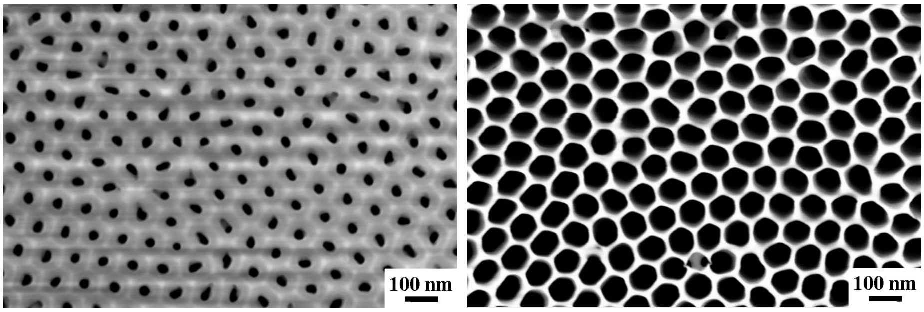

(a) (b)

Figure 1.7: The FESEM images of nanoporous alumina (a) before and (b) after the pore widening. The pore widening was done in 5% H_3PO_4 for 90 minutes at room temperature.

acid after removing the bottom aluminium in some salt electrolytes such as chromic acid [48]. This procedure is illustrated schematically in Fig. 1.8(a). This method is good to remove the barrier layer from a thicker nanoporous alumina templates. In thin nanoporous alumina, after dissolving the supporting aluminium sheet at the bottom, it is very difficult to handle the micrometer thick templates.

A second method of barrier layer removal is the voltage or current reduction method. The fact that the barrier layer thickness increases with the anodization voltage or current in utilized here. In this method at the end of the anodization process, the voltage or current are reduced slowly so that the impermeable layer thickness gets drastically reduced and becomes porous as well. This need to be carried out in a very controlled manner otherwise small fluctuations of the voltage or current might increase the barrier thickness [47]. Using this method, there will still be left a 1 to 2 nm thick barrier layer. After this stage the nanoporous alumina with aluminium at bottom can be used for AC electrodeposition [47]. The remaining barrier layer can be further removed by dissolving it in phosphoric acid wash. This method is good for thin or thick both types of nanoporous alumina because at the bottom there will be the aluminium sheet left for mechanical support. The second method of barrier layer removal by voltage or current reduction is shown schematically in Fig. 1.8(b).

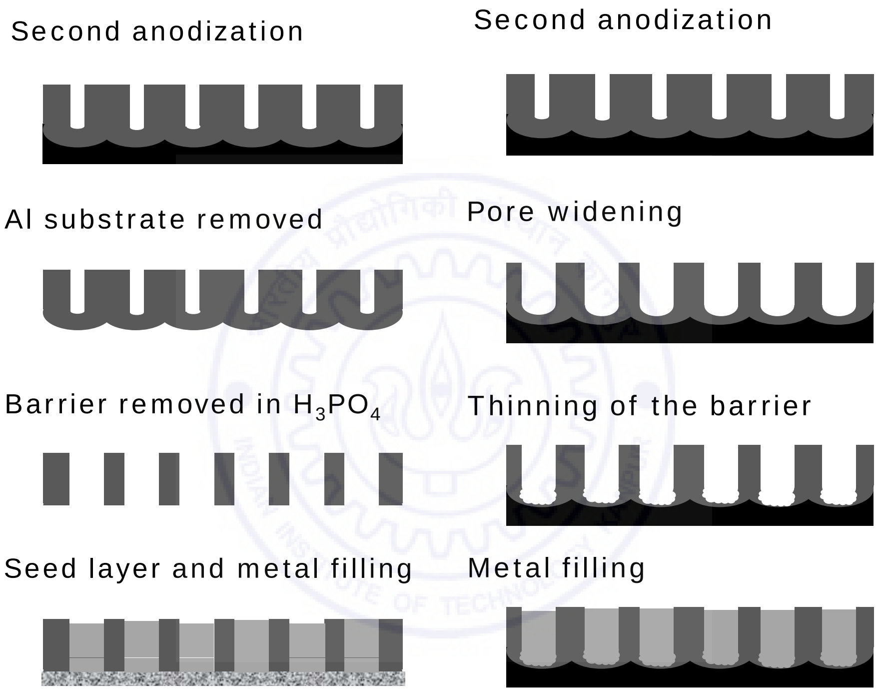

(a) (b)

Figure 1.8: Schematic illustration of two methods for barrier removal. Cross section of the nanoporous alumina are shown at various stages. (a) The wet etching process in H_3PO_4 and (b) shows the voltage/current reduction method.

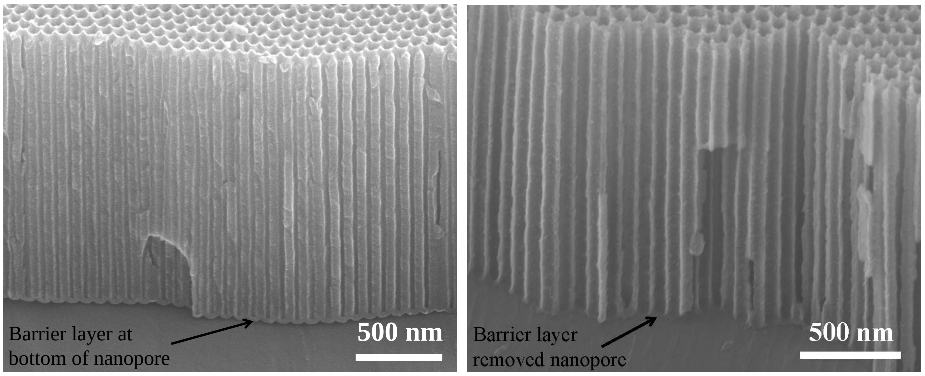

(a) (b)

Figure 1.9: The FESEM images of nanoporous alumina (a) before and (b) after the barrier layer removal by the cathodic polarization process. (a) Shows nanopores with the barrier layer at the bottom and bellow the barrier layer the remained aluminium sheet was used to give the electrical contact to the cathodic polarization process. (b) Shows the nanoporous alumina with removed barrier layer by cathodic polarization process.

A third method of barrier layer removal is called cathodic polarization. In this method, after the anodization process is complete, a reverse electrolysis of the alumina template is further done. The alumina template is used as cathode and graphite or platinum as anode in a diluted potassium chloride solution [48], and by applying a negative potential to the alumina template, the barrier layer gets removed electrolytically. A FESEM of the cross section of the nanoporous alumina with the barrier layer and with the barrier layer removed is shown in Fig. 1.9. This method needs good optimization. If the polarization time is less, then the barrier layer would not be fully removed and if the time become more then it would corrode the aluminium also. This method works well for thinner nanoporous alumina. The cathodic polarization also widens the size of the nanopores. For thicker nanoporous alumina, the polarization time would be more and this causes the nanopores merge with each other. So it can not be used easily for thicker nanoporous alumina.

We have discussed some methods to remove the barrier layer from nanoporous alumina. After removing the barrier layer, the nanoporous alumina can be used as templates to grow metal nanowires for plasmonic and metamaterial study. In next section we shall discuss about the metal nanowire deposition into the nanopores of the nanoporous alumina and the application as nanowire metamaterials.

1.4 Electrodeposition and the Nanowire Metamaterials

In fact, nanoporous alumina themselves are structured anisotropic materials that can work as metamaterials. The nanoporous alumina can be further used as templates to fabricate one dimensionally oriented thin wire composite structures. After removing the barrier layer, the nanopores can be filled by some materials such as metals, polymer, dimers, nanotubes, nanoparticles etc. [46]. External materials filled nanoporous alumina also works as metamaterials [28]. By filling the nanopores with certain materials, the alumina matrix can be dissolved in some electrolyte and the nano objects (typically nanowires) can be separated [49,50]. Thus it becomes a means for the uniform synthesis of nanowires. We are interested here in the deposition of metal nanowire inside the nanoporous alumina.

The metal nanowires synthesis using the nanoporous alumina template is mainly done by AC or DC electrodeposition techniques. If we remove the barrier layer by a wet etching method, then we are left with only nanoporous alumina. A thin or thick layer of a conductor like silver or gold need to be deposited at one face of the nanoporous alumina as a seed layer. This nanoporous alumina is used as the cathode and graphite or platinum as the anode in a metal salt solution of interest. By applying an AC or DC voltage to the electrodes, the metal nanowires can be deposited into the pores of the nanoporous alumina [51]. If the barrier layer is removed by voltage reduction or cathodic polarization method, then the template can be used directly for electrodeposition without any seed layer [47]. In Fig. 1.10, the FESEM image of silver nanowire grown in the alumina template is shown. Figure 1.10(a) shows alumina template with the barrier layer removed. Figure 1.10(b) and Fig. 1.10(c) show the top view and cross section of silver nanowires

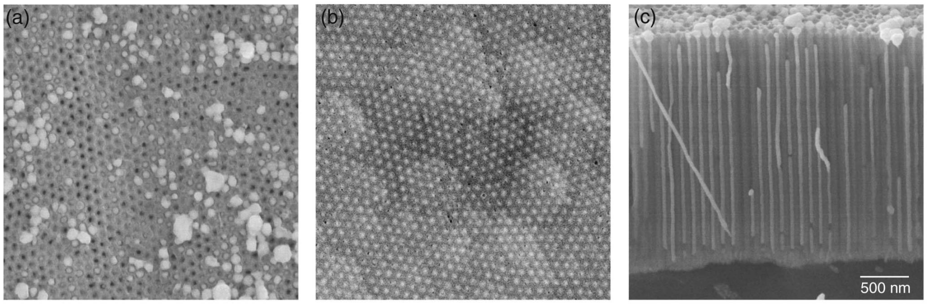

(a) (b) (c)

Figure 1.10: The FESEM images of metalized nanoporous alumina. (a) the bare nanoporous alumina, (b) the top view of silver nanowire deposited nanoporous alumina and (c) the cross section of silver nanowire deposited nanoporous alumina. Reproduced with permission from Sauer et al., Journal of Applied Physics, **91**, 3243 (2002). Copyright 2002, AIP Publishing LLC.

electrodeposited inside the pores of the nanoporous alumina template respectively. Since at the bottom there is an aluminium base, therefore, after dissolving the alumina matrix one can obtain free standing nanowires. Very high aspect ratio nanowires can not be obtained as free standing nanowires because the nanowires will tend to collapse [52].

There are several applications of nanowire embedded nanoporous alumina. But here our primary interest is in its use as nanowire metamaterials. Nanowire embedded nanoporous alumina exhibit the hyperbolic dispersion, and these metamaterials can also show the negative refraction phenomena [51]. Here the negative refraction happen because of the hyperbolic nature instead of a negative refractive index. It can be used as a hyperbolic flat lens [53]. The nanowire metamaterials can be made over very large areas. The nanowire metamaterials are only two dimensional because the nanopores and the nanowire growth occur only along one direction. In literature, the nanowire metamaterials are only known in flat geometry. This thesis will deal with nanowire metamaterials in the cylindrical geometry, which is discussed in the later chapters.

1.5 The Finite Element Method

As we know, most of the electromagnetic metamaterial structures are very complex systems to model. In general, only few problems with some symmetries can be approximately solved analytically, but most of the structures are not amenable to analytical solutions. To solve such complex systems, there is a need for numerical techniques that can be implemented on computers. There are various numerical techniques such as the finite difference time domain (FDTD), the finite element method (FEM), method of moments, mesh free method etc. In this thesis, we have used a commercial simulation software, COMSOL multiphysics 4.4, which is based on the FEM to model our metamaterial structures. In this section, we introduce some basic concepts about the FEM and method used in the COMSOL multiphysics software.

Many physical systems can be represented by partial differential equations. By solving the set of differential equations with proper boundary conditions, the properties of the system can be obtained. The FEM is a numerical technique to find the approximate solutions of physical problems represented by the partial differential equations with well defined the boundary conditions. For the FEM analysis in a domain there are four major steps: 1. Discretization into sub-domains or elements, 2. Deriving the differential equations in the element, 3. Assembling all the elements into the solution domain and 4. Solving the system of differential equations by applying the boundary conditions. Now we briefly describe the each steps of the FEM process by a qualitative analysis of electromagnetic problems [54, 55].

1. Consider an arbitrary object where we want to find some electromagnetic quantities. We first derive the domain of interest into sun-domains or elements as shown in Fig. 1.11. We see that if the number of sub-domains are not sufficient then the discretized domain would be very roughly matched and the solution too would be very approximate. On the other hand, if the number of sub-domains are sufficiently large, then the descretized domain would be better match the original domain and the solution would be

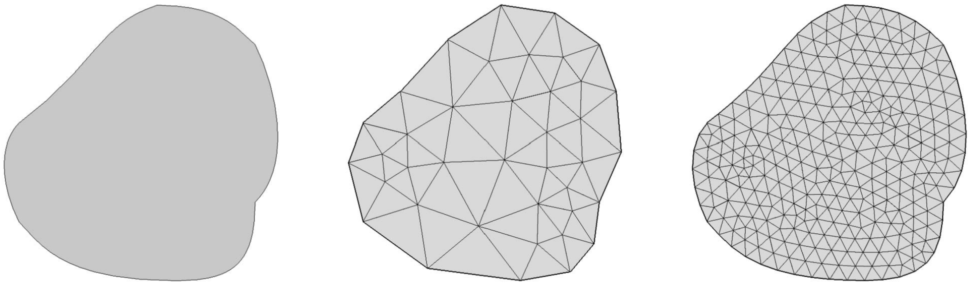
(a) (b) (c)

Figure 1.11: (a) An arbitrary shape domain for FEM analysis, (b) the domain of (a) is discretized in few number of sub-domains and (c) domain is discretized in large umber of sub-domains.

more accurate. Let V_i be the potential in the i^{th} element of the discetrized domains. The total potential of whole domain would be

$$V(x, y) = \sum_{i=1}^{N} V_i(x, y) \tag{1.5}$$

where N is the total number of the sub-domains. Most common forms of the potential for triangular mesh is

$$V_i(x, y) = a_2 x + a_1 y + a_0 \tag{1.6}$$

and for quadrilateral mesh is

$$V_i(x, y) = a_3 x + a_2 xy + a_1 y + a_0. \tag{1.7}$$

The triangular or quadrilateral mesh are chosen to minimize the irregularity of the descretized domain with the original one. In general, it is approximated that the potential V_i is zero outside of the i^{th} element. For the triangular mesh we assumed in Eq. (1.6) potential is linear but in general it may have some other variations also. The electric field associated with V_i would be

$$\vec{E}_i = -\vec{\nabla} V_i. \tag{1.8}$$

2. For triangular meshing, each element has three nodes. The potential for the i^{th} element would be the sum of the potential of each node of the i^{th} element. Using the Eq. 1.6 at each node, the V_i can be represented as

$$V_i = \sum_{j=1}^{3} \alpha_j(x, y) V_{ij} \tag{1.9}$$

where $\alpha_j(x, y)$'s are the coefficients associated with a_0, a_1 and a_2 of Eq. (1.6). The α_j's are the interpolation functions are called element shape functions and have properties like the Kronecker delta function. The energy per unit length of the element i can be obtained by surface integral of the electric field of Eq. (1.8)

$$W_i = \frac{1}{2}\varepsilon[V_i]^T[C^{(i)}][V_i] \tag{1.10}$$

where $C^{(i)}$ is a 3×3 matrix called element coefficient matrix and the superscript 'T' refers the transpose of a matrix. We have got the physical quantities for each element. Now there is a need of assembling the quantities for all element into the solution domain.

3. The energy of the whole domain can be written using the energy of the i^{th} element W_i as

$$W = \sum_{i}^{N} W_e = \frac{1}{2}\varepsilon[V]^T[C][V] \tag{1.11}$$

where

$$[V] = \begin{pmatrix} V_1 \\ V_2 \\ . \\ . \\ . \\ V_n \end{pmatrix}, \tag{1.12}$$

n is the number of node, N is the total number of descretized elements, and [C] is the global coefficient matrix derived from $[C_i]$ matrices. The next task is to find out the [C] to get the field information. In general, the matrix [C] is very big, but its elements have symmetry properties across the principle diagonal because of the some nodes being connected to each other. We see Fig. 1.11 that as the number N increases the nodes will increase and it will take more time and computation to solve. Now we shall apply some other constraints to get the coefficient matrix.

4. From the calculus of variations, we know that the Laplace's equation is satisfied when the energy of the whole system is a minimum. So the partial derivative of energy W with respect to the potential at each node will be zero

$$\frac{\partial W}{\partial V_k} = 0, \quad k = 1, 2, ..., n. \tag{1.13}$$

Using the Eq. (1.11) in Eq. (1.13), we get the following expression

$$\sum_{i=1}^{n} V_i C_{ik} = 0, \tag{1.14}$$

where n is the number of nodes in the mesh of the discretized domain. This is a general expression. If we write the this expression for all nodes, then we get the set of n partial differential equations in N unknowns, which we have to solve simultaneously to get [V]. There are several methods such as the iteration method [56], matrix method [57] etc. which can be used to solve the system of partial differential equations.

We have given a general qualitative description of the FEM analysis. Solving manually such large system of equations of system is not possible, particularly, if the discretized elements are very large or the system is highly complex. Now-a-days, there are several software packages that have been developed to solve such type of problems working on the principles of FEM. We have used the COMSOL Multiphysics, a commercial simulation software based on FEM to model our metamaterial structures. In the next section, we introduced briefly about this software.

1.6 Modelling in COMSOL Multiphysics

In COMSOL, there are different types of physical problems such as mechanical, chemical, electromagnetics, thermal etc., individually or in coupled form, that can be modeled using the different modules. Some major steps of modelling in COMSOL Multiphysics are listed below:

1. Choosing the appropriate module
2. Drawing the geometry of the system domain
3. Filling the domain with material parameters
4. Applying the appropriate boundary conditions
5. Setting the study parameters such as frequency, wavelength etc, and computation
6. Meshing or discritization of the domain
7. Results analysis such as field plotting, mode analysis, eigenvalues etc.,

For the study of electrodynamics problems, we can choose the Radio Frequency (RF) module and for optics problems Wave Optics module or RF module. After choosing the regime of the physics we have to draw the geometry either 2D or 3D. Externally made CAD geometry from other softwares also can be imported into COMSOL Multiphysics. The MATLAB software is fully integrated with COMSOL Multiphysics. The problems script written in MATLAB can be loaded in COMSOL Multiphysics for simulation. If 3D problems takes much time to be solved than the 2D problems, depending on the available symmetries, the 3D problems can be projected into 2D geometries to reduce the computation time and memory required.

After drawing the geometry of the problem, we need to feed the material properties in the volumes of the geometry or sub-geometries. Different kinds of predefined material parameters are given in COMSOL Multiphysics, but the external material data called user defined data can be also loaded. The user defined material data can even be parametrized, spatially or temporally. When the material parameters have been fixed, then there is need of applying the appropriate boundary conditions. We have carried out electromagnetic simulations for our analysis. So from now onward for discussion of simulation in COMSOL Multiphysics, we will focus only on RF module. In the RF module, there are several types of boundary conditions that are available in COMSOL Multiphysics. One should be very careful in applying the boundary conditions, otherwise slightly changing them will result in inappropriate solutions. For example, if there is any metallic or magnetic materials in the domain then we can use perfect electric conductor (PEC) or perfect magnetic conductor (PMC) boundary conditions. For radiating problems, the scattering boundary conditions or perfectly matched layer (PML) boundary conditions are good [58–61]. Most of the metamaterial structures are periodic, in which case, the periodic boundary conditions or Floquet boundary conditions [60, 61] are appropriate.

After fixing the boundary conditions, the next important step is the meshing or discritization. Depending on the size of sub-geometries, the incident frequency, metamaterial element and space symmetry, there is need to properly mesh the computational domain. Simulation of 3D problems are more difficult than the 2D problems because for the same size of meshing in 3D model the number of elements increases exponentially compared to 2D model and hence the computational time and memory increase drastically. So if possible, it is always preferable to use a 2D model instead of a 3D geometry. Once the meshing is done, the simulator is ready to solve or compute the problem. There are different types of solver such as stationary solver, time-dependent solver, eigenvalue solver etc. in COMSOL Multiphysics. The solvers compute almost all the related physical parameters. After the simulations, there is a need to analyze the results by plotting, calculating various quantities etc.

To benchmark the COMSOL computation, we considered an example of dielectric circular waveguide from a book ‘Advanced Engineering Electromagnetics’ [62]. A lossless dielectric circular waveguide of radius 1.3457 cm and dielectric constant 4 is surrounded by a perfect perfect electric conductor. Analytically, its cutoff frequencies for the TE_{11} and TM_{01} modes are 3.2664 GHz and 4.2664 GHz respectively. We simulated this example in COMSOL Multiphysics using the RF module’s eigenfrequency module. For the waveguide modal analysis, the COMSOL solves the following equation

$$\vec{\nabla} \times \mu_r^{-1} \left(\vec{\nabla} \times \vec{E} \right) - k_0^2 \left(\varepsilon_r - \frac{i\sigma}{\omega \varepsilon_0} \right) \vec{E} = 0, \tag{1.15}$$

where all symbols are in standard notations. The Eq. (1.15) is a general form of the

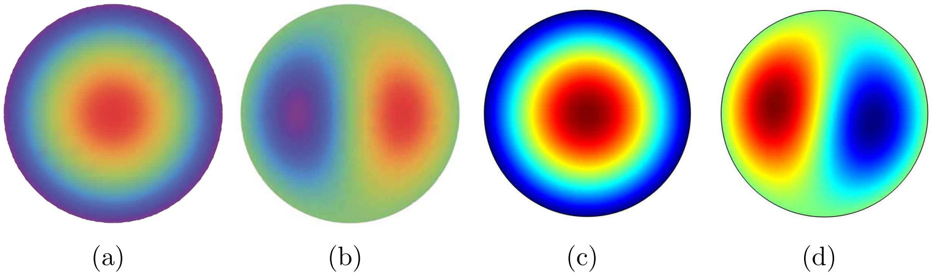
(a) (b) (c) (d)

Figure 1.12: The normalized plots of the field component E_z for TM_{01} and TM_{11} modes at 10 GHz frequency. (a) and (b) are obtained by analytical calculations, $\beta/k_0(\mathrm{TM}_{01})$=1.8088 and $\beta/k_0(\mathrm{TM}_{11})$=1.4668. (c) and (d) are obtained by COMSOL simulation, $\beta/k_0(\mathrm{TM}_{01})$=1.8091 and $\beta/k_0(\mathrm{TM}_{11})$=1.4677.

Maxwell curl equation. COMSOL calculates all the related parameters with boundary conditions. The computed cutoff frequencies for TE_{11} and TM_{01}modes are 3.2641 GHz and 4.2633 GHz respectively. At 10 GHz frequency, analytically calculating the effective propagation constant (β/k_0) for TM_{01} and TM_{11} modes, we obtain the eigenvalues as 1.8088 and 1.4668 respectively, and COMSOL obtained β/k_0 for TM_{01} and TM_{11} modes as 1.8091 and 1.4677 respectively. The normalized field component E_z for TM_{01} and TM_{11} modes are plotted in Fig. 1.12. The analytical and computed cutoff frequencies and effective propagation constants almost match exactly with a very small error since the FEM analysis gives only the approximate solutions. Error may depend on the limitations of boundary conditions, size of meshing and the solver.

1.7 Thesis Organization

The present Chapter 1 introduced the basics concepts of metamaterials, classifications, nanoporous alumina fabrication techniques, nanowire metamaterials, metamaterial waveguides and FEM modeling techniques. The organization of the rest of the chapters of the thesis is given below.

Chapter 2 discusses the details of the experimental aspects of the fabrication of the metamaterials using nanoporous alumina templates. In this chapter, description of the fabrication of planar and cylindrical nanoporous alumina templates, and their structural and morphological characterization will be given. The deposition of metallic nanowires in these templates also will be described.

Chapter 3 will show the homogenization of cylindrical metamaterials made by cylindrical nanoporous alumina templates. We use the technique of transformation optics and local Maxwell-Garnett homogenization (MGH) theory to homogenize the cylindrical metamaterials.

Chapter 4, we approximate that our cylindrical nanoporous alumina are homogeneously filled. Using this approximation we discuss the properties of anisotropic waveguides that are homogeneously filled, and cylindrical anisotropic nanoporous alumina coaxial and hollow fibers.

In Chapter 5, we relax the assumption of the homogeneously filled condition used in the Chapter 4. We discuss the waveguide properties of the radially inhomogeneous and anisotropic nanoporous alumina coaxial and hollow fibers. In this chapter, we discuss the light transmission also in the inhomogeneous and anisotropic nanoporous alumina fibers.

Chapter 6 will discuss the scattering applications of the planar and the cylindrical nanoporous alumina templates. In this chapter, first we discuss the polarization dependent light scattering properties and fluorescence properties of the planar nanoporous alumina which have linearly organized or disorganized nanopores. Later in this chapter, we give the analysis of the light scattering and fluorescence properties of cylindrical nanoporous alumina.

Chapter 7 summarizes the thesis and discusses future possible areas of research with planar and the cylindrical nanoporous alumina.

Chapter 2

Fabrication of Nanoporous Alumina Templates

2.1 Introduction

In the introductory Chapter 1, we have discussed the basics of nanoporous alumina. The anodization technique is known since decades [42, 63, 64] for fabricating large areas of nanoporous alumina with high aspect ratio pores from aluminium sheets. The possibility of structural modification of nanopores in the nanoporous alumina makes it a very flexible system for creating templates to deposit other materials. This technique has been also used to make highly anisotropic nanowire metamaterials [28] but is in the planar geometry. Nanoporous alumina in the cylindrical geometry has been rarely reported [65–67] and have been used for chemical catalysis [65, 66]. Alumina membrane microtubes for use as low friction hypodermic needles has also been reported [67]. In the previous reports, only alumina membrane tubes with large diameters have been used. The anodization of cylindrical aluminium wires with diameters of sub-hundred micrometer, and their detailed structural characterization and optical properties were not known. Nanoporous alumina in the cylindrical geometry have very different properties from the usual nanoporous alumina in their structural and anodization characteristics. Our main interest in the thesis are microwires of nanoporous alumina. In this chapter we shall discuss the details of the fabrication of the nanoporous alumina in planar and cylindrical geometries, their structural characterization and deposition of nanowires into the porous templates. The structural characterization has been carried out by using field emission scanning electron microscope (FESEM), focused ion beam (FIB) and optical microscopy. In this chapter, it is shown how the cylindrical nanoporous alumina is structurally different from planar nanoporous alumina. Later on, silver metal deposition has been carried out with both types of nanoporous alumina. The electrodeposition of silver nanowires in the nanopores of planar nanoporous alumina is easy because the barrier layer can be easily removed and the nanopores are uniform throughout the volume. It is, however, very difficult in case of cylindrical nanoporous alumina as the barrier layer directly can not be removed and the nanopores diameter decreases radially towards the center.

2.2 Anodization of Aluminium Planar Sheet

A home made anodization holder, made of delrin polymer, has been used to anodize the aluminium sheet. The anodization holder and setup are shown in Fig. 2.1. A photograph of the anodization holder (component wise) is shown in Fig. 2.1(a) and the assembled form of the holder is shown in Fig. 2.1(b). The anodization setup is schematically shown in Fig. 2.1(c). An Aplab regulated DC power supply (model:L1281) has been used in the electropolishing, anodization and electrodeposition processes.

2.2.1 Nanoporous Alumina with Highly Organized nanopores

Anodization

Templates were fabricated by a two-step anodization process. Aluminium sheets of 99.999% purity (Alfa Aesar) were cleaned in acetone and then annealed at temperature 500 °C in vacuum to increase the gain size. The annealed sheets were electropolished in a

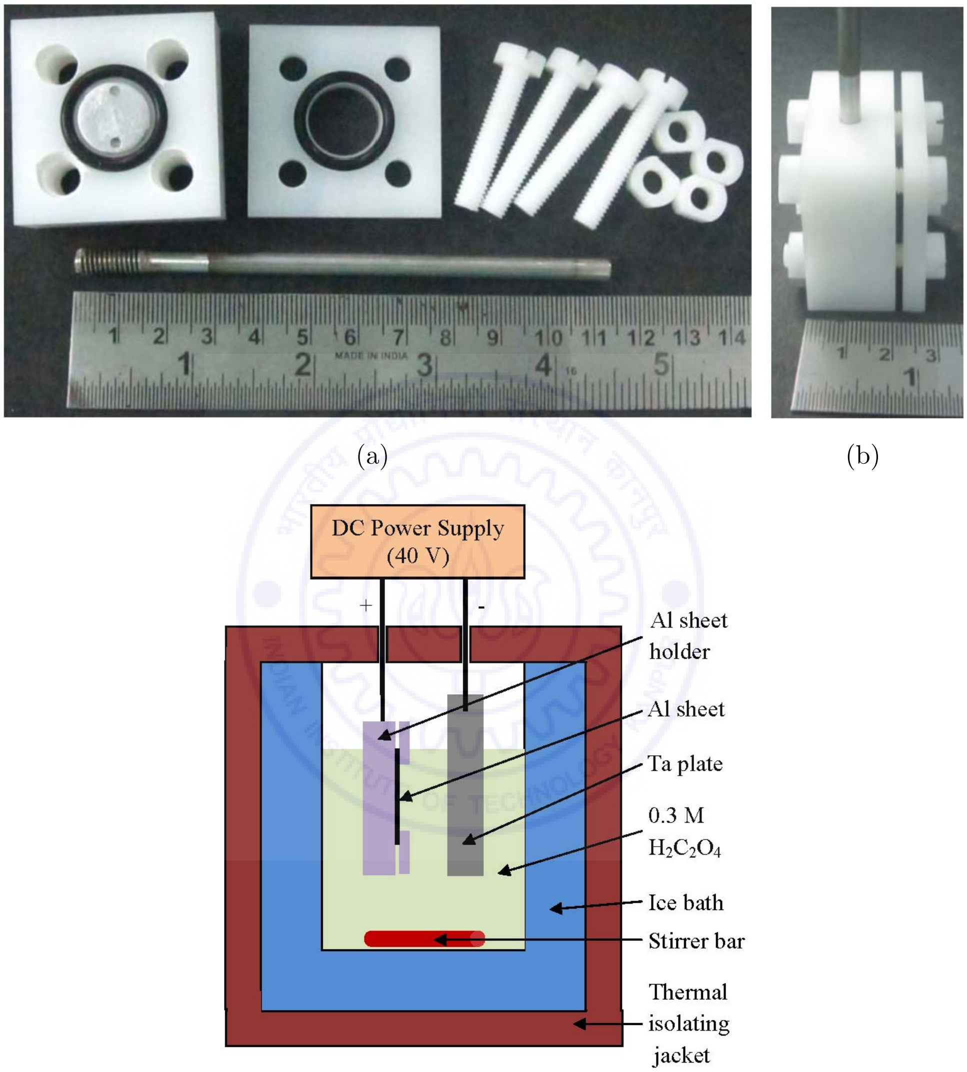

(a) (b)

(c)

Figure 2.1: The photograph of the anodization holder and anodization setup to anodize the aluminium sheet. (a) the components of the holder, (b) the parts of holder are assembled and (c) the anodization setup schematic for anodization of the aluminium sheet.

mixture of ethanol and perchloric acid in 5:1 volume ratio at 0.076 A/cm^2 current density for three minutes [68–70]. After electropolishing a very smooth mirror like shiny surface was obtained which is very necessary to get straight nanopores. The electropolished aluminium sheets were anodized in 0.3 M oxalic acid at 40 V at 0 °C for half hour [42, 46]. Since the anodization is an exothermic process, we used the ice bath to keep temperature of the system constant at 0 °C. A tantalum (Ta) plate used as the counter electrode. During anodization, the solution was continuously stirred using a magnetic stirrer to keep the solution temperature uniform. The alumina synthesized in the first anodization process was etched off in a mixture of chromic acid (9 gm), phosphoric acid (7 ml) and deionized (DI) water in a 200 ml solution at 90 °C [46, 48, 68]. The alumina etched sample was once again anodized in 0.3 M oxalic acid. In the second anodization process, all the parameters were maintained the same as for the first anodization. The second anodization time was varied as per need. From the anodized sheets, the remaining aluminum was removed by dissolving in a mixture of hydrocloric acid (100 ml), cupric chloride (3.4 gm) and water in 200 ml solution. The duration of the alumina etching after the first anodization and the aluminium etching after second anodization depend on the thickness of the alumina and aluminium, which we have to optimize for the particular thickness. Pore widening and barrier layer removal was carried out in 5% phosphoric acid.

Structural Characterization

In Fig. 2.2, a schematic picture of the anodization of plane aluminium sheet is shown. In nanoporous alumina, the nanopores ideally have a hexagonal arrangement, and the diameters of the nanopores are uniform throughout. The nanopore organization, nanopore diameter and interpore distance depend on the purity of the aluminium sheet, the surface roughness of aluminium sheet, the nature of electrolyte, applied voltage or current, temperature of the solution, the first anodization duration. FESEM images of planar nanoporous alumina are shown in Fig. 2.3. It can be seen in Fig. 2.3(a) that the nanopores are arranged almost perfectly in hexagonal order. The size of nanopore is

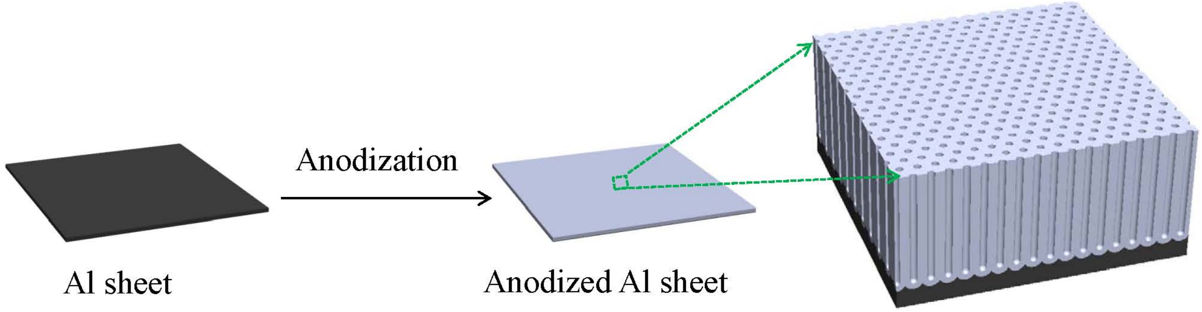

Figure 2.2: A schematic for the planar nanoporous alumina. Nanopores are in hexagonal arrangement and uniform size throughout.

uniform throughout as shown in Fig. 2.3(b).

2.2.2 Nanoporous Alumina with Linearly Organized Nanopores

The organization of the nanopores in the planar nanoporous alumina is affected by the surface topography and the surface stress on the aluminium sheet. The pores can be forced to form in a different order by using pre-patterned aluminium surfaces and subsequent anodization. Techniques such as focused ion beam milling, electron beam lithography or nano-imprint lithography have been used to obtain the pre-patterned aluminium surface [46, 71–75].

Anodization

The planar nanoporous alumina with linearly organized pores were fabricated using the following steps: pieces of Aluminum sheet of 99.9 % purity (Loba Chemie, India) were cleaned by sonicating for 10 minutes in acetone. The cleaned aluminum sheet was then electropolished for 5 minutes in an electrolyte solution containing perchloric acid and ethanol in proportion of 1:5 by volume. A current density 0.076 A/cm^2 was maintained during the electropolishing process. The polished surfaces with mirror-like finish were

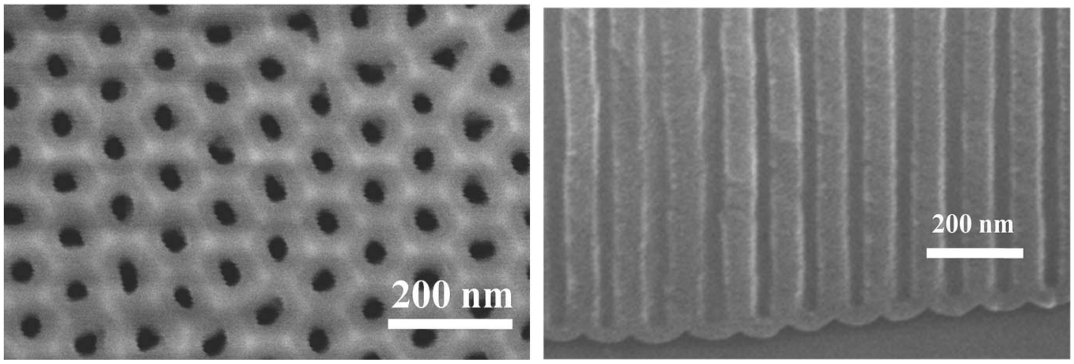

(a) (b)

Figure 2.3: FESEM images of the planar nanoporous alumina prepared in 0.3 M oxalic acid solution at 0 °C. (a) the top view show the nanopores arrangement and (b) the cross section in which the nanopores are uniform throughout.

rinsed in deionized water and used for the subsequent anodization process. Some electropolished aluminum surfaces were deliberately scratched by a steel needle along straight lines resulting in micro scratches on the surfaces. Anodization was carried out on three kinds of surfaces: (i) electropolished, (ii) electropolished and scratched surfaces, (iii) unpolished. For reference, we also anodized a high purity aluminium sheet 99.999 % (Sigma Aldrich) without any electropolishing as well as after electropolishing. The anodization was carried out for 12 hours in aqueous solution of oxalic acid (0.3 molar) at 40 volts. The solution temperature was maintained at 18°C throughout the experiment. A magnetic stirrer at 300 rmp was used to continuously stir the solution.

Structural Characterization

The surface morphology of the fabricated planar nanoporous alumina was characterized by using FESEM. The surface structures of the templates prepared with various surfaces are shown in Fig. 2.4. Figure 2.4(a) shows templates grown by the anodization of rough aluminium sheet without prior electropolishing, Fig. 2.4(b) shows templates grown by the anodization of electropolished smooth surfaces, and Fig. 2.4(c) shows templates grown

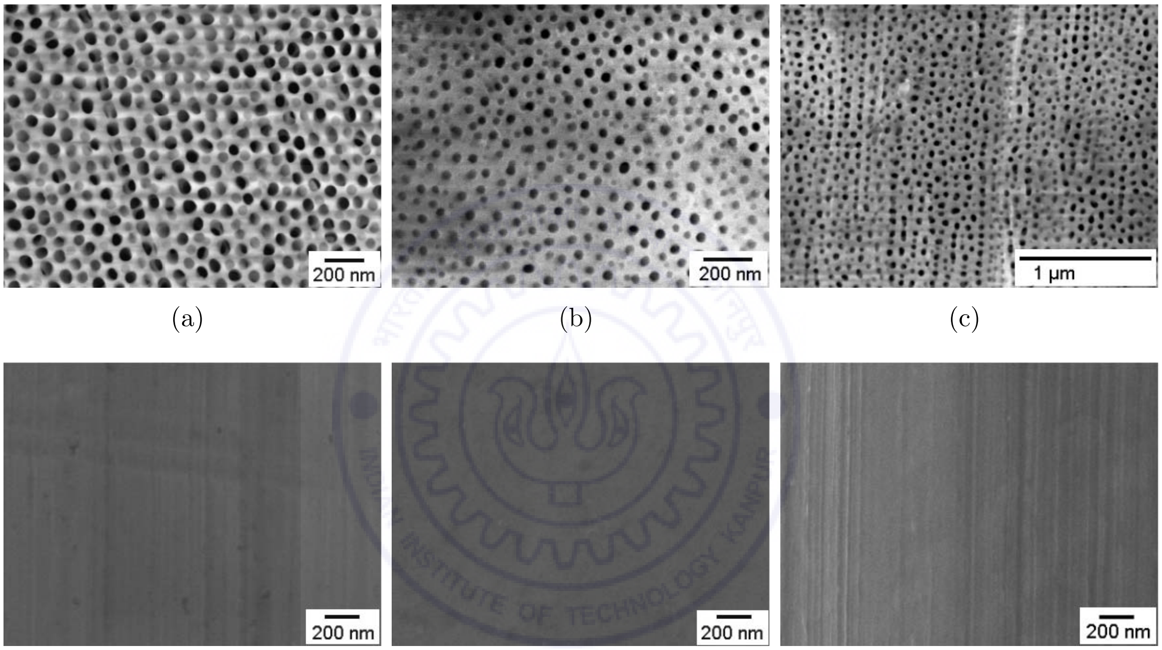

(a) (b) (c)

(d) (e) (f)

Figure 2.4: FESEM images of planar nanoporous alumina obtained by anodization of aluminium sheet: (a) anodized surface without electropolishing, (b) anodized surface after electropolishing and (c) electropolished and scratched surface that has been subsequently anodized. The corresponding images of the surfaces of the aluminium sheet, obtained before anodization, are also shown in (d), (e) and (f) respectively, for comparison.

by anodization of electropolished and subsequently scratched aluminum sheets. For reference, the corresponding SEM images are shown in Fig. 2.4(d) of the rough aluminium sheet, in Fig. 2.4(e) of the smooth aluminum surface after the electropolishing, and Fig. 2.4(f) of the electropolished and scratched aluminum surface, respectively. It is observed that the anodization of the rough aluminum sheet without electropolishing resulted in pores arranged linearly in a stripe like fashion. This is because the aluminium sheet is usually produced by a rolling process that creates scratches along the rolling direction due to the embossing of features from the rolling directions and is possibly also anisotropically stressed. This feature becomes absent when the aluminum sheet is electropolished and subsequently anodized. Figure 2.4(b) shows randomly oriented pores that are obtained when the aluminium sheet was electropolished and subsequently anodized. The originally present scratch lines get removed by the electropolish process and the surface becomes very smooth Fig. 2.4(e). Finally the anodization on the electropolished and intentionally scratched aluminum sheet resulted in the organization of pores along oriented lines. The pores are aligned along the scratching direction as can be seen in Fig. 2.4(c). The intentional scratching lines are visible on the reference image obtained after the electropolishing and scratching steps Fig. 2.4(f). The intentional scratch lines have concave surfaces in the interior of the grooves and the local electric field density during anodization should be very small at the bottom [76]. Similarly, large electric fields will be present at the edges of the grooves due to the convexity with large curvature. Therefore, the anodization is more effective and faster along the edges of the grooves compared to other regions. This results in a linear organization of the pores along the grooves. The anodization without scratching the sheet resulted in randomly oriented pores, as there is no preferred direction on the electropolished surface. The high purity (99.999 %) aluminium sheets after electropolishing and two step anodization processes yield a highly ordered hexagonal array of nanopores. It might be mentioned that by controlling the orientation of the scratching marks one could obtain pores arranged on the over large areas, which might be carried out by a mechanical burnishing operation.

2.3 Anodization of Aluminium Microwire

2.3.1 Anodization

The aluminium microwire was directly anodized using the two step anodization method. There was no holder used and we directly suspended the aluminium microwire into the solution. At the solution-air interface, we painted the microwire with lacquer to protect the aluminium from the fast reaction at the interface. Otherwise, portion of microwire at solution-air interface get complete anodization very fast and stop the electrical contact to anodize the immersed portion of the microwire. A schematic of anodization setup has been shown in Fig. 2.5. Aluminium microwires of 99.999% purity, and diameters 100 μm and 250 μm were purchased from Alfa Aesar company. The aluminium wires were cleaned in acetone prior to the vacuum annealing at 500 °C for three hours to increase the grain size. The annealed wires were anodized in 0.3 oxalic acid solution made in DI water. A tantalum (Ta) plate was used as the cathode. The system temperature was kept at 0° C using an ice bath. Here we did not stir the solution because the wires were thin and a small flow or turbulence could deform them. The first anodization time was kept to be 30 minutes. After the first anodization, the alumina was etched away as in the case of the aluminium planar sheet anodization. Second anodization was performed at the same physical parameters as was done for the first anodization. The aluminium core from the anodized wire was removed in the aluminium etching solution as was for the plane sheet anodization. After the aluminium core removal, we obtained a hollow cylinder of nanoporous alumina (cylindrical shell). Here 5% phosphoric acid used to carry out the pore widening of the anodized wires.

2.3.2 Structural Characterization

A schematic picture of the anodized microwire is shown in Fig. 2.6, while the FESEM images of the obtained nanoporous alumina microtubes are shown in Fig. 2.7. If the surface

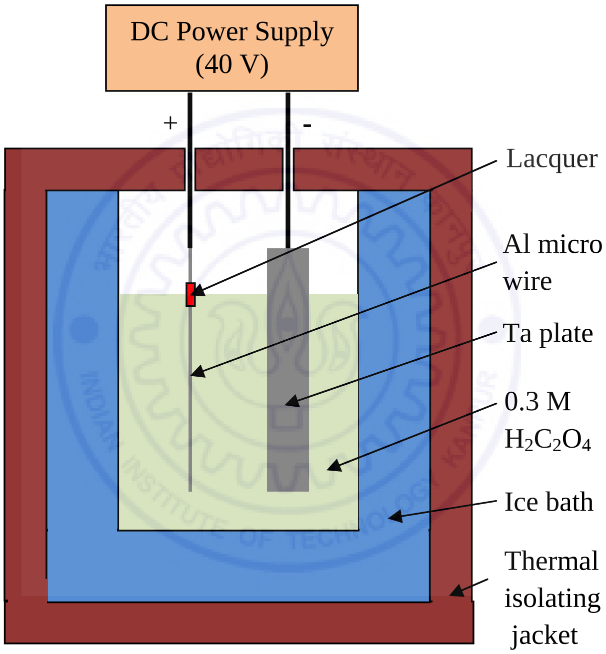

Figure 2.5: A schematic of the anodization setup to anodize the aluminium microwire.

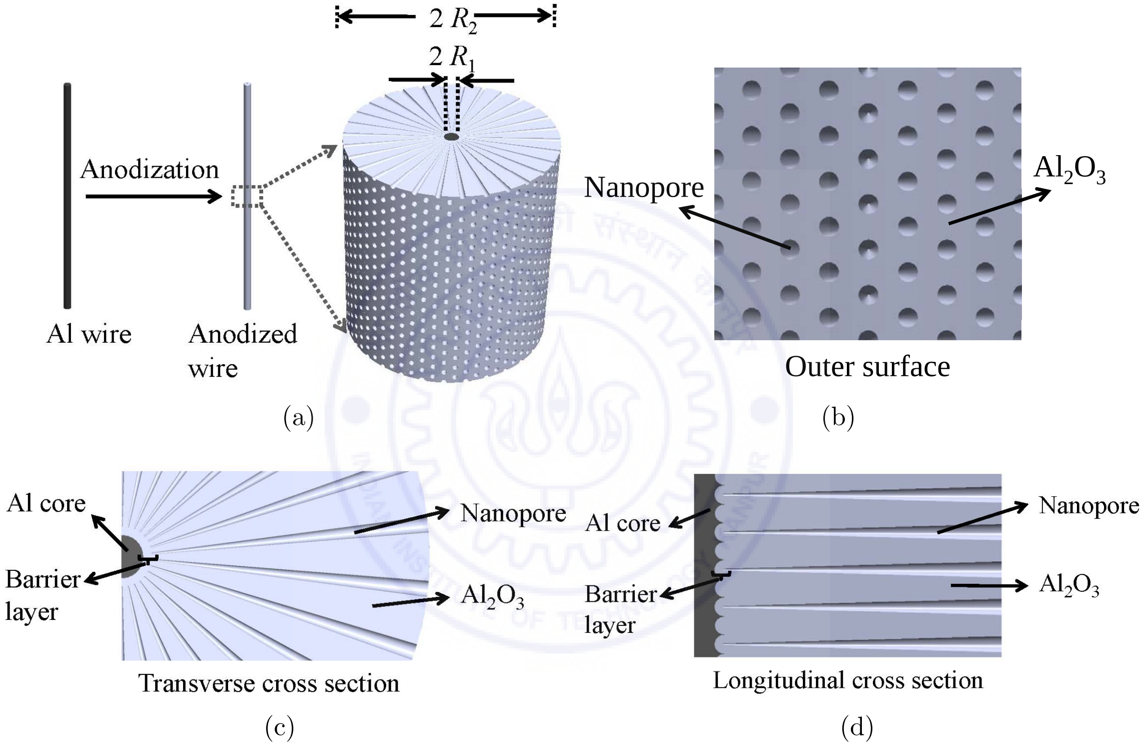

Figure 2.6: Schematic of the structure of the cylindrical nanoporous alumina. (a) anodizing aluminium microwire, (b) outer surface of the anodized wire, (c) the transverse cross section of the anodized wire and (d) the longitudinal cross section of the anodized wire.

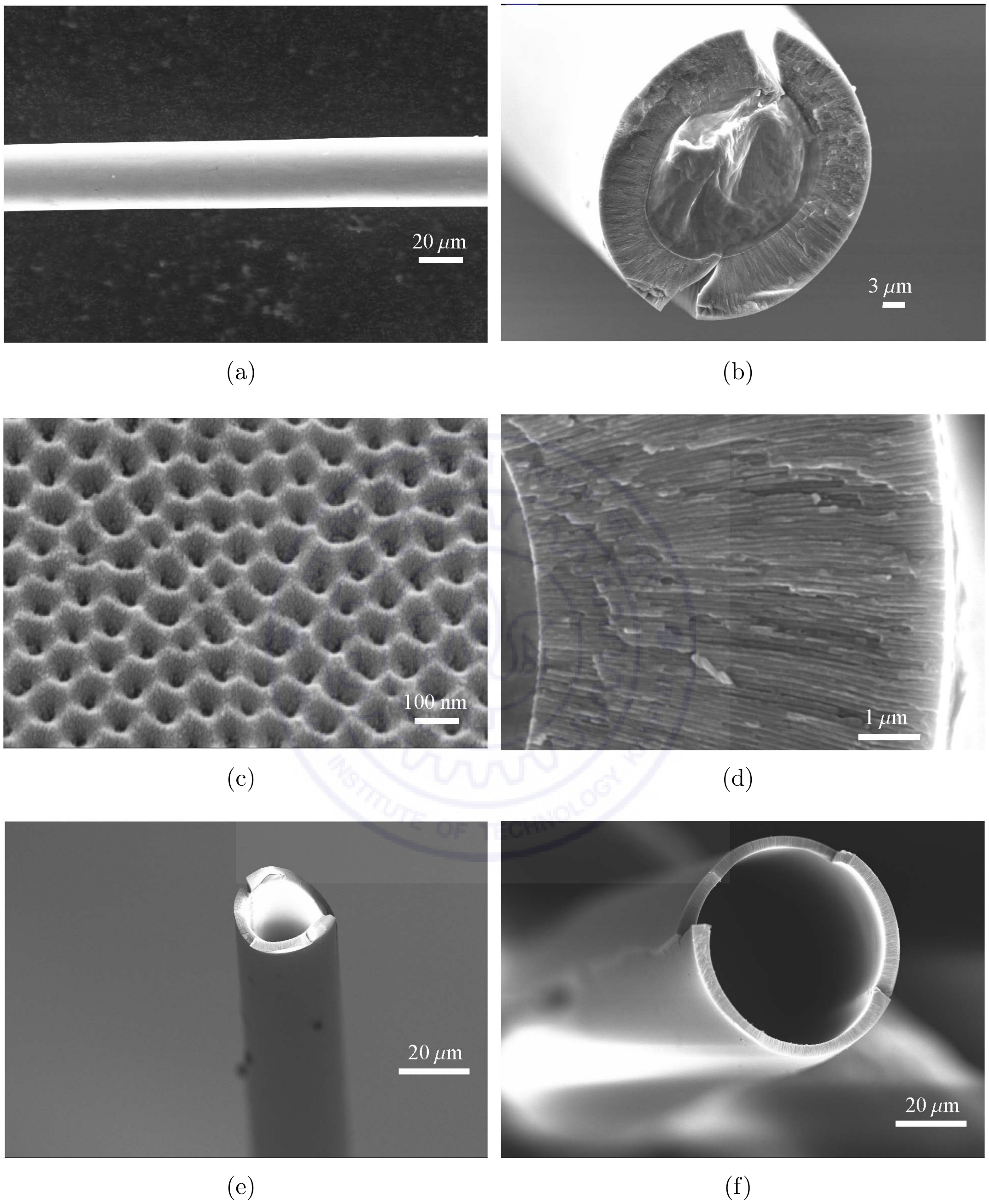

(a) (b)

(c) (d)

(e) (f)

Figure 2.7: FESEM images of (a) electropolished aluminium wire, (b) anodized wire, (c) outer surface of the anodized wire, (d) transverse cross section of the anodized wire. Images (e) and (f) are of hollow nanoporous alumina microtubes of small and large diameter respectively.

is not smooth then the nanopores might merge with each other. The smooth surface of an electropolished aluminium wire is shown in Fig. 2.7(a). The anodized microwire is shown in Fig. 2.7(b), where the nanoporous alumina shell contains an aluminium core. The shell thickness can be increased by increasing the anodization time. In Fig. 2.7(c), the outer surface of the cylindrical nanoporous alumina is shown. The average pore diameter is about 30 nm and the interpore distance is about 100 nm. A zoomed image of the cross section of the alumina shell in Fig. 2.7(d) shows the straight nanopores with decreasing diameter towards the center of the microtube. It can be noted that the nanopores do not merge. After the removing the aluminium core from the anodized wire we got nice hollow nanoporous alumina microtubes. Figures 2.7(e) and 2.7(e) show a small and a larger diameter nanoporous alumina microtubes. We succeeded in removing the aluminium core from the anodized microwire up to two centimeters length approximately. Removal of the aluminium core from longer lengths would take more time in the etching solution, and along with the aluminium core the alumina shell also tends to get dissolved into the solution and get damaged. This process requires further optimization for use on longer wires.

To confirm the reducing size of nanopores towards the center of the wire, we cut out a $22\times4\times12$ μm^3 volume from the anodized nanoporous alumina as shwon in Fig. 2.8(a) and took the image at outer surface at a depth of 12 μm using FIB. We found that the pore size decreases towards the center of the wire as shown in Fig. 2.8(b). It should be noted that the nanopores do not merge while converging towards the center. If the purity of aluminium is not high or if the surface of aluminium microwire is not very smooth, then the nanopores might merge with each other. In the case of cylindrical nanoporous alumina the nanopore diameter decreases, but nanopore remains circular to minimize the system energy as shown in Fig. 2.8(b). So the interpore distance decreases towards the center along the radial direction in a $r\phi$-plane (azimuthal plane), but it has to remain constant in the rz-plane (along the longitudinal direction). If the interpore distance does not remain constant along the longitudinal direction, then the nanopores would merge,

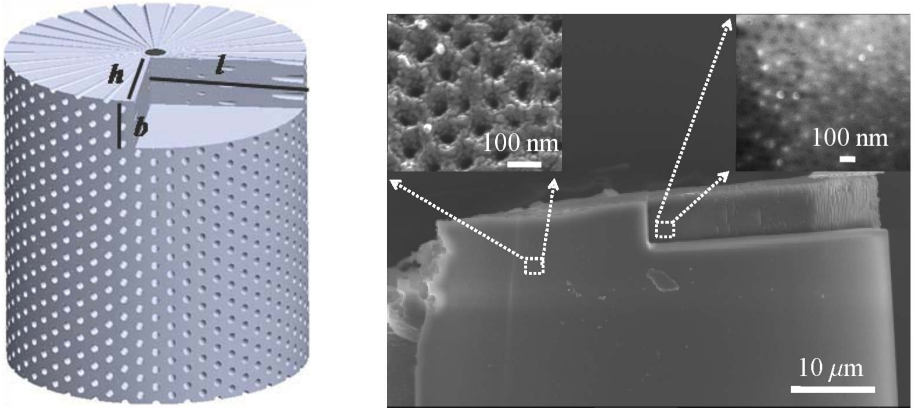

(a) (b)

Figure 2.8: (a) An schematic to mill out the part of the cylindrical nanoporous alumina to see the pore size with respect to radius of the wire and (b) corresponding the FESEM images of the milled out cylindrical nanoporous alumina.

which does not happen. This new feature of changing density of the nanopores makes the cylindrical nanoporous alumina structurally inhomogeneous as well as anisotropic. We had noted in the case of planar nanoporous alumina that the nanopore size remains constant throughout the volume and comparatively, the planar nanoporous alumina system is a homogeneous but anisotropic system. In later chapters, we shall model the optical properties of the cylindrical nanoporous alumina system where the structural anisotropy and inhomogeneity play a major role.

2.3.3 Effect of Radius of Curvature: Anodization Current and Crack Formation

We noted that during anodization of aluminium microwires, there was a crack can develop in the nanoporous alumina shell after some time. There was usually no crack in the planar nanoporous alumina sheet unlike this. We recorded the anodization current of aluminium microwires of diameters 50 μm, 100 μm, 220 μm, and an aluminium sheet. The recorded anodizations currents are shown in Fig. 2.9. The anodization current of aluminium microwires first increases quickly to a peak value and then decreases over time. While decreasing, a sudden small jump occurs in the anodization current beyond the peak value after some time and anodization current then decreases again. The time of jump in the anodization current of the microwires of diameters 50 μm, 100 μm and 220 μm were around 60 minutes, 70 minutes and 110 minutes respectively which can be seen in Figs. 2.9(a), 2.9(b) and 2.9(c) respectively (marked by the arrows). In comparision, the anodization current of the aluminium sheet after the peak value always decreases over time [63, 64, 77] and here there is no jump in the anodization current as shown in Fig. 2.9(d). This jump in the microwire anodization current occurs because of the formation of microcrack. When the crack occurs the effective resistivity between solution and aluminium microwire decreases and the anodization current slightly increases. For larger diameters of the microwires, the time at which the current changes rapidly shifted towards longer times. For the planar aluminium sheet the radius of curvature is effectively infinite and the anodization current remains steadily decreasing with no sudden changes.

In Figs. 2.10, two anodized wires of the same diameter have shown. Figure 2.10(a) is for 30 minutes anodization and there is no crack in the microtube. Figure 2.10(b) is for 70 minutes anodization, when sample had been taken out just after the jump in the anodization current occurred. We see that there a small crack in the nanoporous alumina shell. If the aluminium microwire is anodized for longer time, then the crack size also becomes larger. We know that the anodization starts perpendicular to the planar aluminium sheet surface and there is a volume expansion, as the volume of nanoporous alumina is much larger compared to the original volume of the aluminium [44]. In the case of the planar aluminium sheet anodization, the reactive area of aluminium always remains constant throughout the anodization while the volume of nanoporous alumina increases perpendicular to the sheet surface. So the cracks do not occur in the planar nanoporous alumina because its reactive area is always constant. In the case of anodization of the aluminium microwire the anodization starts perpendicular to the curved surface along the radial direction towards the center in the cylindrical symmetry. So the effective reactive area continuously decreases with radius and the relative volume expansion of the nanoporous alumina increases. Thus, the alumina is under tensile stress and also plastically deforms to some extent. Eventually with continued stress building up, a crack suddenly appears as the yield point is crossed. For the smaller diameter of the microwire the effective reactive area decreases faster compared to the larger diameter microwire, so the crack formation occurs earlier for microwires with smaller diameter.

2.3.4 Effect of Radius of Curvature: Organization of nanopores and Shell Thickness

To see the effects of the radius of curvature of the wire on the pore size, interpore distance and shell thickness, we anodized two different diameters wires, one of 25 μm and other 230 μm, for the same time. We observe that in both the anodized wires, the average nanopore size is 30 mn and the interpore distance is 100 nm at the outer surface, while there is difference in the nanoporous alumina shell thickness. For smaller diameter of the wire, the shell thickness was less than the shell thickness of the larger diameter wire. Figures 2.11(a) and 2.11(b) show the cross sections of the large 230 μm diameter anodized wire, and Figs. 2.11(c) and 2.11(d) show the cross section and outer surface of the anodized wire of diameter 25 μm.

Just after the anodization, for fixed anodization parameters, the pore diameters and interpore distance at outer surface remain constant for smaller and larger diameters microwires both. But the nanopores diameter can be increased by pore widening upto just lesser than the interpore distance. These two quantities, nanopore diameter and interpore distance towards the center along the radial direction vary faster with radius for smaller diameter microwires compare to larger diameter microwires. These quantities can be changed by changing the acid or the anodization parameters or both. In the same anodization time, the nanoporous alumina shell thickness is lesser for smaller diameter microwire compared to larger diameter microwire because the effective reactive area de-

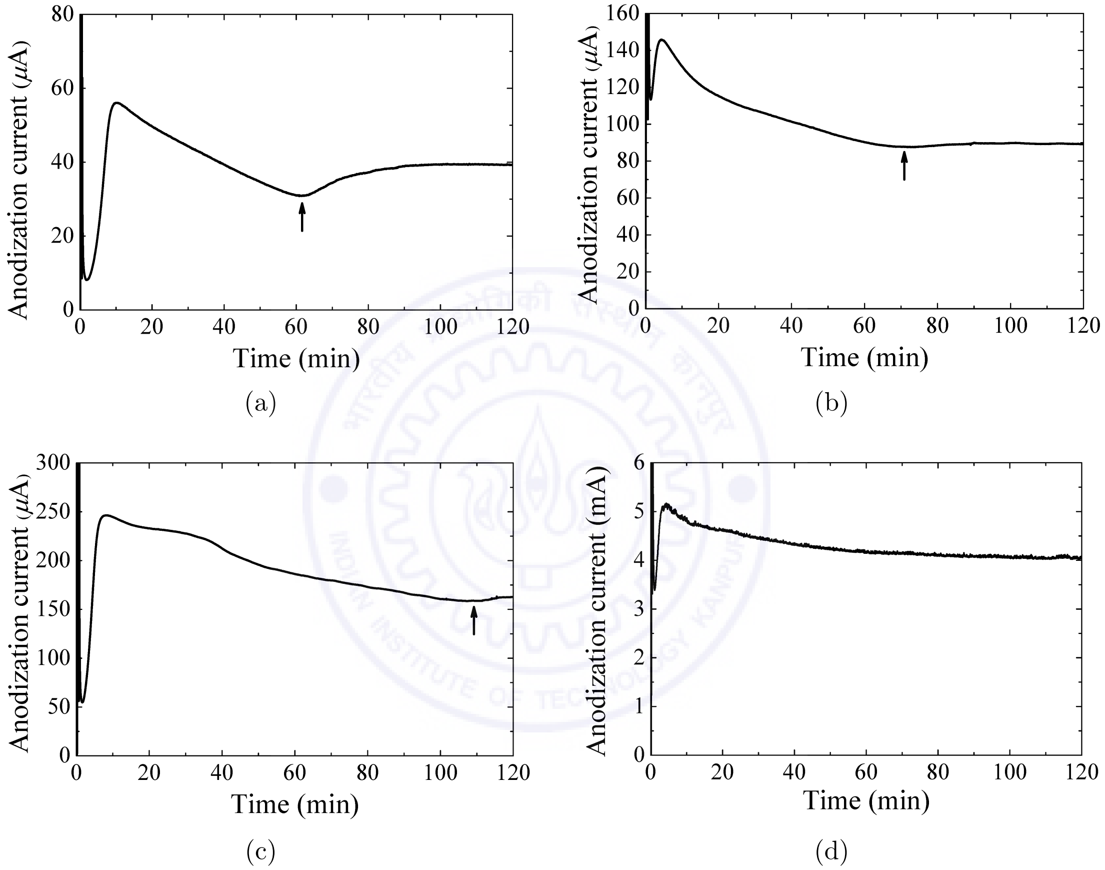

Figure 2.9: The measured anodization current of aluminium microwires of diameters (a) 50 μm, (b) 100 μm and (c) 220 μm. The small jump in the anodization current of anodization of aluminium microwires of (a), (b) and (c) occurred around 60 minutes, 70 minutes and 110 minutes respectively. (d) The anodization current of an aluminium sheet for reference. There is no jump in the anodization current of aluminium sheet anodization.

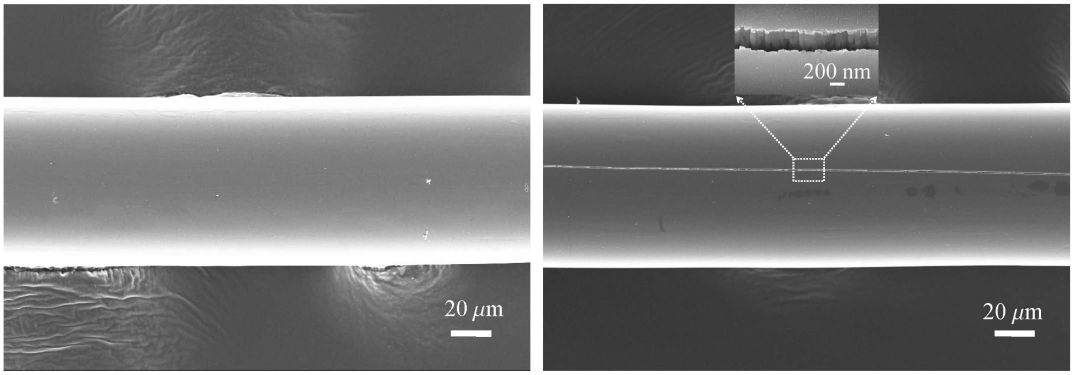

(a) (b)

Figure 2.10: FESEM images of anodized wire to show the crack formation in the nanoporous shell while anodization. (a) No crack for 30 min anodization and (b) sample just after the crack take place. The anodization time was 70 min.

creases faster. As the radius of curvature of microwire increases, the rate of change of the reactive area decreases and tends to zero value for infinite radius of curvature.

2.3.5 Optical Transparency of Nanoporous Alumina Microtubes

The alumina are transparent in the visible range. The nanoporous alumina are structured materials. To see the transparency of the nanoporous alumina shell, we took the optical reflection images of an electropolished aluminum microwire and a nanoporous alumina tube with an optical microscope (Olympus BX51). The optical reflection images of the aluminium microwire and the nanoporous alumina tube with a hollow core are shown in Figs. 2.12(a) and 2.12(b) respectively. We see that the light is highly reflected from the electropolished surface of the wire, while the nanoporous alumina tube is optically transparent. The air core is visible at the center in the microtube. Since these are transparent, therefore, the cylindrical nanoporous alumina with or without aluminium cores can be used as optical waveguides. The presence of a few surface inhomogeneities as well as some scattering enter in the nanopores alumina microtube can be seen. In the later chapters we shall discuss the optical waveguide properties of these cylindrical

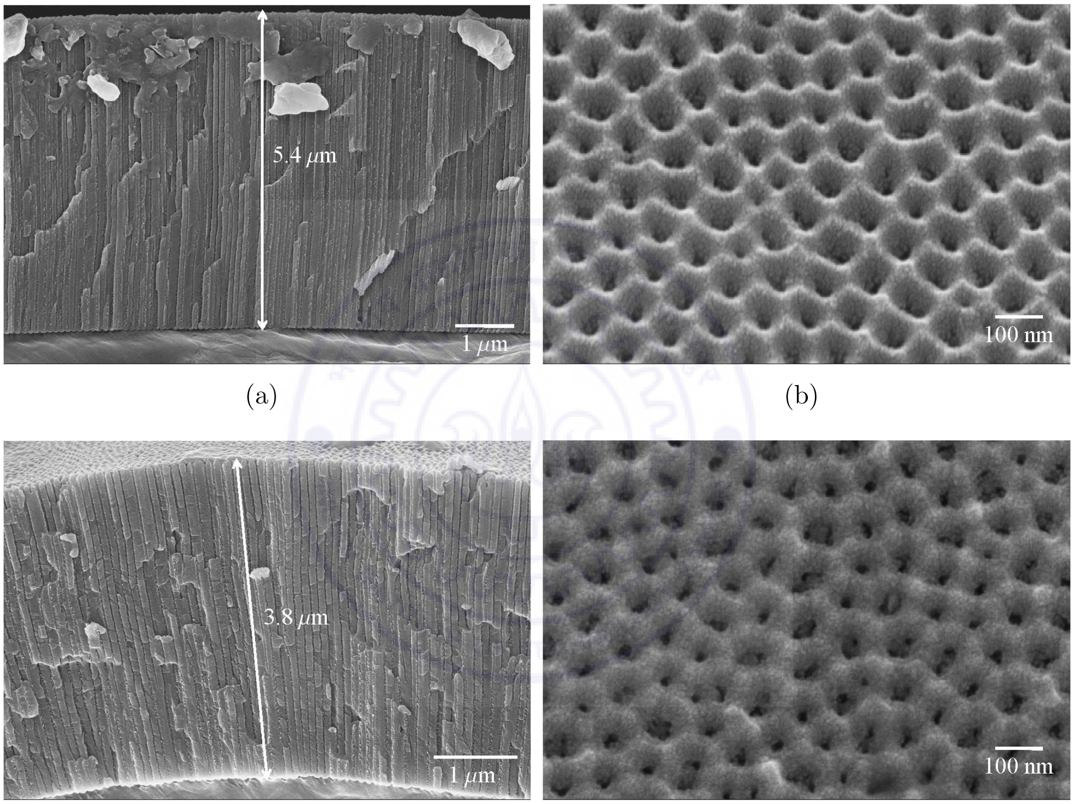

(a) (b)

(c) (d)

Figure 2.11: FESEM images of anodized wire to show the curvature effect on the nanopore size and interpore distance. (a) and (b) for large diameter, and (c) and (d) for small diameter.

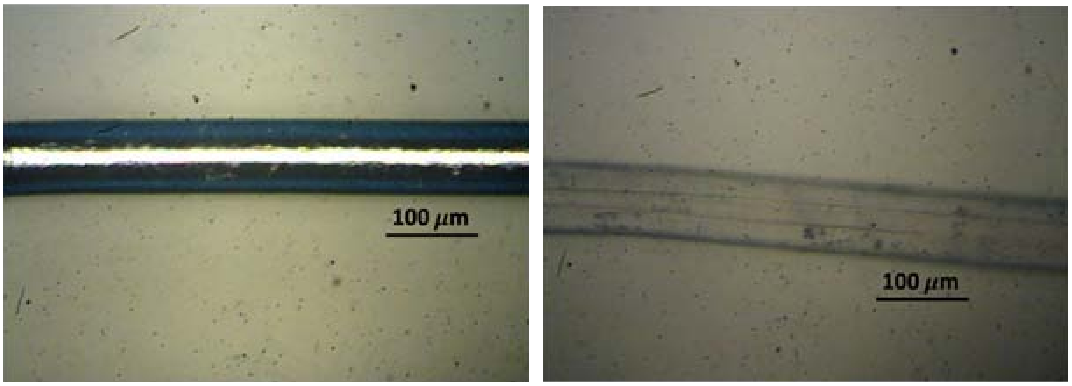

(a) (b)

Figure 2.12: Optical microscope images in reflection mode of (a) an electropolished aluminium wire and (b) anodized wire with hollow core.

nanoporous alumina for optical and infrared frequencies.

2.4 Metalization of Nanoporous Alumina

There are various kinds of materials such metals, oxides, polymers that can be deposited into the pores of the planar nanoporous alumina [28, 46, 71, 78]. Metalized nanoporous alumina have become very interesting to the scientific community after the development of the metamaterials [28, 78]. Several metals can be electrodeposited in the nanopores of the nanoporous alumina making it a popular template. This represents a readymade form of anisotropic or hyperbolic metamaterials. Among the metals, silver is highly preferred because of its plasmonic properties and less lossy nature. All the depositions so far have been made in planar nanoporous alumina templates, and growth of nanowires in cylindrical nanoporous alumina is not reported yet. In the next subsection, we present the deposition of silver nanowires deposition in planar nanoporous alumina, and in the subsequent subsection, in cylindrical nanoporous alumina microwires.

2.4.1 Nanowire Deposition into Planar Nanoporous Alumina

The electrodeposition is carried out with silver metal. After etching the aluminium from the anodized samples, the alumina template was immersed in 5% phosphoric acid at room temperature for 90 minutes to remove the barrier layer. During the barrier layer removal the nanopores were also widened by the acid. The front side of the template was coated with 160 nm gold film as a seed layer. As shown in Fig. 2.13(a) the gold coated template was kept on an aluminium foil and the all back and sides were covered with scotch tape. The gold coated templates were used as the cathode and a platinum wire as the anode. 0.2 M silver nitrate ($AgNO_3$) solution maintained in an ice bath was used as electrolyte to deposit the silver nanowires. Putting both the electrodes in the silver nitrate solution, a 30 mA current was passed for 40 minutes to electrodeposit the silver nanowires into the alumina templates. After the deposition, the scotch tape was removed for further characterization.

The Fig. 2.13(b) show the FESEM image of electrodeposited silver nanowires into the planar nanoporous alumina. The white dotted area of Fig. 2.13(b) is zoomed out Fig. 2.13(c). We can clearly see that the silver nanowires are deposited into the nanopores of the planar nanoporous alumina. The nanowires deposited in the pores of planar nanoporous alumina are broken at several places. Possibly there may be two reasons for broken nanowires. The first reason could be due to the lack of proper electrical contact between the gold thin film and the aluminium foil and the second reason is that we used the silver nitrate water solution only and we have not mixed any surfactant etc. to control the wettability of the system.

2.4.2 Nanowire Deposition into Cylindrical Nanoporous Alumina

The situation of cylindrical nanoporous alumina is quite different than the planar nanoporous alumina. Because the diameter of the cylindrical nanoporous alumina is sub-hundred mi-

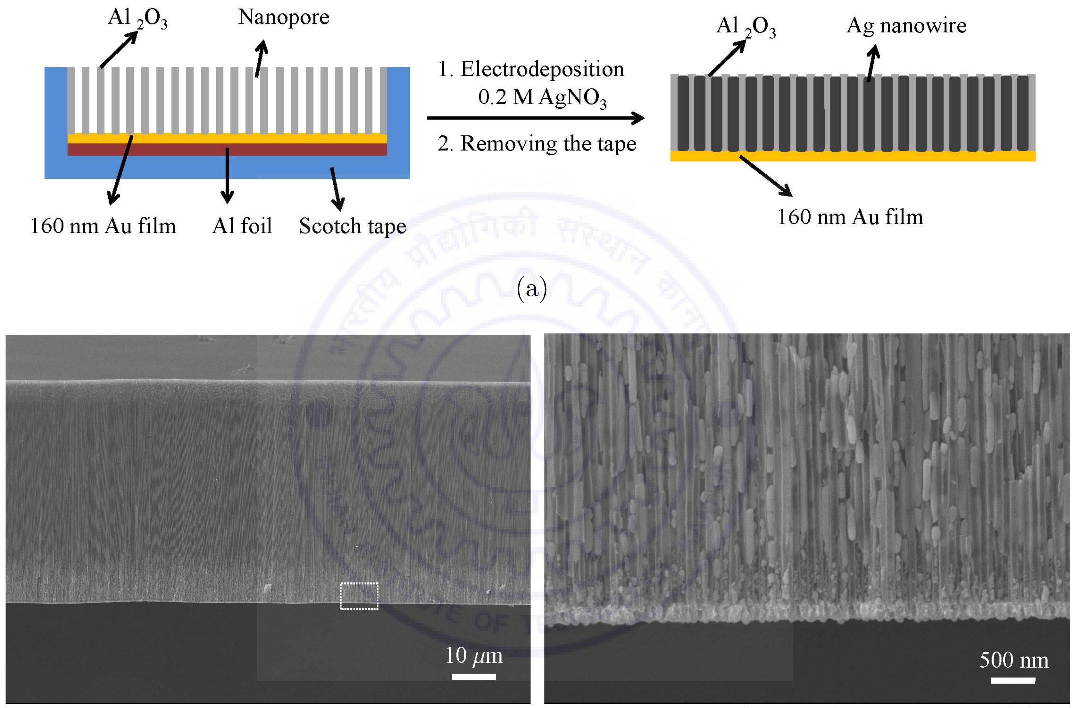

(a)

(b) (c)

Figure 2.13: FESEM image of Ag nanowires deposited into the pores of the planar nanoporous alumina. (a) A schematic to electrodeposition of Ag nanowire, (b) electrodeposited Ag nanowires and (c) the zoomed image of area of white dotted rectangle in (b).

crometer in size and we can not easily make a seed gold layer on the inner side of the template. But we have an aluminium core which can be utilized as a conducting electrode. To remove the barrier layer of impermeable alumina inside the cylindrical nanoporus alumina, the voltage after anodization was reduced slowly to zero. We reduced the voltage in steps of 5 V from 40 V to 5 V. After each voltage reducing step, 5 minutes was allowed to stabilize the anodization current. From 5 V to 0 V, we reduced the potential in steps of 1 V/min. After the anodization was completed, the templates were immersed in 5% phosphoric acid for half hour to remove the barrier layer completely. This process widened the nanopores size as well to some extent. The barrier layer removed cylindrical nanoporous alumina with aluminium core was used as the cathode and a platimum wire used as the anode. Both the electrodes were immersed in an ice cold electrolyte which was mixture of $AgNO_3$(3.5gm.), CH_3COONH_4(2.8 gm.), NH_3H_2O (25 % extra pure) (4.61 ml.) in 70 ml of solution [68]. A 3 mA current was applied for 40 minutes to deposit the silver nanowires.

Figure 2.14(a) shows a schematic of electrodeposited silver nanowires in the cylindrical nanoporous alumina. The silver nanowires are embedded in the alumina matrix. The FESEM image of the silver nanowires in cylindrical nanoporous alumina is shown in Fig. 2.14(b). This FESEM image is taken at the position white dotted area in Fig. 2.14(a). We see that there is an aluminium core and it is surrounded by the metal filled nanoporous alumina shell. The Fig. 2.14(c) is the zoomed image of Fig. 2.14(b) within the white dotted area. The presence of the silver nanowires were confirmed by the Energy-dispersive X-ray spectroscopy (EDX) as shown in Fig. 2.14(d).

We have thus succeeded in electrodepositing the silver nanowires into a very thin layer of the nanoporous alumina shell, where the shell thickness is small compared to the diameter of the aluminium wire. The reason is that as the shell thickness increases, the nanopore size decreases towards the center and it becomes very difficult to remove the barrier layer. In future, some other methods might prove successful to remove the barrier layer from the much thicker nanoporous alumina shell. Using the other method

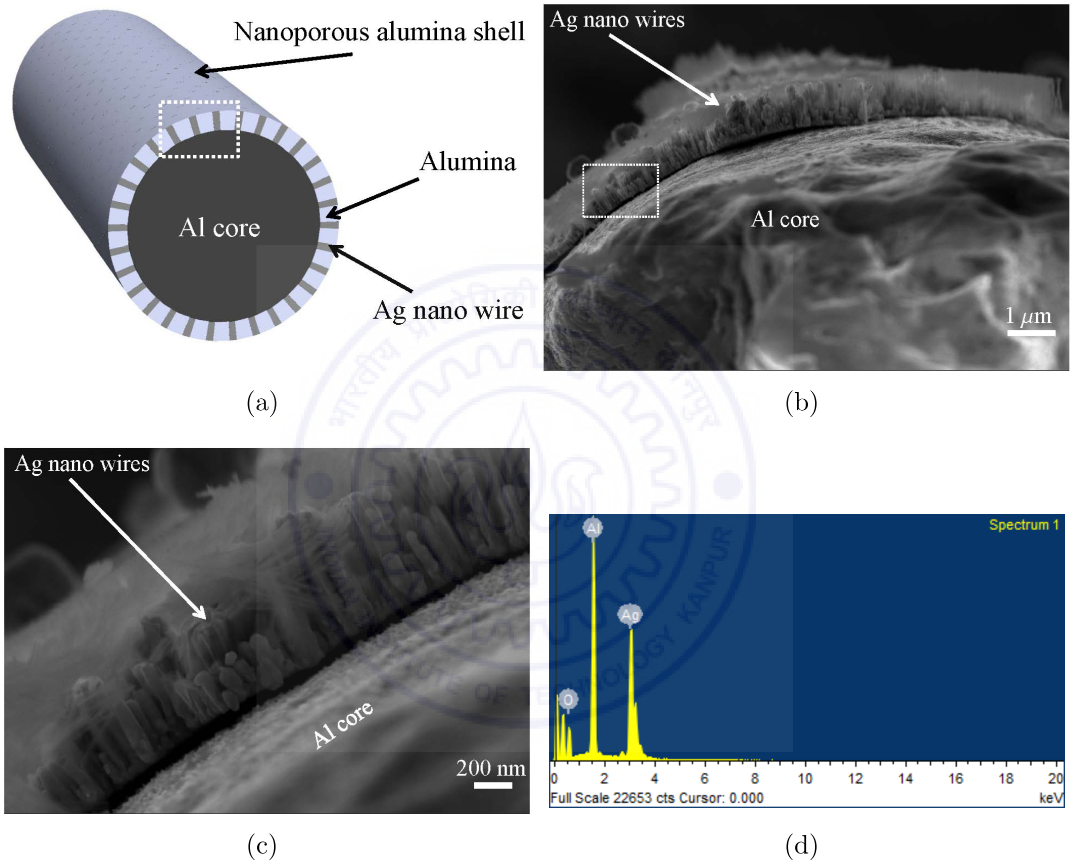

(a) (b)

(c) (d)

Figure 2.14: FESEM image of Ag nanowire deposited in the cylindrical nanoporous alumina. (a) A schematic to electrodeposition of Ag nanowire, (b) electrodeposited Ag nanowires. The white dotted rectangle position of (a) is shown in (b), (c) the zoomed image of area of white dotted rectangle in (b) and the EDX spectra of Ag nanowire embedded in nanoporous alumina shell.

for barrier layer removal and electrodeposition would require further work to optimize the procedures.

2.5 Conclusions

We investigated some new features of the anodization of the aluminium microwires of circular cross section. In planar nanoporous alumina, the nanopores size remain uniform throughout the volume, and the system is homogeneous and anisotropic. In cylindrical nanoporous alumina, in comparison with planar nanoporous alumina, the nanopore sizes decrease towards the axis of the microwire. The azimuthal interpore distance decreases towards the wire axis while the longitudinal interpore distance remains constant. This cylindrical nanoporous alumina system is both inhomogeneous and anisotropic. After removing the aluminum core by etching, the hollow nanoporous alumina microtubes could be obtained. The nanoporous alumina microtubes are optically transparent. The aluminium core could only be removed from a small lengths (2-3 cm) of the anodized wire as the alumina also dissolves while removing the aluminium core from longer lengths of the anodized wire. For longer times of anodization, there were cracks that form in the nanoporous alumina shell because of the volume expansion, and which could be detected by a sudden increase in the anodization current. The time at which the crack occurs for the first time increases with the radius of the microwire, and it is indefinitely long for a plane sheet. For fixed anodization parameters, the shell thickness would be lesser for smaller wire diameters while the nanopores size and the interpore distance remains constant at the outer surface. The nanopore size can be increased nearly to the interpore distance by pore widening process. The barrier layer of the cylindrical nanoporous alumina was removed by the voltage reduction method, and the aluminium core remains at the center. The electrodeposition of the silver nanowires within the pores of the planar nanoporous alumina could be carried out to obtain very thick nanoporous alumina templates, while for sub-hundred micrometer diameter size cylindrical nanoporous alumina, the electrodeposition was not possible for much thicker shells because of the decreasing size of nanopores towards the center and the consequent difficulty in the removal of the insulating barrier alumina layer.

Chapter 3

Homogenized Material Parameters of Cylindrical Nanoporous Alumina

3.1 Introduction

In chapter 2, we have described the fabrication of planar nanoporous alumina and cylindrical nanoporous alumina microtubes. We have also shown that incorporation of metallic nanorods is possible within the pores in the planar as well as cylindrical nanoporous alumina. To understand wave propagation in the nanoporous alumina, we need to model its material parameters by considering it as a homogeneous medium using some valid homogenization method. To homogenize a composite medium, the inclusions should be electrically small, that is, the size of the dispersed particles must be much smaller than the wavelength [7, 79]. The homogenization of planar nanoporous alumina is well known in the literature [51, 80, 81], but the homogenization of cylindrical nanoporous alumina has not been reported.

The Bruggemann homogenization [7,79,82] and Maxwell-Garnett homogenization [7, 79, 83] are widely used two methods for the homogenization of binary mixtures. Since in our case the fill fraction of the inclusion can be made small and the Maxwell-Garnett homogenization works well for fill fraction less than 0.3 [84, 85], therefore, we shall use

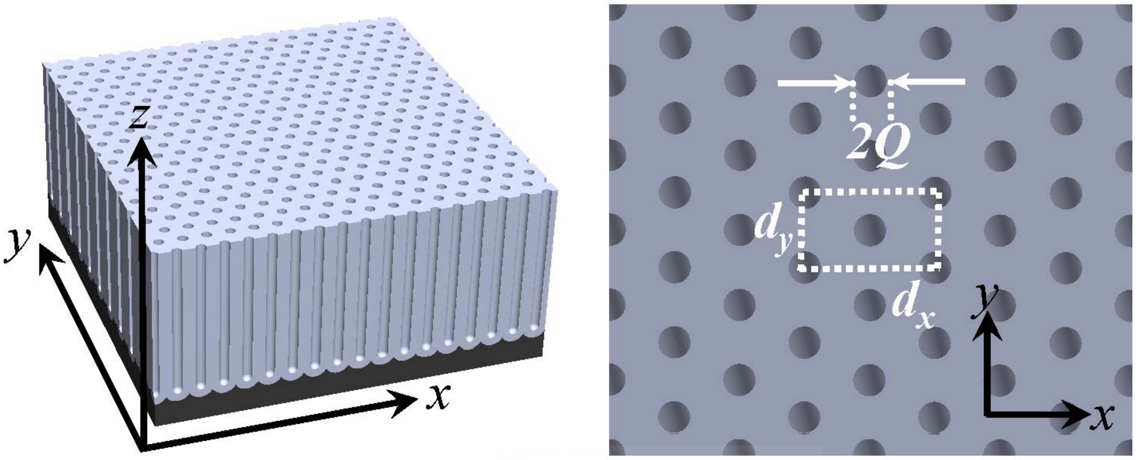

(a) (b)

Figure 3.1: The schematic of (a) planar nanoporous alumina where the nanopores are organized in hexagonal pattern in $xy-$plane and oriented uniformally along $z-$direction, and (b) the top surface area of the planar nanoporous alumina showing a unit shell.

the latter method to homogenize the nanoporous alumina system. In the second section, we homogenize the planar nanoporous alumina.

In the cylindrical nanoporous alumina, the diameter of the nanopores decrease towards the center of the cylinder, hence only a local homogenization will be possible. In the third section we describe the structural parameters of the cylindrical nanoporus alumina required for modeling the effective medium. In the fourth section, we transform the cylindrical geometry into a plane geometry using the technique of transformation optics [16, 86, 87]. We have homogenized the cylindrical nanoporous alumina microtubes in the new transformed geometry and then after homogenization we invert the transformation to obtain the material parameters in the original geometry [88].

3.2 Homogenization of Planar Nanoporous Alumina

Figure 3.1 shows a schematic picture of planar nanoporous alumina. The nanopores have hexagonal arrangement in the xy-plane and are oriented along the z-direction as shown in Fig. 3.1(a). The nanopores are uniformly distributed in the whole volume. Figure 3.1(b) shows the unit cell in the xy-plane. Let the nanopore diameter and interpore distance be $2Q$ and $D(= d_y)$ respectively. Then the nanopore fill fraction f can be given by the following expression

$$\begin{aligned} f &= \frac{\text{Area of nanopores within unit cell}}{\text{Area of unit cell}} && \text{(3.1a)} \\ &= \frac{2 \times (\pi Q^2)}{(\sqrt{3}D) \times D} && \text{(3.1b)} \\ &= \frac{2\pi Q^2}{\sqrt{3}D^2} && \text{(3.1c)} \end{aligned}$$

Here the nanopore fill fraction is same everywhere in the volume. It only depends on the nanopore diameter and the interpore distance. For a fixed interpore distance, the nanopore fill fraction can be changed by increasing the nanopore diameters by pore widening process described in Chapter 1.

For the present, let us assume that the nanopores of planar nanoporous alumina are filled with a material that has a dielectric permittivity of ε_i. Since the nanopores have very high aspect ratio, therefore, the polarizability along the nanowires direction is effectively zero while there is finite polarizability in the transverse direction of the nanopores. The effective permittivity of the planar nanoporous alumina along the nanopores direction, ε_z, can be approximately given by the volume average as [89, 90]

$$\varepsilon_z = f\varepsilon_i + (1 - f)\varepsilon_h \tag{3.2}$$

where ε_i and ε_h are the permittivities of inclusion (air or metal) and host (alumina) respectively.

Since we are considering the areal (area/area) fill fraction, therefore, the effective permittivties ε_x and ε_y along the x-direction and y-direction will be equivalent, that is, $\varepsilon_x = \varepsilon_y$. The effective permittivity along the transverse direction can be obtained by the Maxwell-Garnett homogenization (MGH) theory, and for the cylindrical inclusion it can be given by the following expression [90]

$$\varepsilon_x = \varepsilon_y = \frac{(1+f)\varepsilon_i\varepsilon_h + (1-f)\varepsilon_h^2}{(1-f)\varepsilon_i + (1+f)\varepsilon_h}. \tag{3.3}$$

The Eqs. (3.2) and (3.3) are approximate results and work well for the smaller (< 0.3) fill fractions. They can not, however, be used for larger fill fractions accurately.

3.3 Structural Modeling of Cylindrical Nanoporous Alumina

A cylindrical nanoporous alumina shell whose inner and outer radii are R_1 and R_2 is shown in Fig. 3.2. We divide the cylindrical nanoporous alumina system into three regions. Region-I: inner core from cylindrical axis to R_1 may be metallic or dielectric. Region-II: consisting of the nanoporous alumina shell from R_1 to R_2; Region-III: the outermost region beyond R_2 which may be metal or dielectric. We assume that at the outer surface of the cylindrical nanoporous alumina ($r = R_2$), the nanopores organization is ideally hexagonal packed as shown in Fig. 3.2(a). The interpore distances decrease along the azimuthal direction and there is no change in the interpore distance along the z-direction towards the cylindrical axis. Let the interpore distance be D_2 at R_2 and the nanopore diameter be $2Q_2$ there. Let the interpore distance be d at the ϕz-surface at radius r, and the nanopore diameter be $2q$ at that point. Consider the unit cell as shown in Fig. 3.2(b). The solid angle Ω made by the surface area of the pore at R_2 and r will be same. Therefore, at a point in the nanoporous alumina shell at a distance r from the

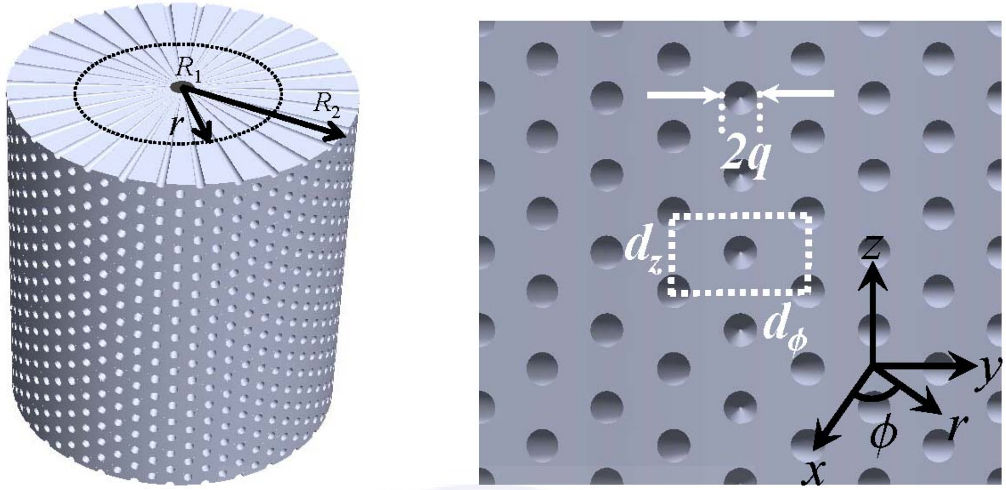

(a) (b)

Figure 3.2: The schematic of (a) position a cylindrical shell of radius r and (b) a small local area on the general ϕz surface at radius r.

center axis,

$$\Omega(r) = \Omega(R_2), \tag{3.4a}$$

$$\frac{\pi q^2}{r^2} = \frac{\pi Q^2}{R_2^2}, \tag{3.4b}$$

$$q = \frac{Q_2}{R_2} r. \tag{3.4c}$$

Equation (3.4c) shows that the pore radius linearly depends on the radial distance from the center of the microwire.

If the pore periodicity at R_2 is D_2, then from the Fig. 3.2(b) the unit cell length along ϕ-direction and along z-direction

$$d_{2,\phi} = \sqrt{3} D_2, \tag{3.5a}$$

$$d_{2,z} = D_2. \tag{3.5b}$$

In the azimuthal plane, the angular width of the unit cell at R_2

$$\Delta\phi = \frac{\sqrt{3} D_2}{R_2}. \tag{3.6}$$

This angular width in the azimuthal plane will be same at any r. Therefore, the unit cell length along ϕ-direction (d_ϕ) and along z-direction (d_z) at a distance r inside the nanoporous alumina shell are given by

$$d_\phi = \Delta\phi \times r, \tag{3.7a}$$

$$= \sqrt{3}\frac{D_2}{R_2}r, \tag{3.7b}$$

$$d_z = D_2. \tag{3.7c}$$

These Eqs. (3.7) show that the pore periodicity along the ϕ-direction linearly depends on r. Therefore, the fill fraction f of the nanopores at a distance R_2 from the center

$$f\left(R_2\right) = \frac{\text{Area of nanopores within unit cell at } R_2}{\text{Area of unit cell at } R_2}, \tag{3.8a}$$

$$= \frac{2 \times \left(\pi Q_2^2\right)}{\left(\sqrt{3}D_2\right) \times D_2}, \tag{3.8b}$$

$$= \frac{2\pi Q_2^2}{\sqrt{3}D_2^2}. \tag{3.8c}$$

Similarly the nanopores fill fraction f at a distance r is

$$f\left(r\right) = \frac{\text{Area of nanopores within unit cell at } r}{\text{Area of unit cell at } r}, \tag{3.9a}$$

$$= \frac{2 \times \left\{\pi\left(\frac{Q_2}{R_2}r\right)^2\right\}}{\left(\sqrt{3}\frac{D_2}{R_2}r\right) \times D_2}, \tag{3.9b}$$

$$= \frac{2\pi Q_2^2}{\sqrt{3}D_2^2}\left(\frac{r}{R_2}\right). \tag{3.9c}$$

Equations (3.9) show the linear dependence of the filling fraction on r, which implies that the cylindrical nanoporous alumina system is an inhomogeneous system. Here the effective medium parameters (dielectric permittivity) will depend on the position. The nanopore fill fraction of cylindrical nanoporous alumina system has been plotted in Fig. 3.3 at nanopore diameter 30 nm and 50 nm at the outer surface.

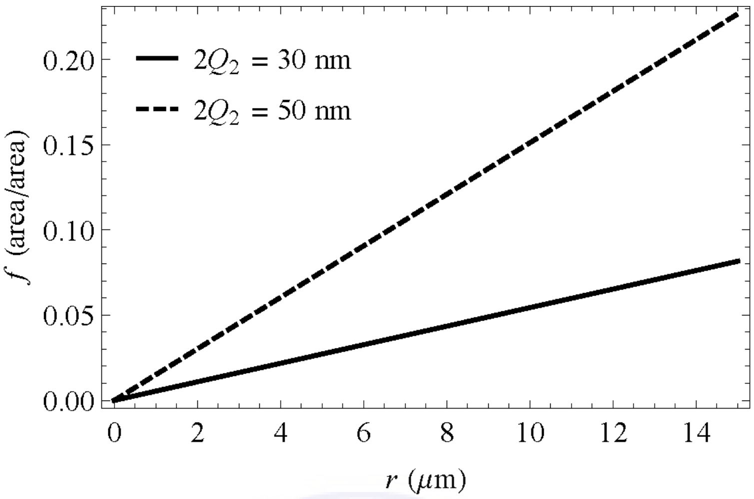

Figure 3.3: Nanopores fill fraction of cylindrical nanoporous alumina when nanopore diameters are 30 nm and 50 nm at the outer surface.

3.4 Geometric Transformation using Transformation Optics

The ad-hoc homogenization of the nanoporous alumina microtube have several assumptions such as the inhomogeneity could be disregarded to locally homogenize the system at different radial distances. In this section, we shall carry out the homogenization rigorously using the techniques of transformation optics [86, 91]. Using a mapping we show that an effective anisotropic dielectric tensor can be obtained for the medium with radially oriented nanowires/nanopores in the curvilinear geometry as well.

The cylindrical shell can be transformed into a rectangular slab by the transformation into cylindrical coordinates,

$$\tilde{x} = \ln r, \quad \tilde{y} = \phi, \quad \tilde{z} = z. \tag{3.10}$$

In the new coordinate frame $(\tilde{x}, \tilde{y}, \tilde{z})$, the transformed material parameters and fields can be written as [91]

$$\tilde{\varepsilon_j} = \varepsilon_j \frac{S_1 S_2 S_3}{S_j^2}, \quad \tilde{\mu_j} = \mu_j \frac{S_1 S_2 S_3}{S_j^2}, \quad \tilde{E}_j = S_j E_j, \quad \tilde{H}_j = S_j H_j, \tag{3.11}$$

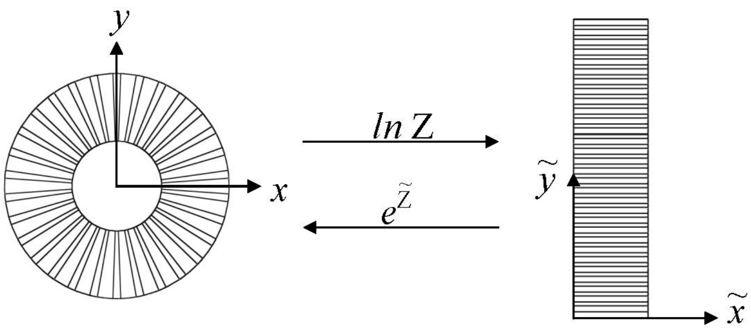

Figure 3.4: A cylindrical shell is mapped to a flat slab. The nanopores along the radial direction in shell mapped along the $\tilde{x}$-direction in the new frame.

$$S_j^2 = \left(\frac{\partial r}{\partial \tilde{q}_j}\right)^2 + \left(\frac{r\partial \phi}{\partial \tilde{q}_j}\right)^2 + \left(\frac{\partial z}{\partial \tilde{q}_j}\right)^2, \tag{3.12}$$

where tilde ($\tilde{}$) represents the new transformed frame. Now using Eqs. (3.10)–(3.12), the material parameters in the new frame for the embedded material (i) and alumina host material (h) within their respective regions are given by

$$\tilde{\varepsilon}_{\tilde{x},i} = \varepsilon_{r,i}, \quad \tilde{\varepsilon}_{\tilde{y},i} = \varepsilon_{\phi,i}, \quad \tilde{\varepsilon}_{\tilde{z},i} = e^{2\tilde{x}}\varepsilon_{z,i}, \tag{3.13a}$$

$$\tilde{\mu}_{\tilde{x},i} = \mu_{r,i}, \quad \tilde{\mu}_{\tilde{y},i} = \mu_{\phi,i}, \quad \tilde{\mu}_{\tilde{z},i} = e^{2\tilde{x}}\mu_{z,i}, \tag{3.13b}$$

$$\tilde{\varepsilon}_{\tilde{x},h} = \varepsilon_{r,h}, \quad \tilde{\varepsilon}_{\tilde{y},h} = \varepsilon_{\phi,h}, \quad \tilde{\varepsilon}_{\tilde{z},h} = e^{2\tilde{x}}\varepsilon_{z,h}, \tag{3.13c}$$

$$\tilde{\mu}_{\tilde{x},h} = \mu_{r,h}, \quad \tilde{\mu}_{\tilde{y},h} = \mu_{\phi,h}, \quad \tilde{\mu}_{\tilde{z},h} = e^{2\tilde{x}}\mu_{z,h}. \tag{3.13d}$$

In this manner, we can transform the cylindrical shell with radially emanating nanopores/nanorods into a slab with columns along the $\tilde{x}$ direction (see Fig. 3.4). The only difference from a medium of unidirectional nano-columns is that both the background material of the slab and the columns are now both anisotropic and inhomogenous (along $\tilde{z}$) in the new geometry. Such a structure can be easily homogenized by noting that the principal axis of anisotropy coincides with the column axes and the fact that we have only diagonal anisotropy.

3.5 Homozenization of Cylindrical Nanoporous Alumina

Now we will proceed to homogenize the structure in the new geometry, and then transform the obtained effective-medium parameters back to the cylindrical geometry. This will be valid at all points, except at the origin in the cylindrical geometry where there is a singularity, which is excluded in the homogenization. The effective permittivity along the $\tilde{x}$-direction with the help of Eq. (3.13) can be given by the volume average [89, 90]

$$\varepsilon_{\tilde{x}}^{\text{eff}} = f\varepsilon_{r,i} + (1-f)\varepsilon_{r,h}, \tag{3.14}$$

where f is the fill fraction of the inclusion. In the transverse direction, the effective permittivity can be approximately obtained by the Maxwell-Garnett homogenization procedure. We would need the polarizabilities of anisotropic cylinders embedded in an anisotropic medium. The polarisability of an anisotropic prolate spheroid in an isotropic medium is well known [92] and the homogenization of anisotropic ellipsoids embedded in an anisotropic medium has been also been obtained [93].

The coincidence of the principal axes of anisotropy with the symmetry axes of the geometry makes it simple here. In our case, as the inclusion is cylindrical with very large aspect ratio, therefore, it can be approximated as a prolate spheroid with extreme eccentricity (like a long needle). The normalized electric field of an anisotropic cylinder with $\bar{\bar{\varepsilon}} = (1, 1, r_0^2)$ embedded in an anisotropic medium $\bar{\bar{\varepsilon}} = (\varepsilon_{Al_2O_3}, \varepsilon_{Al_2O_3}, \varepsilon_{Al_2O_3} r_0^2)$ which is placed in a uniform electric field have been plotted using COMSOL Multiphysics is shown in Fig. 3.5(a). Here $\varepsilon_{Al_2O_3}$ $(= 2.6375)$ is the dielectric permittivity of the isotropic alumina and r_0 $(= 12.5\mu\text{m})$ is the outer radius of cylindrical shell. The field plot of an anisotropic nanowire with $\bar{\bar{\varepsilon}} = (\varepsilon_{Ag}, \varepsilon_{Ag}, \varepsilon_{Ag} r_0^2)$ embedded in an anisotropic medium $\bar{\bar{\varepsilon}} = (\varepsilon_{Al_2O_3}, \varepsilon_{Al_2O_3}, \varepsilon_{Al_2O_3} r_0^2)$ is shown in Fig. 3.5(b), where ε_{Ag} $(= -1359.1400 + i115.5060)$ represents the dielectric permittivity of silver metal. For comparison the field plots of an isotropic air cylinder with $\varepsilon = 1$ and an isotropic silver cylinder with $\varepsilon_{Ag} = -1359.1400 +$

$i115.5060$ placed in isotropic alumina $\varepsilon_{Al_2O_3} = 2.6375$ are shown in Fig. 3.5(c) and 3.5(d) respectively. Since the diameter of anisotropic cylinder with $\bar{\bar{\varepsilon}} = (1, 1, r_0^2)$ and anisotropic nanowire with $\bar{\bar{\varepsilon}} = (\varepsilon_{Ag}, \varepsilon_{Ag}, \varepsilon_{Ag} r_0^2)$ both are electrically small, therefor, the field plots are almost look like the case of isotropic air cylinder and isotropic silver nanowire. We see that the field plots for anisotropic cylinders are almost the same as the field plots of the isotropic cylinders as well as the polarizability. So the local homogenization is good approximation for such type of system. The homogenized effective-medium parameters are obtained as [90]

$$\varepsilon_{\tilde{y}}^{\text{eff}} = \frac{(1+f)\varepsilon_{\phi,i}\varepsilon_{\phi,h} + (1-f)\varepsilon_{\phi,h}^2}{(1-f)\varepsilon_{\phi,i} + (1+f)\varepsilon_{\phi,h}}, \tag{3.15}$$

and

$$\varepsilon_{\tilde{z}}^{\text{eff}} = e^{2\tilde{x}} \frac{(1+f)\varepsilon_{z,i}\varepsilon_{z,h} + (1-f)\varepsilon_{z,h}^2}{(1-f)\varepsilon_{z,i} + (1+f)\varepsilon_{z,h}}. \tag{3.16}$$

The additional exponential factor in the $\varepsilon_{\tilde{z}}^{\text{eff}}$ results in a biaxial and inhomogeneous medium in the Cartesian coordinate frame of rectangular slab. Thus, it is different from a flat nanoporous anodic alumina template.

Now we will map back these parameters into the original cylindrical geometry and obtain

$$\varepsilon_r^{\text{eff}} = f\varepsilon_{r,i} + (1-f)\varepsilon_{r,h}, \tag{3.17}$$

$$\varepsilon_{\phi}^{\text{eff}} = \frac{(1+f)\varepsilon_{\phi,i}\varepsilon_{\phi,h} + (1-f)\varepsilon_{\phi,h}^2}{(1-f)\varepsilon_{\phi,i} + (1+f)\varepsilon_{\phi,h}}, \tag{3.18}$$

and

$$\varepsilon_z^{\text{eff}} = \frac{(1+f)\varepsilon_{z,i}\varepsilon_{z,h} + (1-f)\varepsilon_{z,h}^2}{(1-f)\varepsilon_{z,i} + (1+f)\varepsilon_{z,h}}. \tag{3.19}$$

Note that the exponential factors of $e^{2\tilde{x}}$ cancel in the inverse mapping process. Since in the cylindrical geometry, the individual materials are isotropic, the effective permittivity components $\varepsilon_{\phi}^{\text{eff}}$ and $\varepsilon_z^{\text{eff}}$ are equal in this approximation. Incidentally, we obtain an identical result as obtained by just applying this process directly in the curvilinear

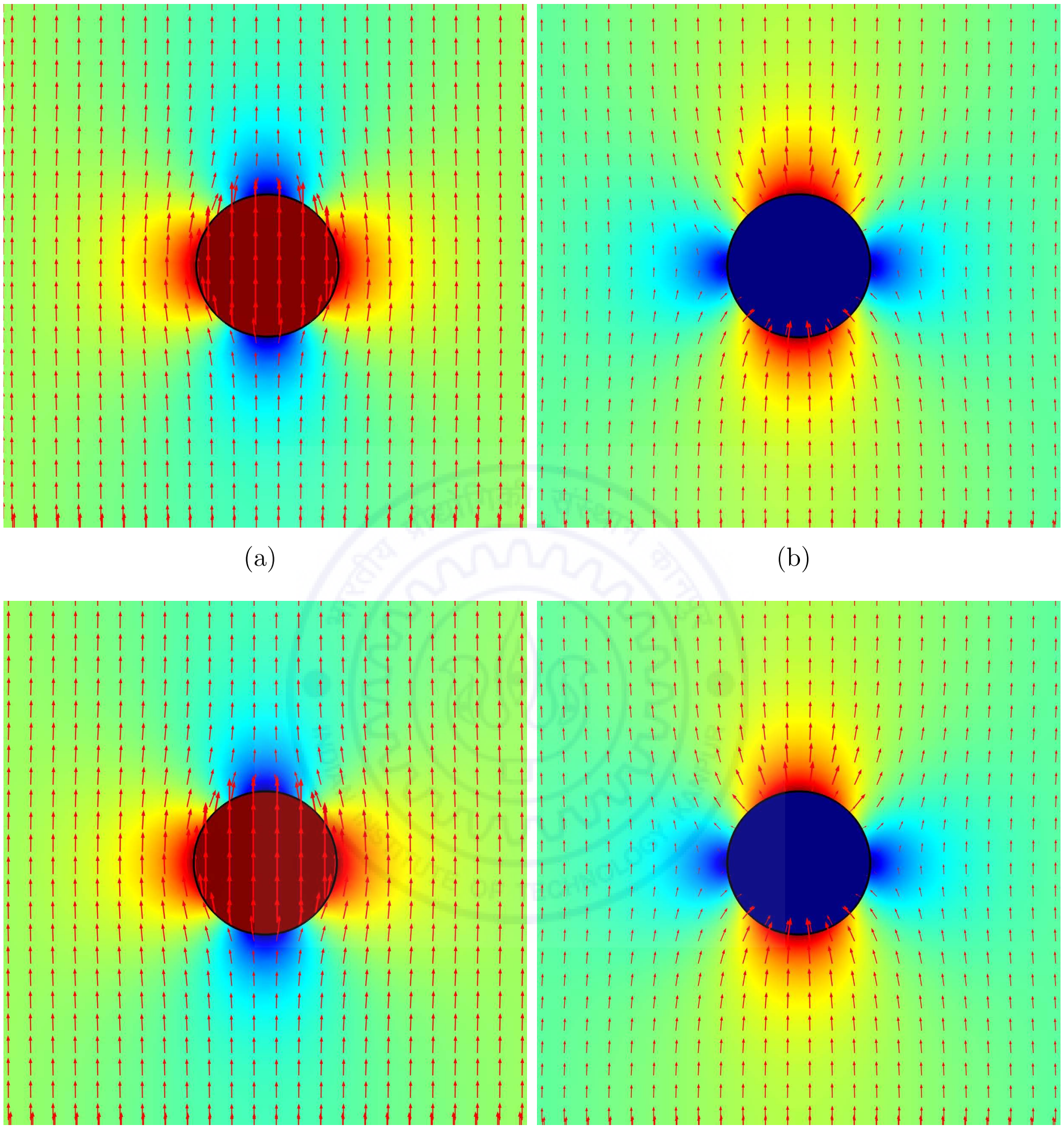

(a) (b)

(c) (d)

Figure 3.5: The COMSOL calculated, the normalized electric field of (a) anisotropic cylinder with $\bar{\bar{\varepsilon}} = (1, 1, r_0^2)$ in an anisotropic medium $\bar{\bar{\varepsilon}} = (\varepsilon_{Al_2O_3}, \varepsilon_{Al_2O_3}, \varepsilon_{Al_2O_3} r_0^2)$, (b) anisotropic cylinder with $\bar{\bar{\varepsilon}} = (\varepsilon_{Ag}, \varepsilon_{Ag}, \varepsilon_{Ag} r_0^2)$ in an anisotropic medium $\bar{\bar{\varepsilon}} = (\varepsilon_{Al_2O_3}, \varepsilon_{Al_2O_3}, \varepsilon_{Al_2O_3} r_0^2)$, (c) isotropic air cylinder with $\varepsilon = 1$ in an isotropic alumina $\varepsilon = \varepsilon_{Al_2O_3}$ and (d) isotropic silver cylinder with $\varepsilon = \varepsilon_{Ag}$ in an isotropic alumina $\varepsilon = \varepsilon_{Al_2O_3}$. The color shows the normalized electric field and the arrow show the electric field directions. Here $\varepsilon_{Al_2O_3} = 2.6375$, $\varepsilon_{Ag} = -1359.1400 + i115.5060$ and $r_0 = 12.5\mu$m.

geometry. This is the due to the large aspect ratio of the inclusions and the electrically small diameter of the nanopores aligned along the r-direction. We also note that cylindrically symmetric metamaterials have been also been homogenized using similar geometric transformations [94, 95], including for the design of anisotropic invisibility cloaks [96].

In this picture, only the areal fill fraction (f) of the pore/nanorod determines the effective medium properties and the anisotropy results in $\varepsilon_r \neq \varepsilon_\phi$ and $\varepsilon_z \simeq \varepsilon_\phi$. From the FESEM images of several samples, we find that the nanopore cross-section approximately reduces linearly with the radial distance in alumina microtubes anodized at constant voltage, and the areal fill fraction changes with the radial distance as Eq. 3.9. Typically, $D_2 = 100$ nm at the outer surface of the anodized aluminium wire where anodization begins when an anodization voltage of 40 V is used at 0° C in oxalic acid (see Chapter 2). Similarly, the pore diameter $2Q_2$ is 30 nm under these circumstances. The pore diameter can be flexibly increased to any any value up to about 90 nm by pore widening in a solvent such as phosphoric acid. At a wavelength of 632.8 nm, Fig. 3.6 shows the variation in the anisotropic material parameters with the radial distance obtained for the cases of (i) air nanopores in nanoporous alumina and (ii) silver nanorods in the nanoporous alumina, where a Drude dielectric permittivity for silver (Fig. 3.7(b)) was used as $\varepsilon_{Ag} = \varepsilon_\infty - \omega_p^2/[\omega(\omega + i\gamma)]$ with $\varepsilon_\infty = 5.7$, $\omega_p = 9.2$eV and $\gamma = 0.021$eV [8]. For the host alumina material (Fig. 3.7(a)), the dielectric permittivity have been taken from [1]. The imaginary part of the effective medium parameters for the silver filled nanoporous structure is also small due to the small fill fractions (0.23) of silver. Due to the radial variation of the pore diameters, these fibers are actually spatially inhomogenous. Typically, nanowires made of plasmonic materials that have $\mathrm{Re}(\varepsilon) < 0$ results in an extreme effective anisotropy with $\varepsilon_r < 0$ and $\varepsilon_\phi > 0$.

At a constant nanopore fill fraction of 0.23, the effective permittivity components with respect to the frequency have been plotted in Fig. 3.8. Here also the alumina data is taken from Ref. [1] and the silver data is from Ref. [8]. For the case of air inclusions as shown in Fig. 3.8(a), the permittivity components are anisotropic. The anisotropy is

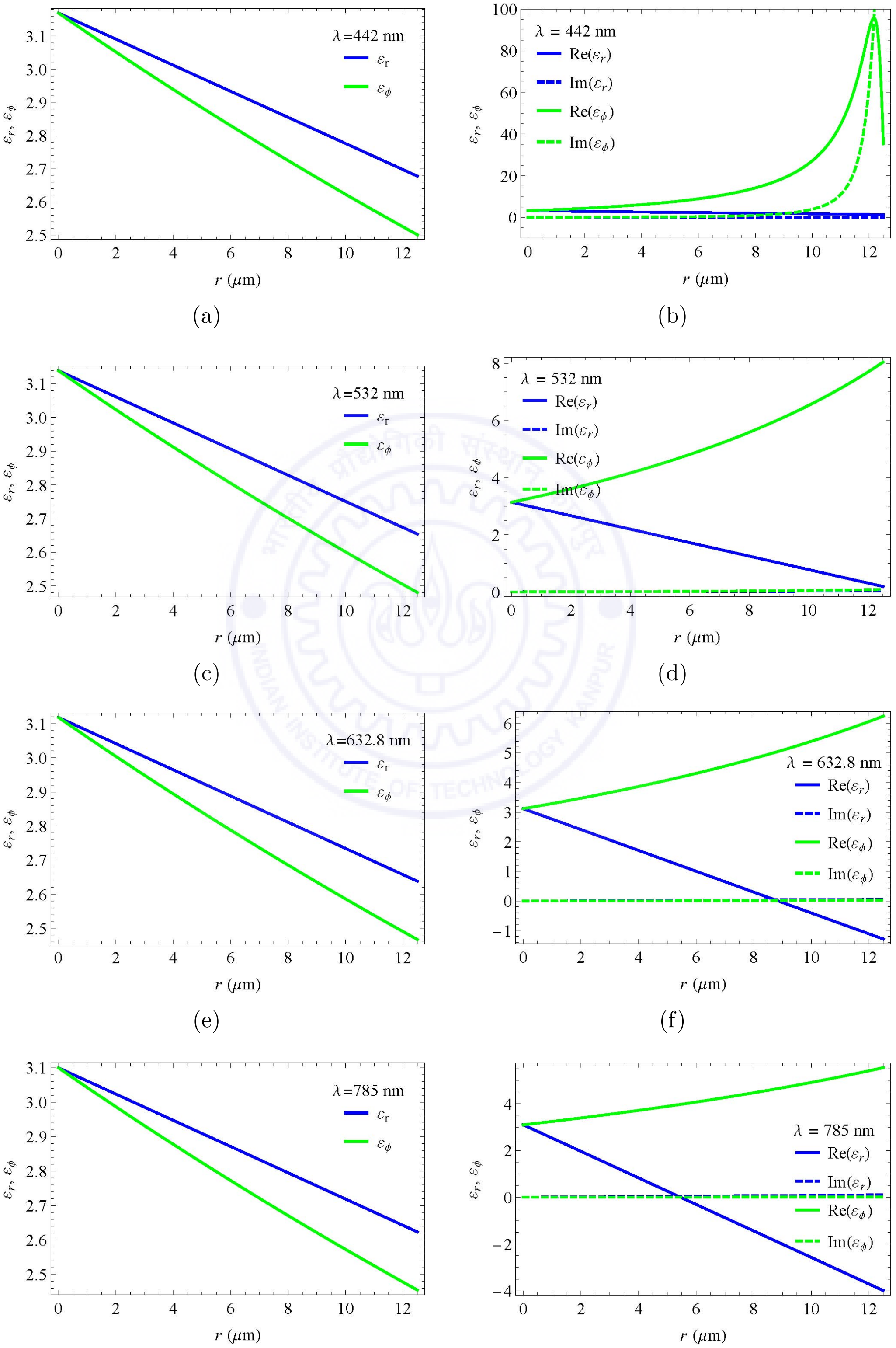

(a) (b)

(c) (d)

(e) (f)

(g) (h)

Figure 3.6: The effective permittivity components of cylindrical nanoporous alumina with respect to the radius of the wire at 442 nm, 532 nm, 632.8 nm and 785 nm wavelengths. The left panel is for air inclusion and the right panel is for the silver inclusion.

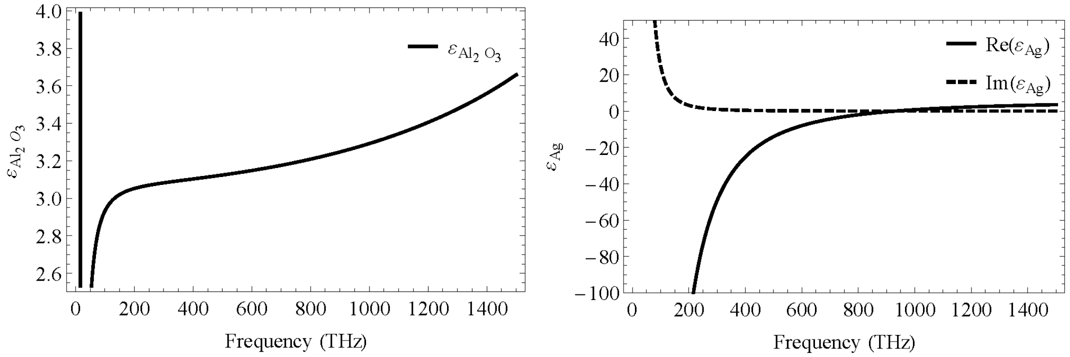

(a) (b)

Figure 3.7: The permittivity of (a) pure alumina (Weber, Handbook of Optical Materials, 2003) and (b) silver metal of Drude model (Cai et al., Optical Metamaterials: Fundamentals and Applications, 2010).

larger for higher frequencies. The material dispersion for the case of silver inclusions is shown in Fig. 3.8(b). The signs of ε_r and ε_ϕ vary over the given spectral range. We see that in certain spectral range the permittivity components show the hyperbolic dispersion. In the case of air inclusion, the ε_r is always greater than the ε_ϕ is shown in Fig. 3.8(a). If we fill the nanopores of cylindrical nanoporous alumina with some higher index medium compare to alumina then this inequality can be reversed, that is, in this case $\varepsilon_r < \varepsilon_\phi$. But if we fill the nanopores of the cylindrical nanoporous alumina with metals then all the inequality exist. Figure 3.8(b) shows the effective permittivity components of cylindrical nanoporous alumina with silver metal inclusion. It shows that below the 600 THz there is indefinite permittivity with $\varepsilon_r < 0, \varepsilon_\phi > 0$ which have very high metallic losses. In a very narrow rage around 800 THz there is $\varepsilon_r > 0, \varepsilon_\phi < 0$. But beyond this range there is normal anisotropy. It is clear that the metal inclusion increases the anisotropy of the nanoporous alumina.

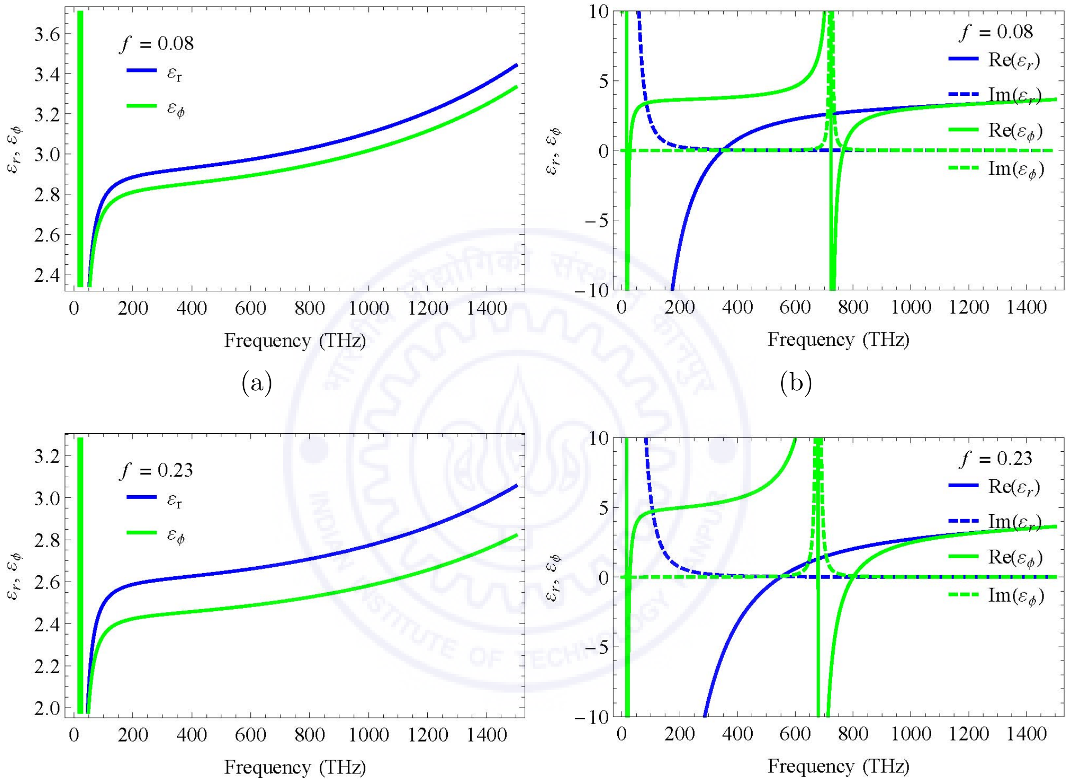

(a) (b)

(c) (d)

Figure 3.8: The effective permittivity components of cylindrical nanoporous alumina at constant nanopore fill fractions of 0.08 and 0.23 with respect to the frequency. The left panel for air inclusion, and the right panel for silver inclusion. Here R_1=0.5μm and R_2=12.5μm.

3.6 Conclusions

We have carried out a homogenization analysis using the structural parameters of the cylindrical nanoporous alumina microtubes. The nanopore diameter of nanopores, azimuthal interpore distance and the nanopore fill fraction vary linearly with the radius of the wire. All these three decrease toward the microwire axis, and the cylindrical nanoporous alumina is an inhomogeneous and anisotropic medium. These variations are not available in the planar nanoporous alumina which is only an anisotropic but a homogeneous system. We locally homogenized the cylindrical nanoporous alumina using the technique of the transformation optics and the Maxwell-Garnett homogenization theory. We found that for the case of air inclusions the system has inhomogeneous and anisotropic dispersion while for the silver inclusion the system has anisotropic as well as hyperbolic dispersion depending on the electromagnetic spectral ranges. For fixed inclusions, these dispersions can be changed by changing the nanopore diameters or changing the interpore distance. For fixed nanopore diameters and interpore distance the dispersions can be changed by using the different inclusions. This method is only valid for dilute inclusions ($f < 0.3$). For higher fill fraction ($f > 0.3$), these homogenization would not be valid and in that case we have to use some other homogenization method such as Bruggemann's homogenization method. In the case of air inclusions there are less losses almost over whole given range but there are huge losses for metallic inclusions in lower frequency ranges.

Chapter 4

Homogeneous, Anisotropic Metamaterial Optical Fiber

4.1 Introduction

Circular waveguides optical fibers have been studied since several decades [97]. They are being used in many scientific and engineering applications such as communication, power transmission, sensors, medical, instruments etc. Most of them are isotropic in nature and light confinement is due to the total internal reflections. Later on photonic crystal fibers, which are internally structured but invariant along the axial direction, have been introduced [29]. In these fibers, few micrometer size holes placed in a perodic manner are drawn along the fiber axis and light is guided by the photonic band gap in the transverse direction [30]. Development of metamaterials has opened new doors for applications of optical fibers [7]. Using metamaterials, any desired anisotropy can be introduced in the waveguides and optical fibers [31, 53, 98]. The modal dispersions of an anisotropic dielectric permittivity fiber have been recently discovered [36]. The light guiding nature of metamaterial clad hollow waveguides also has been of interest, where the anisotropy in the clad region is produced by the split ring resonators [39, 40].

In the Chapter 2 we have discussed about the fabrication of radially structured microtubes of nanoporous alumina, whose effective parameters have been theoretically found in Chapter 3 using the Maxwell-Garnett homogenization theory. In this chapter we shall discuss about the wave guiding nature of these radially structured fibers. These fibers have an anisotropy with cylindrical symmetry that renders the polarization in the axial, radial and azimuthal directions different. To simplify the discussion, we shall consider that the anisotropic medium is homogeneous in this chapter. This assumption will be relaxed in the next chapter. We find these waveguides to support novel modes, particularly where the anisotropy is indefinite and the mode dispersions become hyperbolic. The new modes possible are analyzed and explained in this chapter. Conditions for the guidance are also analyzed.

4.2 Electromagnetic Fields in a Cylindrically Symmetric Anisotropic Medium

Consider a cylindrically symmetric medium with anisotropy along the radial, azimuthal and axial directions as given by the homogenization in Chapter 3 for a nanoporous alumina microtube. More generally, both the dielectric permittivity ($\bar{\bar{\varepsilon}}$) and magnetic permeability ($\bar{\bar{\mu}}$) can be anisotropic and are second ranked tensors that can be represented by 3×3 matrices. For cylindrically symmetric anisotropic medium for diagonal anisotropy, $\bar{\bar{\varepsilon}}$ and $\bar{\bar{\mu}}$ are given as

$$\bar{\bar{\varepsilon}} = \begin{pmatrix} \varepsilon_r & 0 & 0 \\ 0 & \varepsilon_\phi & 0 \\ 0 & 0 & \varepsilon_z \end{pmatrix}, \tag{4.1a}$$

$$\bar{\bar{\mu}} = \begin{pmatrix} \mu_r & 0 & 0 \\ 0 & \mu_\phi & 0 \\ 0 & 0 & \mu_z \end{pmatrix}. \tag{4.1b}$$

The medium for the present discussion (in this chapter) will be regarded as homogeneous. The Maxwell's equations for time harmonic electromagnetic fields in a source free, linear, anisotropic and homogeneous medium can be written as

$$\vec{\nabla}\cdot\left(\varepsilon_0\bar{\bar{\varepsilon}}\vec{E}\right)=0, \tag{4.2a}$$

$$\vec{\nabla}\cdot\left(\mu_0\bar{\bar{\mu}}\vec{H}\right)=0, \tag{4.2b}$$

$$\vec{\nabla}\times\vec{E}=i\omega\mu_0\bar{\bar{\mu}}\vec{H}, \tag{4.2c}$$

$$\vec{\nabla}\times\vec{H}=-i\omega\varepsilon_0\bar{\bar{\varepsilon}}\vec{E}. \tag{4.2d}$$

We are interested in guided mode solutions in the waveguide that propagate along the waveguide axis (z-direction). Hence, we consider the form of electromagnetic wave propagating in the fiber as

$$\vec{E}\left(r,\phi,z,t\right)=\vec{E}\left(r,\phi\right)e^{i(\beta z-\omega t)}, \tag{4.3a}$$

$$\vec{H}\left(r,\phi,z,t\right)=\vec{H}\left(r,\phi\right)e^{i(\beta z-\omega t)}, \tag{4.3b}$$

where β is the propagation constant along z-direction. Expanding the Eq. (4.2c) and Eq. (4.2d) using Eqs. (4.1) we get

$$\begin{aligned}\left(\frac{1}{r}\frac{\partial E_z}{\partial\phi}-\frac{\partial E_\phi}{\partial z}\right)\hat{r}+\left(\frac{\partial E_r}{\partial z}-\frac{\partial E_z}{\partial r}\right)\hat{\phi}+\frac{1}{r}\left\{\frac{\partial}{\partial r}\left(rE_\phi\right)-\frac{\partial E_r}{\partial\phi}\right\}\hat{z}&\\ =i\omega\mu_0\left\{\mu_rH_r\hat{r}+\mu_\phi H_\phi\hat{\phi}+\mu_zH_z\hat{z}\right\},&\end{aligned} \tag{4.4a}$$

$$\begin{aligned}\left(\frac{1}{r}\frac{\partial H_z}{\partial\phi}-\frac{\partial H_\phi}{\partial z}\right)\hat{r}+\left(\frac{\partial H_r}{\partial z}-\frac{\partial H_z}{\partial r}\right)\hat{\phi}+\frac{1}{r}\left\{\frac{\partial}{\partial r}\left(rH_\phi\right)-\frac{\partial H_r}{\partial\phi}\right\}\hat{z}&\\ =-i\omega\varepsilon_0\left\{\varepsilon_rE_r\hat{r}+\varepsilon_\phi E_\phi\hat{\phi}+\varepsilon_zE_z\hat{z}\right\}.&\end{aligned} \tag{4.4b}$$

Using Eq. (4.3) in Eq. (4.4), and comparing the coefficients of $\hat{r}$, $\hat{\phi}$ and $\hat{z}$ on both sides, we get

$$\frac{1}{r}\frac{\partial E_z}{\partial \phi} - i\beta E_\phi = i\omega\mu_0\mu_r H_r, \tag{4.5a}$$

$$i\beta E_r - \frac{\partial E_z}{\partial r} = i\omega\mu_0\mu_\phi H_\phi, \tag{4.5b}$$

$$\frac{1}{r}\left\{\frac{\partial}{\partial r}(rE_\phi) - \frac{\partial E_r}{\partial \phi}\right\} = i\omega\mu_0\mu_z H_z, \tag{4.5c}$$

$$\frac{1}{r}\frac{\partial H_z}{\partial \phi} - i\beta H_\phi = -i\omega\varepsilon_0\varepsilon_r E_r, \tag{4.5d}$$

$$i\beta H_r - \frac{\partial H_z}{\partial r} = -i\omega\varepsilon_0\varepsilon_\phi E_\phi, \tag{4.5e}$$

$$\frac{1}{r}\left\{\frac{\partial}{\partial r}(rH_\phi) - \frac{\partial H_r}{\partial \phi}\right\} = -i\omega\varepsilon_0\varepsilon_z E_z. \tag{4.5f}$$

Eliminating H_ϕ from Eq. (4.5b) and Eq. (4.5d), H_r from Eq. (4.5a) and Eq. (4.5e), E_ϕ from Eq. (4.5a) and Eq. (4.5e) and E_r from Eq. (4.5b) and Eq. (4.5d) we obtain

$$E_r = \left\{\frac{i\omega\mu_0\mu_\phi}{\omega^2\varepsilon_0\mu_0\varepsilon_r\mu_\phi - \beta^2}\right\}\left(\frac{\beta}{\omega\mu_0\mu_\phi}\frac{\partial E_z}{\partial r} + \frac{1}{r}\frac{\partial H_z}{\partial \phi}\right), \tag{4.6a}$$

$$E_\phi = \left\{\frac{i\omega\mu_0\mu_r}{\omega^2\varepsilon_0\mu_0\varepsilon_\phi\mu_r - \beta^2}\right\}\left(-\frac{\partial H_z}{\partial r} + \frac{\beta}{\omega\mu_0\mu_r}\frac{1}{r}\frac{\partial E_z}{\partial \phi}\right), \tag{4.6b}$$

$$H_r = \left\{\frac{i\beta}{\omega^2\varepsilon_0\mu_0\varepsilon_\phi\mu_r - \beta^2}\right\}\left(\frac{\partial H_z}{\partial r} - \frac{\omega\varepsilon_0\varepsilon_\phi}{\beta}\frac{1}{r}\frac{\partial E_z}{\partial \phi}\right), \tag{4.6c}$$

$$H_\phi = \left\{\frac{i\beta}{\omega^2\varepsilon_0\mu_0\varepsilon_r\mu_\phi - \beta^2}\right\}\left(\frac{\omega\varepsilon_0\varepsilon_r}{\beta}\frac{\partial E_z}{\partial r} + \frac{1}{r}\frac{\partial H_z}{\partial \phi}\right). \tag{4.6d}$$

We see that in Eqs. (4.6) E_r, E_ϕ, H_r and H_ϕ are all functions of E_z and H_z. For the TE mode, $E_z = 0$ and the components E_r, E_ϕ, H_r and H_ϕ will be non-zero. For the TM mode, $H_z = 0$ and the four components E_r, E_ϕ, H_r and H_ϕ will be non-zero. Only either TE, TM, or hybrid EH and HE modes are considered here.

In an ordinary isotropic fiber or waveguide there are oscillatory and decaying solutions described by Bessel functions with integral order. But the anisotropic nature of the material of the waveguides causes the other kind of solutions. To explore all the possible solutions in a cylindrical anisotropic waveguide, we shall first discuss the modes in an anisotropic coaxial waveguide, where the region inside and outside are metallic. These metal boundaries can be approximated as perfect electric conductors (PEC) for most practical purposes. The PEC condition will have lesser errors for lower frequencies than the higher frequencies because at lower frequencies its metallic nature will be better than higher frequencies. At higher frequencies, beyond optical (e.g. UV), metals behaves as dielectric. But metals like silver or aluminium has a large plasma frequency (9.2 eV and 15.1 eV) which would make the magnitude of the dielectric permittivity very large even at 632.8 nm wavelength. Then the metal would actually appear as a resistive electrical conductor. If we do not consider the PEC conditions then the solutions particular to the cylindrical anisotropic medium can not be clearly distinguished because of the dielectric boundary constraints which will couple the polarization and will not allow the propagation of pure TE and TM modes. If we consider a coaxial waveguide with PEC boundary inside and outside, then the modal dispersion relations can be decoupled for E_z and H_z which will give TM and TE modes respectively. In the next section we will study the behavior of TE and TM modes in a nanoporus alumina metamaterial waveguide in the coaxial geometry. A schematic picture of such a waveguide is shown in Fig. 4.1. Now we first carry out the general mode analysis of a PEC-anisotropic-PEC coaxial fiber, and later present the numerical analysis of the PEC-nanoporous alumina-PEC coaxial fiber.

4.2.1 TE Modes in a Coaxial Anisotropic Fiber

We shall first consider the TE modes with

$$E_r \neq 0, E_\phi \neq 0, E_z = 0, \tag{4.7a}$$

$$H_r \neq 0, H_\phi \neq 0, H_z \neq 0. \tag{4.7b}$$

Using Eq. (4.7) in Eqs. (4.6a) and (4.6b) and solving the Eq. (4.5c) for H_z, we get

$$\frac{\partial^2 H_z}{\partial r^2} + \frac{1}{r}\frac{\partial H_z}{\partial r} + \frac{\mu_\phi}{\mu_r}\left\{\frac{k_0^2\varepsilon_\phi\mu_r - \beta^2}{k_0^2\varepsilon_r\mu_\phi - \beta^2}\right\}\frac{1}{r^2}\frac{\partial^2 H_z}{\partial \phi^2} + \frac{\mu_z}{\mu_r}\left\{k_0^2\varepsilon_\phi\mu_r - \beta^2\right\}H_z = 0. \tag{4.8}$$

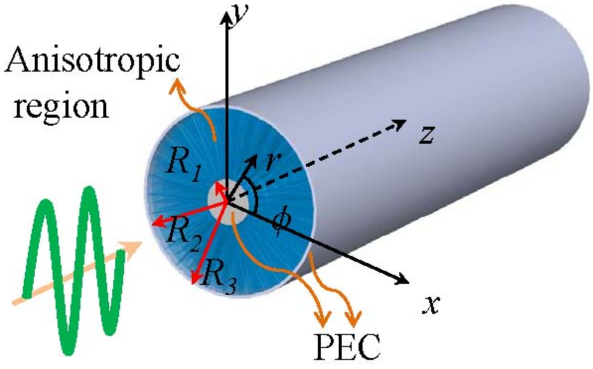

Figure 4.1: Schematic of the coaxial fiber. The region between R_1 and R_2 is the anisotropic cylindrical nanoporous alumina shell. The core ($r < R_1$) and the outer region ($r > R_2$) of the anisotropic region are the PEC.

We use separation of variables to solve the above partial differential Eq. (4.8). Let

$$H_z(r,\theta) = R(r)\,\Theta(\theta)\,, \tag{4.9}$$

so that azimuthal part of the Eq. (4.8) is governed by

$$\frac{1}{\Phi(\phi)}\frac{d^2\Phi(\phi)}{d\phi^2} = -m^2, \tag{4.10}$$

where m is a constant and the radial part of the Eq. (4.8) satisfies

$$r^2\frac{d^2R(r)}{dr^2} + r\frac{dR(r)}{dr} + \left[\frac{\mu_z}{\mu_r}\left\{k_0^2\varepsilon_\phi\mu_r - \beta^2\right\}r^2 - \frac{\mu_\phi}{\mu_r}\left\{\frac{k_0^2\varepsilon_\phi\mu_r - \beta^2}{k_0^2\varepsilon_r\mu_\phi - \beta^2}\right\}m^2\right]R(r) = 0. \tag{4.11}$$

The solution of Eq. (4.10) is

$$\Phi(\phi) = Ce^{im\phi} \tag{4.12}$$

where C is a constant and m is constrained to be an integer due to the single valued requirement on $\Phi(\phi)$. Defining

$$k_\nu^2 = \frac{\mu_z}{\mu_r}\left\{k_0^2\varepsilon_\phi\mu_r - \beta^2\right\}, \tag{4.13a}$$

$$\nu^2 = \frac{\mu_\phi}{\mu_r}\left\{\frac{k_0^2\varepsilon_\phi\mu_r - \beta^2}{k_0^2\varepsilon_r\mu_\phi - \beta^2}\right\}m^2, \tag{4.13b}$$

then the Eq. (4.11) can be written as

$$r^2 \frac{d^2 R(r)}{dr^2} + r \frac{dR(r)}{dr} + \left(k_\nu^2 r^2 - \nu^2\right) R(r) = 0, \tag{4.14}$$

which is the well known Bessel differential equation. Solving this equation we obtain the radial dependence. A general form for the z component for the magnetic field is

$$H_z(r, \phi, z, t) = \{A_1 J_\nu(k_\nu r) + A_2 Y_\nu(k_\nu r)\} e^{im\phi} e^{i(\beta z - \omega t)}. \tag{4.15}$$

where J_ν and Y_ν are the Bessel functions of first kind and second kind (Y_ν are also termed Neumann functions). The coefficients A_1 and A_2 can be found by setting the tangential components $E_\phi = 0$ at PEC bundary R_1 and R_2 and we obtain the following condition

$$J_\nu^{'}(k_\nu R_1) Y_\nu^{'}(k_\nu R_2) - J_\nu^{'}(k_\nu R_2) Y_\nu^{'}(k_\nu R_1) = 0, \tag{4.16}$$

where prime ($'$) indicates the radial derivative. Solving this equation, we can obtain the dispersion relations for TE modes.

The nature of the modes critically depends on the parameters ν and k_ν. It is well known that when k_ν is imaginary, the modal solutions assume the form of the modified Bessel functions. More importantly, in this case, the anisotropic nature of the waveguide allows the order, ν, of the Bessel function to be fractional and even imaginary ($\nu^2 < 0$) [99, 100], which is not possible in isotropic systems. In a non-magnetic medium, for example, a propagating (β is real) TE mode with real k_ν (implying that $k_0^2 \varepsilon_\phi > \beta^2$). If $k_0^2 \varepsilon_r < \beta^2 < k_0^2 \varepsilon_\phi$, then $\nu^2 < 0$ and the order of the mode becomes imaginary. This is seen to occur straightforwardly in a medium with $\varepsilon_r < 0$ and $\varepsilon_\phi > 0$, whereas in a medium with $\varepsilon_r = \varepsilon_\phi$, this situation would not arise [88]. Note that the inequalities reverse if we seek a TE mode with imaginary k_ν described by the modified Bessel functions. The requirements for an imaginary order for the TM modes are actually slightly more involved due to the various possibilities of the material parameters which is discussed in the next subsection. By changing the sign of the dielectric permittivity components, there are various kinds of solutions possible. All the possible solutions of the TE modes for various

Table 4.1: Possible solutions for H_z in a non-magnetic ($\mu_r = \mu_\phi = \mu_z = 1$) homogeneous anisotropic circular coaxial waveguide.

Sr.	ε_r	ε_ϕ	ε_z	Conditions	k_ν^2	ν^2	β	Remarks
1	$+$	$+$	$+$	$k_0^2\varepsilon_r > \beta^2$ $k_0^2\varepsilon_\phi > \beta^2$	$+$	$+$	$\sqrt{k_0^2\varepsilon_\phi - k_\nu^2}$	Solutions similar to positive index fibers, fractional order modes
				$k_0^2\varepsilon_r < \beta^2$ $k_0^2\varepsilon_\phi > \beta^2$	$+$	$-$	$\sqrt{k_0^2\varepsilon_\phi - k_\nu^2}$	Imaginary order modes
				$k_0^2\varepsilon_r > \beta^2$ $k_0^2\varepsilon_\phi < \beta^2$	$-$	$-$	$\sqrt{k_0^2\varepsilon_\phi - k_\nu^2}$	Imaginary order modes
				$k_0^2\varepsilon_r < \beta^2$ $k_0^2\varepsilon_\phi < \beta^2$	$-$	$+$	$\sqrt{k_0^2\varepsilon_\phi - k_\nu^2}$	Plasmonic surface modes
2	$+$	$+$	$-$	H_z same as 1				
3	$+$	$-$	$+$	$k_0^2\varepsilon_r > \beta^2$ $-k_0^2\left\|\varepsilon_\phi\right\| < \beta^2$	$-$	$-$	$i\sqrt{k_0^2\left\|\varepsilon_\phi\right\| + k_\nu^2}$	No propagation
				$k_0^2\varepsilon_r < \beta^2$ $-k_0^2\varepsilon_\phi < \beta^2$	$-$	$+$	$i\sqrt{k_0^2\left\|\varepsilon_\phi\right\| + k_\nu^2}$	No propagation
4	$-$	$+$	$+$	$-k_0^2\left\|\varepsilon_r\right\| < \beta^2$ $k_0^2\varepsilon_\phi > \beta^2$	$+$	$-$	$\sqrt{k_0^2\varepsilon_\phi - k_\nu^2}$	Imaginary order modes
				$-k_0^2\left\|\varepsilon_r\right\| < \beta^2$ $k_0^2\varepsilon_\phi < \beta^2$	$-$	$+$	$\sqrt{k_0^2\varepsilon_\phi - k_\nu^2}$	Plasmonic surface modes
5	$+$	$-$	$-$	H_z same as 3				
6	$-$	$+$	$-$	H_z same as 4				
7	$-$	$-$	$+$	$-k_0^2\left\|\varepsilon_r\right\| < \beta^2$ $-k_0^2\left\|\varepsilon_\phi\right\| < \beta^2$	$-$	$+$	$i\sqrt{k_0^2\left\|\varepsilon_\phi\right\| + k_\nu^2}$	No propagation

possibilities with anisotropic and non-magnetic materials are tabulated in Table 4.1.

Physical applications of Bessel functions with imaginary orders have been rarely reported [99–101]. There are consequences to a fractional or imaginary order, ν. The order of the Bessel function and the field distributions now depend on the propagation constant β, unlike those for an integral order (m) mode in isotropic media. We notice in Table 4.1 that the imaginary order modes ($\nu^2 < 0$) are even possible if the all permittivity components are positive (Sr. 1 Table 4.1). There are some surface plasmonic modes as presented by Table 4.1 Sr. no. 1, 4 and 6. In the plasmonic mode, the field decay along the radial direction but can propagate along the axial direction. There is one very important issue is that if the $\varepsilon_\phi < 0$, then the propagation constant β becomes imaginary and there is no propagation is possible for TE modes (Sr. 3,5,7 Table 4.1). The nature of the fields of the modes described by the Bessel functions with imaginary orders will be discussed in the later subsections of this chapter.

4.2.2 TM Modes in a Coaxial Anisotropic Fiber

Now we describe the TM modes in the coaxial anisotropic waveguide. The field components for TM modes

$$E_r \neq 0, E_\phi \neq 0, E_z \neq 0, \tag{4.17a}$$

$$H_r \neq 0, H_\phi \neq 0, H_z = 0. \tag{4.17b}$$

We again use the method of separation of variables and let

$$E_z\left(r,\phi\right) = R\left(r\right)\Phi\left(\phi\right). \tag{4.18}$$

Following a similar approach as for the TE modes, for TM modes we can get the azimuthal component of the E_z field as

$$\Theta\left(\phi\right) = Ce^{im\phi}, \tag{4.19}$$

where m is an integer and C is a constant. The radial part of E_z is the solution of the differential equation

$$r^2 \frac{d^2 R(r)}{dr^2} + r\frac{dR(r)}{dr} + \left(k_\tau^2 r^2 - \tau^2\right) R(r) = 0, \tag{4.20}$$

in which

$$k_\tau^2 = \frac{\varepsilon_z}{\varepsilon_r}\left\{k_0^2 \varepsilon_r \mu_\phi - \beta^2\right\}, \tag{4.21a}$$

$$\tau^2 = \frac{\varepsilon_\phi}{\varepsilon_r}\left\{\frac{k_0^2 \varepsilon_r \mu_\phi - \beta^2}{k_0^2 \varepsilon_\phi \mu_r - \beta^2}\right\} m^2. \tag{4.21b}$$

If we see the expressions of the k_ν and ν in Eq. (4.13) of TE modes and the expressions of the k_τ and τ in Eq. (4.21) of TM modes are exactly complimentary to each other, but with the permittivity replaced by the permeability components and vice versa. So to avoid the confusion between the expressions of the TE and TM modes, we used different symbols. The general form of the field component E_z of the TM mode is given by

$$E_z(r, \phi, z, t) = \left\{B_1 J_\tau(k_\tau r) + B_2 Y_\tau(k_\tau r)\right\} e^{im\phi} e^{i(\beta z - \omega t)}. \tag{4.22}$$

where k_τ and τ is given by the Eq. (4.21). The coefficients B_1 and B_2 can be obtained by setting the tangential components of the field, $E_z = 0$ for the field at the PEC boundaries, resulting in

$$J_\nu(k_r R_1) Y_\nu(k_r R_2) - J_\nu(k_r R_2) Y_\nu(k_r R_1) = 0. \tag{4.23}$$

This the dispersion relation of the TM modes of the coaxial waveguides. After taking the various combinations of the sign of permittivity components, there are various types of solutions possible. All these solutions for a non-magnetic anisotropic circular coaxial fiber are listed in Table 4.2. Due to the involvement of ε_z in Eq. (4.21a), there some more solutions that are not possible in the case of TE mode of non-magnetic and anisotropic circular coaxial fiber as we have seen in the Table 4.1 of the previous subsection . In the TM mode case, if the $\varepsilon_z < 0$ then in some cases when there are modes with essentially no cutoff frequency (Sr. 2,5 Table 4.2). Here there is only one case $\varepsilon_r < 0, \varepsilon_z < 0$ for which there is no propagation (Sr. 6 Table 4.2).

Table 4.2: Possible solutions for E_z in a non-magnetic ($\mu_r = \mu_\phi = \mu_z = 1$) homogeneous anisotropic circular coaxial waveguide.

Sr.	ε_r	ε_ϕ	ε_z	Conditions	k_τ^2	τ^2	β	Remarks
1	$+$	$+$	$+$	$k_0^2\varepsilon_r > \beta^2$ $k_0^2\varepsilon_\phi > \beta^2$	$+$	$+$	$\sqrt{k_0^2\varepsilon_r - \frac{\varepsilon_r}{\varepsilon_z}k_\tau^2}$	Solutions similar to positive index fibers, fractional order modes
				$k_0^2\varepsilon_\rho > \beta^2$ $k_0^2\varepsilon_\phi < \beta^2$	$+$	$-$	$\sqrt{k_0^2\varepsilon_r - \frac{\varepsilon_r}{\varepsilon_z}k_\tau^2}$	Imaginary order modes
				$k_0^2\varepsilon_r < \beta^2$ $k_0^2\varepsilon_\phi > \beta^2$	$-$	$-$	$\sqrt{k_0^2\varepsilon_r - \frac{\varepsilon_r}{\varepsilon_z}k_\tau^2}$	Imaginary order modes
				$k_0^2\varepsilon_r < \beta^2$ $k_0^2\varepsilon_\phi < \beta^2$	$-$	$+$	$\sqrt{k_0^2\varepsilon_r - \frac{\varepsilon_r}{\varepsilon_z}k_\tau^2}$	Plasmonic surface modes
2	$+$	$+$	$-$	$k_0^2\varepsilon_r > \beta^2$ $k_0^2\varepsilon_\phi > \beta^2$	$-$	$+$	$\sqrt{k_0^2\varepsilon_r + \frac{\varepsilon_r}{\lvert\varepsilon_z\rvert}k_\tau^2}$	No cutoff
				$k_0^2\varepsilon_r > \beta^2$ $k_0^2\varepsilon_\phi < \beta^2$	$-$	$-$	$\sqrt{k_0^2\varepsilon_r + \frac{\varepsilon_r}{\lvert\varepsilon_z\rvert}k_\tau^2}$	No cutoff
				$k_0^2\varepsilon_r < \beta^2$ $k_0^2\varepsilon_\phi > \beta^2$	$+$	$-$	$\sqrt{k_0^2\varepsilon_r + \frac{\varepsilon_r}{\lvert\varepsilon_z\rvert}k_\tau^2}$	No cutoff
				$k_0^2\varepsilon_r < \beta^2$ $k_0^2\varepsilon_\phi < \beta^2$	$+$	$+$	$\sqrt{k_0^2\varepsilon_r + \frac{\varepsilon_r}{\lvert\varepsilon_z\rvert}k_\tau^2}$	No cutoff
3	$+$	$-$	$+$	$k_0^2\varepsilon_r > \beta^2$ $-k_0^2\lvert\varepsilon_\phi\rvert < \beta^2$	$+$	$+$	$\sqrt{k_0^2\varepsilon_r - \frac{\varepsilon_r}{\varepsilon_z}k_\tau^2}$	Solutions similar to positive index fibers, fractional order modes
				$k_0^2\varepsilon_r < \beta^2$ $-k_0^2\lvert\varepsilon_\phi\rvert < \beta^2$	$-$	$-$	$\sqrt{k_0^2\varepsilon_r - \frac{\varepsilon_r}{\varepsilon_z}k_\tau^2}$	Imaginary order modes

Sr.	ε_r	ε_ϕ	ε_z	Conditions	k_τ^2	τ^2	β	Remarks
4	$-$	$+$	$+$	$-k_0^2\left\|\varepsilon_r\right\| < \beta^2$ $k_0^2\varepsilon_\phi > \beta^2$	$+$	$+$	$\sqrt{-k_0^2\left\|\varepsilon_r\right\| + \frac{\left\|\varepsilon_r\right\|}{\varepsilon_z}k_\tau^2}$	Fractional order modes
				$-k_0^2\left\|\varepsilon_r\right\| < \beta^2$ $k_0^2\varepsilon_\phi < \beta^2$	$+$	$-$	$\sqrt{-k_0^2\left\|\varepsilon_r\right\| + \frac{\left\|\varepsilon_r\right\|}{\varepsilon_z}k_\tau^2}$	Imaginary order modes
5	$+$	$-$	$-$	$k_0^2\varepsilon_r > \beta^2$ $-k_0^2\left\|\varepsilon_\phi\right\| < \beta^2$	$-$	$+$	$\sqrt{k_0^2\varepsilon_r + \frac{\varepsilon_r}{\left\|\varepsilon_z\right\|}k_\tau^2}$	No cutoff
				$k_0^2\varepsilon_r < \beta^2$ $-k_0^2\left\|\varepsilon_\phi\right\| < \beta^2$	$+$	$-$	$\sqrt{k_0^2\varepsilon_r + \frac{\varepsilon_r}{\left\|\varepsilon_z\right\|}k_\tau^2}$	No cutoff
6	$-$	$+$	$-$	$-k_0^2\left\|\varepsilon_r\right\| < \beta^2$ $k_0^2\varepsilon_\phi > \beta^2$	$-$	$+$	$i\sqrt{k_0^2\left\|\varepsilon_r\right\| + \frac{\left\|\varepsilon_r\right\|}{\left\|\varepsilon_z\right\|}k_\tau^2}$	No propagation
				$-k_0^2\left\|\varepsilon_r\right\| < \beta^2$ $k_0^2\varepsilon_\phi < \beta^2$	$-$	$-$	$i\sqrt{k_0^2\left\|\varepsilon_r\right\| + \frac{\left\|\varepsilon_r\right\|}{\left\|\varepsilon_z\right\|}k_\tau^2}$	No propagation
7	$-$	$-$	$+$	$-k_0^2\left\|\varepsilon_r\right\| < \beta^2$ $-k_0^2\left\|\varepsilon_\phi\right\| < \beta^2$	$+$	$+$	$\sqrt{-k_0^2\left\|\varepsilon_r\right\| - \frac{\left\|\varepsilon_r\right\|}{\varepsilon_z}k_\tau^2}$	Fractional order modes

4.3 Modal Fields and Dispersions in a homogeneously filled anisotropic coaxial waveguide

In Chapter 3, we homogenized a cylindrically symmetric microwire of nanoporous alumina and found that it has uniaxial anisotropy, i.e., $\varepsilon_r \neq \varepsilon_\phi = \varepsilon_z$. Due to the varying fill fraction with the radial distance, the alumina microtube is actually an inhomogeneously filled anisotropic waveguide. However, to understand the nature of the modes in cylindrically anisotropic medium, it would be good to separate out the effects of anisotropy and inhomogeneity. Hence, in this section, we analyze the modes of a homogeneously filled anisotropic waveguide. As an approximation, let us assume that the nanoporus alumina fiber is homogeneously filled and it has uniaxial anisotropy. Additionally PEC boundary conditions are applied symmetrically at $r = R_1$ and $r = R_2$ thereby reducing it to a coaxial waveguide.

In the previous section, we discussed the general solutions of TE and TM modes of a homogeneously filled anisotropic ($\varepsilon_r \neq \varepsilon_\phi \neq \varepsilon_z$) coaxial waveguide. If in the Tables 4.1 and 4.2, we use the anisotropy as $\varepsilon_r \neq \varepsilon_\phi = \varepsilon_z$ then the number of possibilities are reduced. From these two tables we have noticed that the TM modes present more interesting cases with than the TE modes with dielectric anisotropy. For example, there are modes with no cut-off frequencies in some cases. Hence we discuss the TM modes here. The numerical analysis of the TE modes can be done in a similar manner. As we have seen, the nanopores of cylindrical nanoporous alumina microtube can be filled with suitable materials like polymers, liquids, metals etc. which can give different signs to the different permittivity components. Here we considered two cases to demonstrate the nanoporous alumina coaxial fiber. First the nanopores filled with air and the second the nanopores filled with silver metal.

In this chapter we have used mode index notation $\mathrm{TM}_{m,n}$ to avoid the confusion for higher index modes, where m is the azimuthal integral order of the mode which appears in the solution of the angular part of Eq. (4.12) or (4.19), and n is the sequence of number of roots of dispersion relation for a fixed azimuthal order m. Since in the anisotropic coaxial waveguides there can exist the integral, fractional and imaginary order modes, therefore, in the next subsection we shall briefly introduce about the Bessel functions of various kinds of orders which will help to understand the nature of the modes of the anisotropic fiber.

4.3.1 Bessel Functions of Integral, Fractional and Imaginary Orders

The Bessel functions are the solutions of the Bessel differential equation [102]

$$x^2\frac{d^2y}{dx^2}+x\frac{dy}{dx}+(x^2-\alpha^2)y=0, \tag{4.24}$$

where constant α is called the order of the Bessel functions. The above equation have two solutions which are called Bessel functions of first kind (J_α) and Bessel functions of second kind or Neumann function (Y_α). For the purely imaginary argument the solutions of the Eq. (4.24) are called Modified Bessel function of first kind (I_α) and Modified Bessel function of second kind (K_α). The Bessel functions order, α, can be integral, fractional, imaginary or complex numbers which will reflect on the properties of the Bessel functions. Some plots of Bessel functions of different kind of orders are shown in Fig. 4.2 [103].

We see that the integral order Bessel functions either oscillate or decay as shown in Fig. 4.2(a) and 4.2(b). In the integral order case the minimum variation of α is 1, while this variation in the fractional order case can be extremely small. The fractional order Bessel functions also oscillate or decay but their variation with the order α become slow or fast as the functions orders slow or fast than the integral order Bessel functions. For example in the Fig. 4.2(c) the functions orders are 1/2 and 1/3 then the variation in the function is small. If the function order would become 1/2.1 or 17/2 then the function would change very slow or fast compared to the function of order 1/2. Similarly this also happens for the modified Bessel functions too, but only thing is that they always decay with increasing x. The behavior of the imaginary order Bessel functions are very

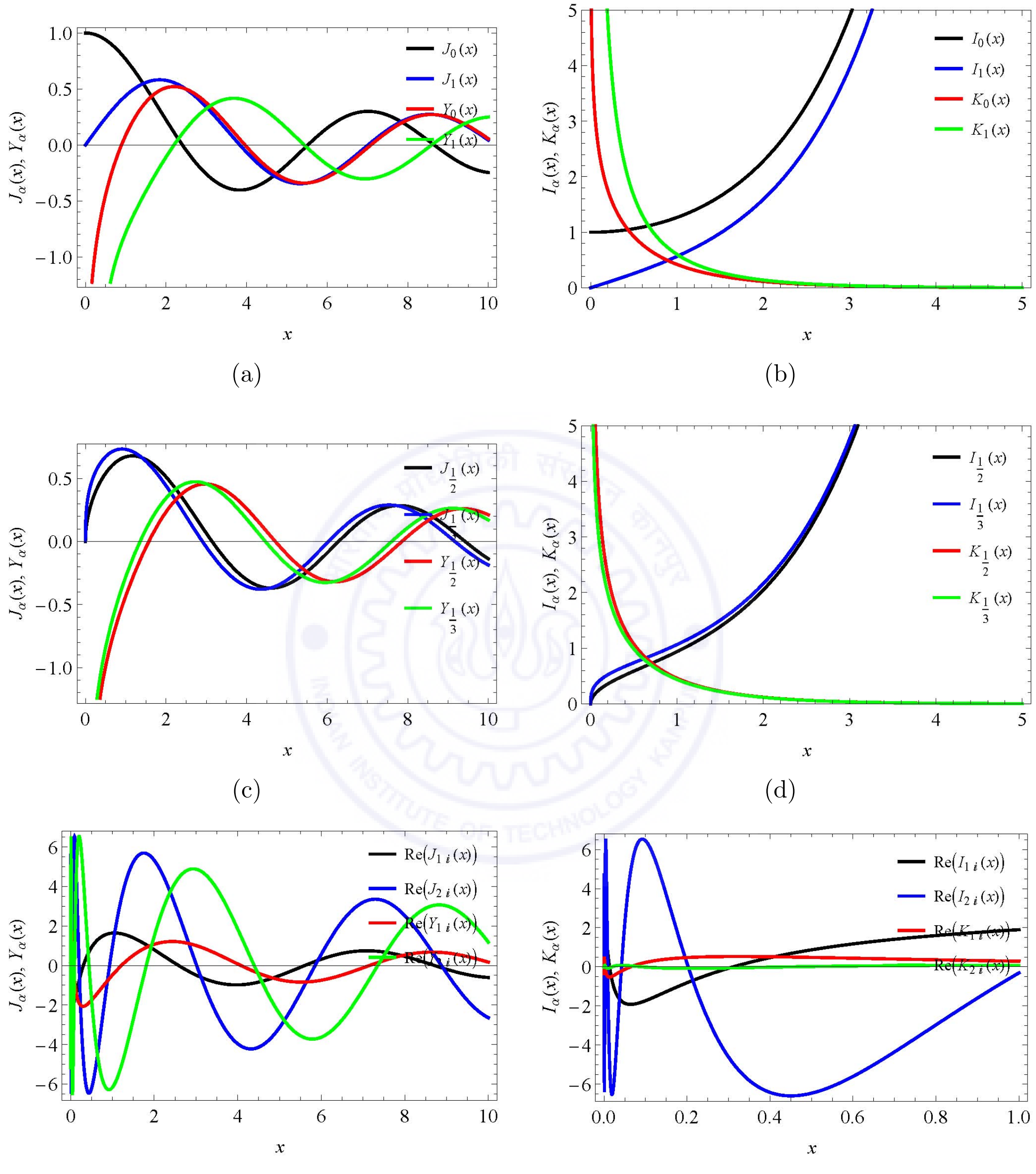

(a) (b)

(c) (d)

(e) (f)

Figure 4.2: Plots of the Bessel functions J_α and Y_α (left panel), and plots of the Modified Bessel functions I_α and K_α (right panel). Plots of (a) and (b) for integral order, (c) and (d) for fractional order, and (e) and (f) for imaginary order (Olver et al., NIST Handbook of Mathematical Functions,2010).

different than the integral and fractional order Bessel functions. They always oscillate whether they are ordinary Bessel functions (Fig. 4.2(e)) or Modified Bessel functions(Fig. 4.2(f)). As the argument, x, decrease, the functions oscillations increase. The functions amplitudes and oscillations increase tremendously with their order as argument tends to zero. In fact, these functions do not have a well defined limit as $x \to 0$, and are reminiscent functions like $\sin(1/x)$ that have an essential singularity at $x = 0$. More details of the Bessel functions can be found in Ref. [103]. In the next subsection, we shall use these Bessel functions to explain the mode properties of the homogeneously filled anisotropic coaxial waveguides.

4.3.2 Modal Fields in homogeneous Anisotropic Waveguides

At cut-off, every type of mode has an integral order, the order τ or ν of the Bessel function changes with β or the frequency, ω, for a given m. One of the consequences is that the modes become comparatively more confined near the center with increasing β or ω. This confinement is more drastic than in ordinary dielectric fibers as the effects of β or ω are manifested within the Bessel functions order (τ or ν) rather than only the argument (k_r). Figure 4.3 shows this behavior for the $\mathrm{TM}_{1,1}$ and TM $_{2,2}$ modes. In contrast to a waveguide filled with an isotropic medium where the argument of the Bessel function (k_r) changes with β, here, the order ν of the Bessel function itself evolves with β. In Fig. 4.3, this is strictly true that at $\beta = 0$ represents the onset of a stop band and a condition where the modes may be described purely as TE or TM, hence, it is not unreasonable to show them as we have also shown alongside the field distributions for $\beta \neq 0$. We highlight that the field profile for the first two sub-figures varies subtly for the non-zero beta value shown in the remaining figures, as a result of the mode order becoming fractional from a integral one.

For air inclusions and at 0.23 fill fraction, the field component (E_z) for the TM modes is plotted in Fig. 4.4. In this figure, the first row is for an isotropic alumina

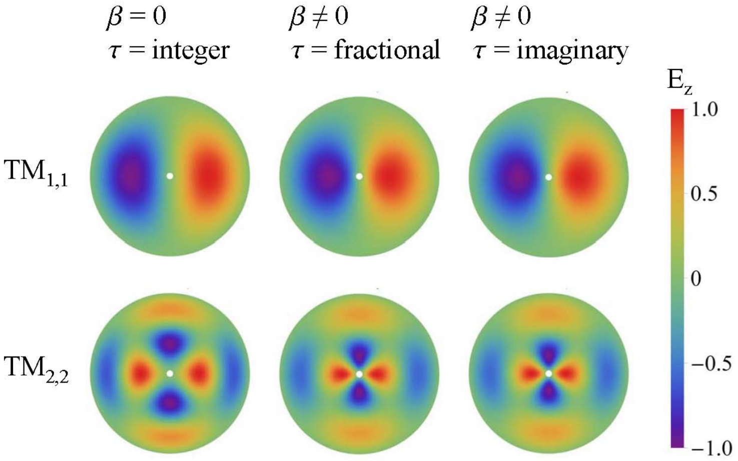

Figure 4.3: The behavior of low-order modes ($TM_{1,1}$ and $TM_{2,2}$) in an anisotropic nanoporous alumina coaxial fiber for dimensions $R_1 = 0.5$ μm and $R_2 = 12.5$ μm. Col. 1: Eigen modes at $\beta = 0$, $\tau = m$ integral order, Col. 2: modes at $\varepsilon_r = 2.467$, $\varepsilon_\phi = \varepsilon_z = 2.638$, and $\beta \neq 0$, $\tau \neq m$ fractional order, Col. 3: modes at $\varepsilon_r = 2.638$, $\varepsilon_\phi = \varepsilon_z = 2.467$, and $\beta \neq 0$, $\tau \neq m$ imaginary order. Dielectric constants are at wavelength 633 nm.

fiber with positive $\varepsilon_r = \varepsilon_\phi = \varepsilon_z = 3.118$ at wavelength $\lambda = 632.8$ nm for reference. In the case of an air filled nanoporous fiber with $\varepsilon_r = 2.467, \varepsilon_\phi = \varepsilon_z = 2.638$, there are fractional order modes possible at wavelength $\lambda = 632.8$ nm as shown in Fig. 4.4. We see that the confinement of the electric field is higher than the isotropic fiber. It is more visible for the higher order modes. Imaginary order modes are also possible for $\varepsilon_r = 2.638, \varepsilon_\phi = \varepsilon_z = 2.467$, and $\lambda = 632.8$ as shown in Fig. 4.4. Here the confinement of light within the fiber is very high and the light is highly concentrated towards the center of the fiber. For the imaginary order modes, as the index m increases, the fields spread all over the volume while concentrating towards the center. By contrast, in the isotropic fiber with positive ε, the fields move away from the center of the fiber for large azimuthal index m. These modes that are localized to the edge of the fiber are conventionally termed “whispering gallery modes”.

Metals have complex permittivity with negative real parts below their plasma fre-

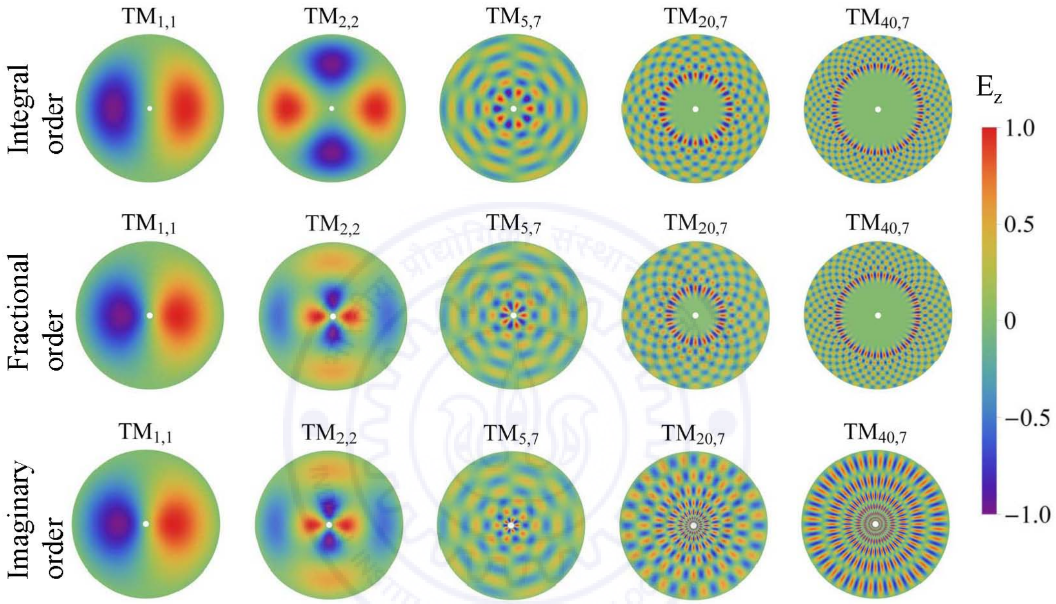

Figure 4.4: The computed electric fields (E_z) of modes in cylindrical nanoporous alumina when nanopores have air inclusion for $R_1 = 0.5\ \mu$m, $R_2 = 12.5\ \mu$m for $m = 1, 2, 5, 20, 40$. Top row shows the Bessel modes in an isotropic alumina fiber with real integral orders for $\varepsilon_r = \varepsilon_\phi = \varepsilon_z = 3.118$. The middle row shows Bessel modes in an anisotropic nanoporous alumina fiber with fractional order and positive dielectric permittivity components for $\varepsilon_r = 2.467$ and $\varepsilon_\phi = \varepsilon_z = 2.638$. The bottom row shows the fields for Bessel modes of anisotropic nanoporous alumina fiber with imaginary orders and $\varepsilon_r = 2.638$ and $\varepsilon_\phi = \varepsilon_z = 2.467$. Relative permittivity components are at wavelength 632.8 nm.

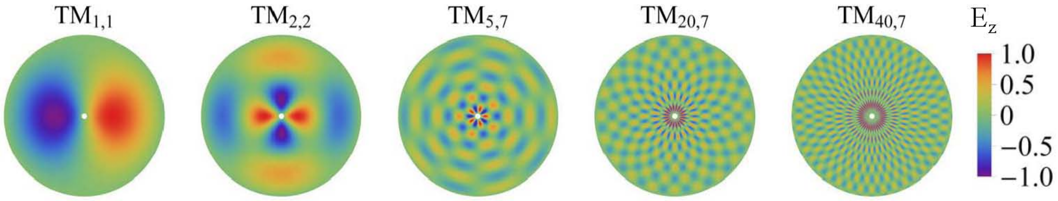

Figure 4.5: The computed electric fields (E_z) of modes in cylindrical nanoporous alumina when nanopores have silver metal inclusion for $R_1 = 0.5$ μm, $R_2 = 12.5$ μm for $m = 1, 2, 5, 20, 40$. The fields for Bessel modes of anisotropic nanoporous alumina fiber with complex orders and $\varepsilon_r = -1.288 + i0.053$ and $\varepsilon_\phi = \varepsilon_z = 6.244 + i0.027$. Relative permittivity components are at wavelength 632.8 nm.

quencies which lie in UV range for most of the metals. Filling the nanopores of the cylindrical nanoporous alumina with silver metal, the effective permittvity components of the cylindrical nanoporous alumina show the hyperbolic dispersion in some frequency range. Field plots for TM modes for the case of silver inclusion in nanoporous alumina with $\varepsilon_r = -1.288+i0.053, \varepsilon_\phi = \varepsilon_z = 6.244+i0.027$ at wavelength $\lambda = 632.8$ nm have been shown in Fig. 4.5. We see that the modes are confined like the imaginary order modes of the air inclusion case. But in the silver inclusion case, complex order modes are also possible because of the complex permittivity of the metal. Here also the fields are spread over the volume while concentrating towards the fiber axis. If we vary the real part of the dielectric permittivity and keeping imaginary part of the dielectric permittivity constant then it will change the cutoff frequency of the modes and field confinement, but no change in the losses will occur. The change of the cutoff and confinement also depend on the levels of the anisotropy. On the other hand, if we keep real part of the dielectric permittivity constant and vary the imaginary part, then it will increase the losses drastically and slight change on the cutoff and field distribution. For smaller imaginary part of dielectric permittivity losses will be lower and for larger imaginary part of dielectric permittivity the losses will be higher. In all the applications, there is a need to keep imaginary part of dielectric permittivity small as much as it can be.

The modes with imaginary orders are very interesting in that the higher-order (large

m) modes are localized near the central region of the waveguide (see Fig. 4.4). In contrast, the large m whispering gallery modes are concentrated at the edges of a waveguide filled with an isotropic positive material (Fig. 4.2). Further, these Bessel functions with imaginary orders undergo large oscillations near the center and need not converge at $r = 0$ [99], a reflection of the geometric singularity at the axis, which cannot be attained in a physical system. The PEC boundary condition applied at $r = R_1$, however, prevents any issues with the mathematical singularities of the function at the origin ($r = 0$). The number of oscillations of the wave-field near $r = 0$ increases with the order τ (or ν) of the mode. Even for modes with real fractional orders that result for anisotropic fibers, there is a comparatively larger confinement of the higher-order m modes (Fig. 4.4).

The origin of this spreading out of the fields of the modes with large m well into the interior of the waveguide lies in the dispersion of the wave in a hyperbolic medium with cylindrical symmetry. Consider at very small length scales, when a wave propagating in the (r, ϕ) plane would essential look like a plane wave, so that the local wave-vector can be considered to be along the ray. If (k_r, k_ϕ) be locally the wave-vector, the phase shift for an infinitesimal displacement $(\delta r, r\delta\phi)$ would be $\exp[i(k_r\delta r + k_\phi r\delta\phi)]$. Demanding a single valued function constrains that $k_\phi = m/r$, where m is an integer. Under these circumstances (in analogy to a wave in an anisotropic medium in flat rectangular space), locally we have

$$\frac{k_r^2}{\varepsilon_\phi} + \frac{m^2}{r^2\varepsilon_r} = \frac{\omega^2}{c^2}. \tag{4.25}$$

In a normal positive medium with $\varepsilon_r > 0$ and $\varepsilon_\phi > 0$, as the wave moves towards the origin, $r \to 0$ and $k_\phi \to \infty$, and k_r becomes imaginary. Thus, the wave decays exponentially towards the origin for the large m whispering gallery modes and avoids the region near the origin. On the contrary, in an hyperbolic medium with $\varepsilon_r \cdot \varepsilon_\phi < 0$, k_r remains real and large for $k_\phi \to \infty$ (large m), and the wave can effectively propagate in the region near the origin with the only difference that the fields oscillate more and more rapidly along r closer to the origin. This is due to the fact that propagation of higher-order modes that can be supported in media with hyperbolic dispersion as seen earlier in the case of the hyperlens [104]. In that work, the higher-order modes carrying spatially sub-wavelength (rapidly varying) image features could be propagated across the radial direction and imaged out into far-field radiating modes [12]. For example, in Eq. (4.25), if $\varepsilon_r < 0$ and $\varepsilon_z > 0$, then k_r increases without bound along with β. Thus, very large oscillatory field variations in the radial direction can be supported close the center of the fiber and the field can occupy large modal volumes.

4.3.3 Modal Dispersions in Homogeneous Anisotropic Waveguide

We proceeded then to calculate the dependence of the propagation constant β on the frequency (the dispersion) for the anisotropic waveguide. The Fig. 4.6 shows the dispersions in an nanoporous alumina fiber with air and silver inclusions at fill fraction of 0.23 and 0.08 respectively. In the 1-35 THz frequency range, alumina has a number phonon resonances. So we used experimental data for the dielectric permittivities of the alumina host [105] and the silver inclusion [7, 106]. For comparison the modal dispersion of the isotropic alumina fiber is also shown. The cutoff frequencies of modes of isotropic alumina fiber and anisotropic nanoporous alumina fiber for air inclusion are calculated in the 1-35 THz range and tabulated in the Tables 4.3 and 4.4 respectively.

As shown in Fig. 4.6(a), the alumina has phononic resonances at 13 THz and 17 THz, which cause strong dispersion in the effective permittivity of the nanoporous alumina. Both fibers, isotropic as well as anisotropic, show forward wave propagation from 5.5-11.5 THz. In this range losses ($\mathrm{Im}(\beta) << \mathrm{Re}(\beta)$) are very small and fibers are suitable for practical applications. Because of phononic resonance of alumina, from 11.5-22 THz range there are several narrow bands of backward and forward wave propagation. The backward propagating waves usually have extreme losses. In the 22-25.7 THz frequency range, there is negative phase velocity with high loss in the nanoporous alumina fiber for

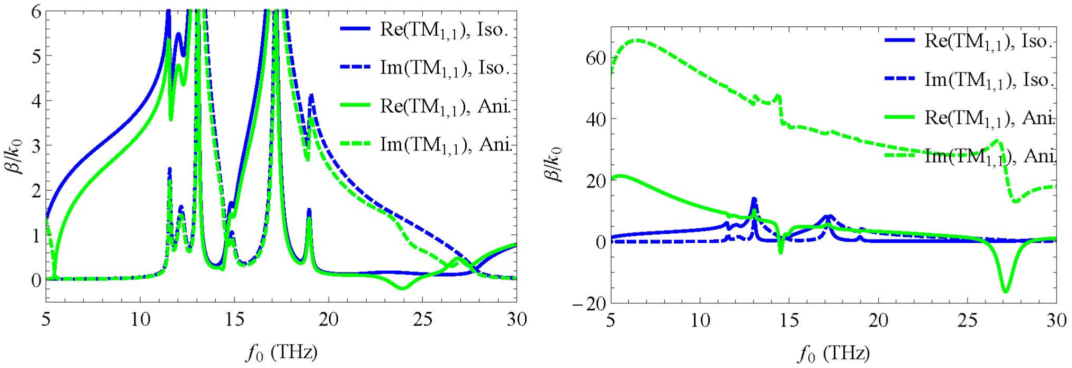

(a) (b)

Figure 4.6: The computed $TM_{1,1}$ dispersive dispersion of modes in cylindrical nanoporous alumina when nanopores have (a) air inclusion with fill fraction 0.23 and (b) silver inclusion with fill fraction 0.08. $R_1 = 0.5$ μm, $R_2 = 12.5$ μm. The air permittivity was 1, the permittivity of alumina taken from Ref. Rajab et al. 2008 and for silver from Ref. Ordal et al. 1983.

Table 4.3: The dispersive cutoff frequencies (in THz) of TM modes of a non-magnetic homogeneous isotropic alumina coaxial fiber. Cutoff frequencies are calculated in the 1-35 THz frequency range for various modes.

Mode	f_{c1}(THz)	f_{c2}(THz)	f_{c3}(THz)
$TM_{0,1}$	3.6371 - i 0.0063	14.9586 - i 0.1575	27.5003 - i 0.3531
$TM_{0,2}$	7.0699 - i 0.0265	15.0282 - i 0.1524	29.2919 - i 0.2667
$TM_{1,1}$	4.5847 - i 0.0102	14.9684 - i 0.1566	27.8242 - i 0.3339
$TM_{1,2}$	7.6983 - i 0.0323	15.0601 - i 0.1509	29.8815 - i 0.2461

air inclusion only which is not possible in isotropic fibers. This is a very unique feature of the nanoporous alumina. Beyond 25.7 THz the nanoporous alumina fibers again become useful for applications.

For the case of silver inclusion in the nanoporous alumina, the high negative permittivity of silver always dominates over the permittivity of alumina host and creates extreme anisotropy. Since the metals are very lossy media. Therefore, including the metals into the structured system such as nanoporous alumina increases the loss in the anisotropic system. Figure 4.6(b) shows the dispersion and Table 4.5 shows the cutoff frequencies of

Table 4.4: The dispersive cutoff frequencies (in THz) of TM modes of a non-magnetic homogeneous nanoporous alumina coaxial fiber for air inclusion in the nanopores. Cutoff frequencies are in the 1-35 THz frequency range.

Mode	f_{c1}(THz)	f_{c2}(THz)	f_{c3}(THz)	f_{c4}(THz)
$TM_{0,1}$	4.3450 - i 0.0085	14.9262 - i 0.1599	24.1951 - i 0.6636	27.3489 - i 0.3619
$TM_{0,2}$	8.1955 - i 0.0359	15.0640 - i 0.1501	24.8165 - i 0.5454	29.0552 - i 0.2651
$TM_{1,1}$	5.4478 - i 0.0138	14.9681 - i 0.1565	24.3554 - i 0.6256	27.6089 - i 0.3441
$TM_{1,2}$	8.8376 - i 0.0436	15.1223 - i 0.1487	24.9237 - i 0.5322	29.7192 - i 0.2384

the waveguide modes with silver nanowire inclusions in the nanopores of the cylindrical nanoporous alumina. The Fig. 4.6(b) shows that there is extreme loss ($\mathrm{Im}(\beta) >> \mathrm{Re}(\beta)$) over almost the entire range. But in a very wide frequency range, from 6.6-25.5 THz, there is backward wave propagation effectively. In a narrow band around 14.5 THz and a wide band 26-28.3 THz, there is negative phase velocity. The nanoporous alumina with silver inclusion from 27-28 THz might be potentially useful for applications because of lower losses.

The losses due to the metal inclusion vary over the electromagnetic spectrum. These losses are very less in the visible range. The solutions for modes for homogenized fibers corresponding to silver-filled nanoporous alumina, the ratio of the imaginary and real parts of β at 632.8 nm wavelength was on the order of 10^{-3} for $TM_{1,1}$ modes ($f = 0.08$) with complex order. Thus, while the fibers discussed here are clearly not meant for traditional transmission applications, they have immense potential for several other purposes such as coupling the near-field into a waveguide or waveguide couplers and shifters. The complex order modes always will be lossy. While absorption can not be removed totally, but it can be lowered down with very dilute metallic inclusions. For very dilute metallic inclusions with very low fill fraction, we may not obtain hyperbolic dispersions. So we have to optimize the parameters of the dielectric permittivity to obtain complex order modes as per need.

For non-metallic inclusions, we can get the situation where $\mathrm{Re}(\beta) >> \mathrm{Im}(\beta)$, as

Table 4.5: The dispersive cutoff frequencies (in THz) of TM modes of a non-magnetic homogeneous nanoporous alumina coaxial fiber for silver metal inclusion in the nanopores. Cutoff frequencies of fibers are in the 1-1500 THz frequency range.

Mode	f_{c1}(THz)	f_{c2}(THz)	f_{c3}(THz)
$TM_{0,1}$	3.3632 - i 0.0054	14.9565 - i 0.1577	27.4242 - i 0.3580
$TM_{0,2}$	6.6161 - i 0.0228	15.0111 - i 0.1534	28.9349 - i 0.2807
$TM_{1,1}$	4.2489 - i 0.0087	14.9645 - i 0.1570	27.6980 - i 0.3412
$TM_{1,2}$	7.2308 - i 0.0280	15.0353 - i 0.1520	29.4314 - i 0.2616

for example can be seen in Fig. 4.6(a) in the case of air inclusion. In this situation the losses will be almost zero and such arrangement can be used for practical purpose. As we see in the previous paragraph in the case of metallic inclusions, the losses are so high that in this case the waveguide may not be practically suitable for applications, although this arrangement has hyperbolic dispersion. But, if we are able to fill the nanopores with such electrically conducting materials that have almost zero imaginary part of dielectric permittivity (very low loss), then we can get Re(β) >> Im(β) and hyperbolic behavior simultaneously.

4.4 Guided Modes in Homogeneously Filled Anisotropic Hollow Fiber

It is also important to realize that the general nature of these modal solutions are not limited by the application of PEC boundaries. The only restriction would be for the nanoporous alumina regions to have a larger dielectric permittivity than the surrounding medium. Having dielectric boundaries, for example by having a hollow core and no aluminum coating on the outer surface, causes the waveguide to be inhomogeneous and support hybrid (the so-called HE and EH) modes. Fibers with hollow cores are important for various issues of confinement of light as in hollow core photonic crystal fibers.

Now we consider a general case in which the PEC condition in the core ($r < R_1$) and outside region ($r > R_2$) of the homogeneously filled waveguide have been relaxed (4.1). Assuming that in core and the outside region have same non-magnetic and isotropic material with dielectric permittivity ε_1, then the nature of the field be same in core and outer region. For the guided modes the longitudinal field components in region 1, 2 and 3 can be expressed as

$$E_{1z} = C_1 I_{\tau 1}(\gamma_{\tau 1} r) e^{im\phi} e^{i(\beta z - \omega t)}, \tag{4.26a}$$

$$H_{1z} = C_2 I_{\nu 1}(\gamma_{\nu 1} r) e^{im\phi} e^{i(\beta z - \omega t)}, \tag{4.26b}$$

$$E_{2z} = (C_3 J_{\tau 2}(\gamma_{\tau 2} r) + C_4 Y_{\tau 2}(\gamma_{\tau 2} r)) e^{im\phi} e^{i(\beta z - \omega t)}, \tag{4.26c}$$

$$H_{2z} = (C_5 J_{\nu 2}(\gamma_{\nu 2} r) + C_6 Y_{\nu 2}(\gamma_{\nu 2} r)) e^{im\phi} e^{i(\beta z - \omega t)}, \tag{4.26d}$$

$$E_{3z} = (C_7 K_{\tau 3}(\gamma_{\tau 3} r)) e^{im\phi} e^{i(\beta z - \omega t)}, \tag{4.26e}$$

$$H_{3z} = (C_8 K_{\nu 3}(\gamma_{\nu 3} r)) e^{im\phi} e^{i(\beta z - \omega t)}, \tag{4.26f}$$

where τ's and ν's are given by Eqs. (4.21b) and (4.13b) respectively, and γ_τ's and γ_ν's by the following expressions:

$$\gamma_{\tau i} = \frac{\varepsilon_{zi}}{\varepsilon_{ri}} \sqrt{\omega^2 \varepsilon_{ri} \mu_{\phi i} - \beta^2}, \tag{4.27a}$$

$$\gamma_{\nu i} = \frac{\mu_{zi}}{\mu_{ri}} \sqrt{\omega^2 \varepsilon_{\phi i} \mu_{ri} - \beta^2}. \tag{4.27b}$$

Substituting Eqs. (4.26) in Eqs. (4.6) the transverse components can be obtained. Equating the parallel components of the fields at boundary R_1 and R_2 we get eight homogeneous equations in eight unknowns. For existence of the non-trivial solutions, the determinant of the coefficient matrix must be zero. This determinant is solved for β to obtain the dispersion relations. Considering that in the region 2 the solutions are oscillatory, then for $\varepsilon_r > 0$, $\varepsilon_\phi > 0$ and $\varepsilon_z > 0$, the guided mode conditions will be

$$\varepsilon_1 < \beta^2/k_0^2 < \varepsilon_r, \quad \text{and} \quad \varepsilon_1 < \beta^2/k_0^2 < \varepsilon_\phi. \tag{4.28}$$

For the guided modes, when $\varepsilon_r > \varepsilon_\phi$, there is one condition called the normalized propagation constant defined as

$$V = k_0 R_2 \sqrt{\varepsilon_\phi - \varepsilon_1}. \tag{4.29}$$

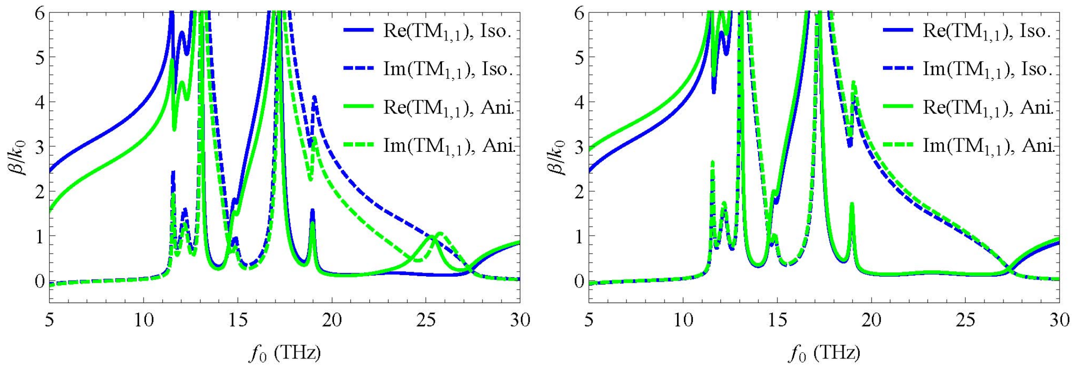

(a) (b)

Figure 4.7: The modal dispersions of the homogeneously filled nanoporous alumina hollow waveguides embedded in air and when the nanopoers are filled with (a) air for fill fraction 0.23 and (b) silver metal for fill fraction 0.08. The permittivity of alumina taken from Ref. Rajab et al. 2008 and for silver from Ref. Ordal et al. 1983.

Similarly if $\varepsilon_r < 0$, $\varepsilon_\phi > 0$ and $\varepsilon_z > 0$, then the condition for a guided mode will be

$$-|\varepsilon_r| < \beta^2/k_0^2, \quad \text{and} \quad \varepsilon_1 < \beta^2/k_0^2 < \varepsilon_\phi, \tag{4.30}$$

and the normalized propagation constant will be same as when all the permittivity components are positive. By choosing the different signs for the dielectric permittivity components, there are only few cases that are listed in Table 4.6 where the guided modes are possible. Let $a = 5\mu$m and $b = 15\mu$m, then for the nanoporous alumina fiber with air inclusion embedded in air, at visible frequency He-Ne laser wavelength, the V is 180.34. But for an isotropic fiber where the where the core and clad have indexes 1.4457 and 1.4378 respectively, V is 11.99. This demonstrates that more number of guided modes will exist in the nanoporous alumina fiber for these conditions and this number will change over changing the frequency. The number of guided modes will reduce at smaller frequencies.

The Fig. 4.7 shows the modal dispersions of the homogenepusly filled nanoporous alumina hollow waveguide embedded in air with air and silver metal inclusions. The modal dispersion of isotropic alumina fiber is also shown for comparison. We see that the change of the normalized β is very small compared to the case of an isotropic fiber. This hap-

Table 4.6: Guided mode conditions of a non-magnetic homogeneous anisotropic hollow circular waveguide. Where dielectric constant of core and outer region are $\varepsilon_1 = \varepsilon_3 = \varepsilon_i$. The index i for isotropic material.

Sr.	ε_r	ε_ϕ	ε_z	k_ν^2	k_τ^2	Conditions
1	+	+	+	$k_0^2\varepsilon_\phi - \beta^2$	$\frac{\varepsilon_z}{\varepsilon_r}(k_0^2\varepsilon_r - \beta^2)$	$\varepsilon_i < \beta^2/k_0^2 < \varepsilon_r$ $\varepsilon_i < \beta^2/k_0^2 < \varepsilon_\phi$
2	+	+	−	$k_0^2\varepsilon_\phi - \beta^2$	$\frac{-\lvert\varepsilon_z\rvert}{\varepsilon_r}(k_0^2\varepsilon_r - \beta^2)$	$\varepsilon_r < \beta^2/k_0^2$ $\varepsilon_i < \beta^2/k_0^2 < \varepsilon_\phi$
3	+	−	+	$-k_0^2\lvert\varepsilon_\phi\rvert - \beta^2$	$\frac{\varepsilon_z}{\varepsilon_r}(k_0^2\varepsilon_r - \beta^2)$	No guided mode
4	−	+	+	$k_0^2\varepsilon_\phi - \beta^2$	$\frac{\varepsilon_z}{\lvert\varepsilon_r\rvert}(k_0^2\lvert\varepsilon_r\rvert + \beta^2)$	$-\lvert\varepsilon_r\rvert < \beta^2/k_0^2$ $\varepsilon_i < \beta^2/k_0^2 < \varepsilon_\phi$
5	+	−	−	$-k_0^2\lvert\varepsilon_\phi\rvert - \beta^2$	$\frac{-\lvert\varepsilon_z\rvert}{\varepsilon_r}(k_0^2\varepsilon_r - \beta^2)$	No guided mode
6	−	+	−	$k_0^2\varepsilon_\phi - \beta^2$	$\frac{\lvert\varepsilon_z\rvert}{\lvert\varepsilon_r\rvert}(-k_0^2\lvert\varepsilon_r\rvert - \beta^2)$	No guided mode
7	−	−	+	$-k_0^2\lvert\varepsilon_\phi\rvert - \beta^2$	$\frac{\varepsilon_z}{\lvert\varepsilon_r\rvert}(k_0^2\lvert\varepsilon_r\rvert - \beta^2)$	No guided mode

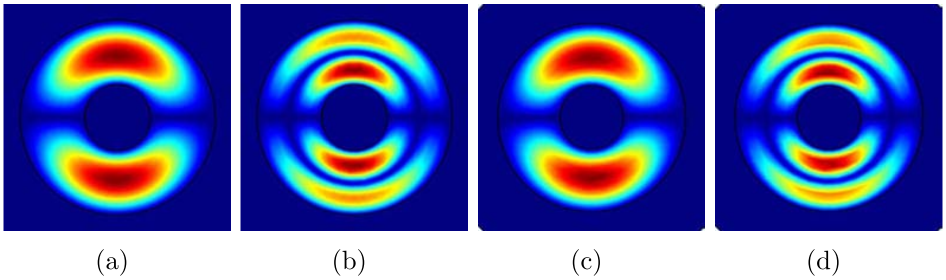
(a) (b) (c) (d)

Figure 4.8: The normalized mode plots of the homogeneously filled nanoporous alumina waveguide, when the nanopores are filled with air and silver, at wavelength 632.8 nm. (a) and (b) are modes for air inclusion, $\varepsilon_r = 2.638, \varepsilon_\phi = 2.467$. (c) and (d) are modes for silver inclusion, $\varepsilon_r = -1.288 + i0.053, \varepsilon_\phi = 6.244 + i0.027$. Here the core radius $R_1 = 5\mu$m and nanoporous alumina shell radius $R_2 = 15\mu$m.

pens because of the effective orders ν and τ of the Bessel functions for magnetic field and electric field become fractional and changes very slowly with increasing with azimuthal number m. Some plots of the modes in homogeneously filled anisotropic nanoporous alumina waveguide, when nanopores filled with air and silver nanowires at fill fraction 0.23, at wavelength 632.8 nm are shown in Fig. 4.8. For this example, the core ($r < R_1 = 5\mu$m) and outer region ($r > R_2 = 15\mu$m) of the homogeneous hollow anisotropic waveguide are assumed to be air. When the nanopores of anisotropic region are filled with air, then this is corresponds to Sr no. 1 of Table 4.6. Similarly, when the nanopores of anisotropic region are filled with silver nanowires, then this case is correspond to Sr. no. 4 of the Table 4.6. We see that the whole field is confined into the anisotropic region and in the core and outer region the field is almost zero.

4.5 Conclusions

We have presented a sample of the astonishing range of possibilities that arise with anisotropic metamaterial optical fibers. In this chapter, we have given a general mathematical description of nature of wave propagation in the anisotropic metamaterial fibers and numerically analyzed some practically possible examples of nanoporous alumina metamaterial fibers. These anisotropic metamaterial fibers support exotic modes described by Bessel and Neumann functions of fractional, imaginary and complex order, a rare physical application of these mathematical objects. A detailed analysis of the modes that are possible for the coaxial geometry under different kinds of anisotropies is presented. The conditions under which the modes are described by Bessel functions with imaginary orders or complex orders are investigated. These are shown to arise from hyperbolic dispersion in the medium. Many of the properties presented here are generic to circular waveguides with anisotropic metamaterial fillings and have wide ranging applications across the electromagnetic spectrum from the radio frequencies to optical frequencies. The nanoporous alumina microtubes with or without a central hollow core are presented as a physical manifestation of such an anisotropic metamaterial optical fiber. Here the guidance of the modes is entirely due to refractive effects and the condition for guided modes are analyzed. These metamaterial fibers with metallic inclusions exhibit electromagnetic losses by absorption and can not be used for communication purposes. But unique range of properties offered by them can be best utilized for sensing, coupling and other non-linear applications.

Chapter 5

Inhomogeneous, Anisotropic Metamaterial Optical Fiber

5.1 Introduction

The optical fibers or waveguides that have been homogeneously filled with an anisotropic dielectric material had been studied and used in various applications from several decades. In the step index fiber, the core and the clad are homogeneous. The inhomogeneous optical fibers have been less popular compared to homogeneous optical fibers [97,107,108]. This was presumably because of the difficulty in fabrication of the desired inhomogenious distribution of materials and the difficulty in predicting the properties as well. A quadratic inhomogeneous in permittivity optical fibers had been reported, which can be solved approximately in closed form [108,109]. Fibers with parabolic profile in the radial direction for the refractive index have been popular as they strongly localize the electromagnetic wave into the fiber. The FEM numerical technique is commonly used to solve such type of inhomogeneous problems [110–112]. An inhomogeneous fiber made of anisotropic liquid crystals with homogeneous material clad has also been reported [113]. In this liquid crystal fiber an angular inhomogeneity was present while the earlier fibers only have a radial inhomogeneity in the refractive index. After the invention of the photonic crystal, a few inhomogeneous photonic crystal fibers have been reported to support spatial soliton formation and to change the spectral properties of the fibers [114, 115].

In the previous Chapter 4, we presented the modal analysis of a homogeneously filled nanoporous alumina metamaterial coaxial fiber. In fact, the cylindrical nanoporous alumina is actually an inhomogeneous medium because of the varying nature of the size of the nanopores along the radial direction. In the previous chapter, we considered that the nanoporous alumina is homogeneous for simplicity and to understand the effects of the anisotropy only. Otherwise, we could not have distinguished the effects of inhomogeneity and anisotropy. In the present chapter, we shall discuss about the propagation of light and analyze the modes in inhomogeneous and anisotropic nanoporous alumina coaxial/hollow fiber. We shall see that in the inhomogeneous fiber, the electric and magnetic fields can not be decoupled and the modal solutions are not always amenable to analytic solutions. To study the waveguide properties of the inhomogeneous and anisotropic nanoporous alumina fiber, we carry out the analysis using the COMSOL Multiphysics simulations.

5.2 Inhomogeneous Nature of Cylindrical Nanoporous Alumina

We have seen in the previous Chapters 2 and 3, that the diameter of the nanopores and the azimuthal interpore distance in the cylindrical nanopores decrease towards the center of the fiber. Equation (3.9) shows that the nanopores fill fraction is a linear function of fiber radius which makes the cylindrical nanoporous alumina an inhomogeneous system. For a fixed radius of an aluminium microwire, the size of the nanopores and the interpore distance at the outer surface of the anodized wire can be changed by electrolyte, anodization voltage or current and solution temperature. Keeping the interpore distance fixed, the nanopores size even can be increased by pore widening. As we have seen in Chapter 2, at 40 V anodization of aluminium microwire in an iced cold 0.3 M oxalic acid solution gives average 30 nm nanopore diameter and average 100 nm interpore distance. Later

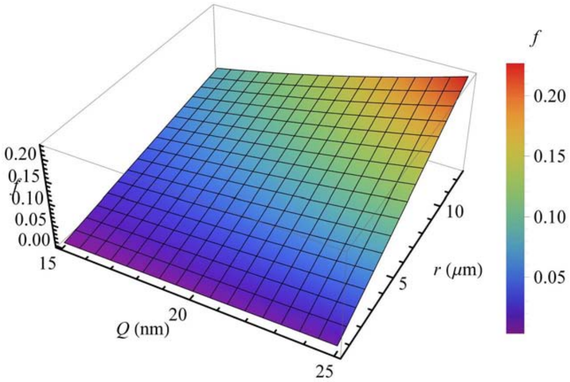

Figure 5.1: Plot of the fill fraction of nanopores of the cylindrical nanoporous alumina with microtube radius r and the diameter of the nanopores $2Q$ at the outer surface at R_2. Here interpore distance $D = 100$ nm, $R_1 = 0.5$ μm, $R_2 = 12.5$ μm.

on the nanopore diameters can be increased up to below the interpore distance by pore widening in dilute phosphoric acid. For a fixed interpore distance of 100 nm, the Fig. 5.1 show the plot of the nanopores fill fraction of the cylindrical nanoporous alumina with respect to the radius of the fiber and the nanopore diameter ($2Q$) at the outer surface. We see that for smaller nanopores diameter the variation of the fill fraction along the fiber radius is smaller and this variation increases for the bigger nanopore diameters, that is, the inhomogeneity and the anisotropy increase with the nanopores diameter.

The effective permittivity tensor components of the cylindrical nanoporous alumina are obtained in Eqs. (3.17), (3.18) and (3.19), by using the transformation optics technique and the Maxwell-Garnett homogenization theory. They have been plotted in Fig. 5.2 with respect to the radius of the fiber and frequency for the case of air inclusions and 50 nm nanopores diameter and 100 nm interpore distance. For lower frequency ranges, there is a resonance in the effective permittivity components ε_r and $\varepsilon_\phi = \varepsilon_z$ as shown in Figs. 5.2(a) and 5.2(b). But at visible range of frequencies, the ε_r and ε_ϕ are almost varying linear with the fiber radius at fixed frequency as shown in Figs. 5.2(c) and 5.2(d). Near the resonance, the anisotropy in the permittivity components is high and beyond the resonance the anisotropy is very small.

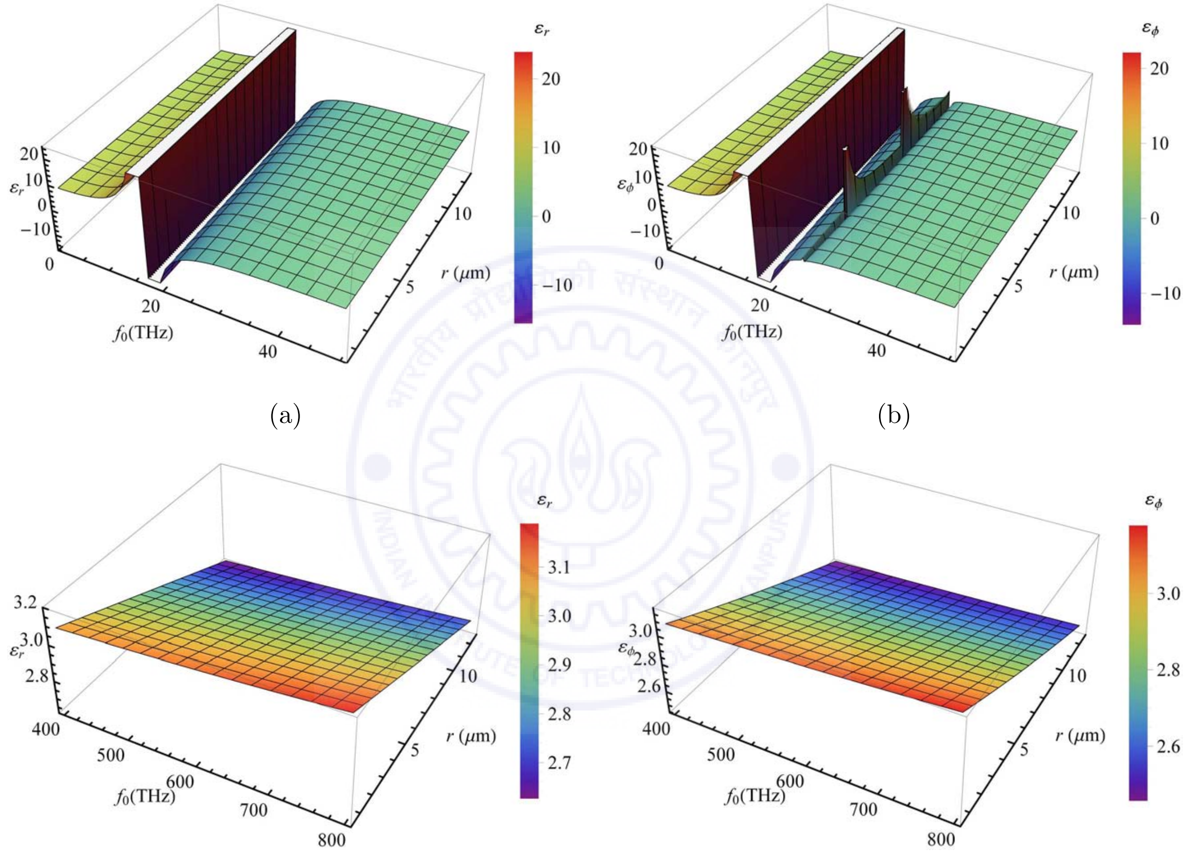

(a) (b)

(c) (d)

Figure 5.2: Plots of the effective permittivity components ε_r and ε_ϕ with frequency and radius of the fiber for $2Q = 50$ nm, $D = 100$ nm. (a) and (b) for 1 THz to 50 THz frequency range, (c) and (d) for the visible range.

5.3 Electromagnetic Fields in Inhomogeneous and Anisotropic Cylindrical Media

We have given the detailed mathematical modal analysis of homogeneously filled nanoporous alumina fiber in Chapter 4. The previous derivations have only the anisotropic effects. Since the cylindrical ananoporous alumina is inhomogeneous also, therefore, for investigating the waveguiding properties of the inhomogeneous and anisotopic cylindrical ananoporous alumina, we need to rederive the equations allowing for inhomogeneous material parameters.

Let us assume that the components of $\bar{\bar{\varepsilon}}$ and $\bar{\bar{\mu}}$ in Eqs. (4.1) are the functions of radius. For cylindrically symmetric inhomogeneous and anisotropic medium, putting E_r and E_ϕ from Eqs. (4.6a) and (4.6b) in the Eq. (4.5c), we get

$$\frac{\omega\mu_0}{r}\frac{\partial}{\partial r}\left(\frac{\mu_r}{q}r\frac{\partial H_z}{\partial r}\right)+\chi\frac{\beta}{r}\frac{\partial^2 E_z}{\partial r\partial\phi}+\frac{\omega\mu_0\mu_\phi}{p}\frac{1}{r^2}\frac{\partial^2 H_z}{\partial\phi^2}-\frac{\beta}{r}\frac{\partial}{\partial r}\left(\frac{1}{q}\right)\frac{\partial E_z}{\partial\phi}+\omega\mu_0\mu_z H_z=0. \tag{5.1}$$

Putting H_r and H_ϕ from Eqs. (4.6c) and (4.6d) in Eq. (4.2b), we get

$$\frac{\beta}{r}\frac{\partial}{\partial r}\left(\frac{\mu_r}{q}r\frac{\partial H_z}{\partial r}\right)+\chi_{\varepsilon\mu}\frac{\omega\varepsilon_0}{r}\frac{\partial^2 E_z}{\partial r\partial\phi}+\frac{\beta\mu_\phi}{p}\frac{1}{r^2}\frac{\partial^2 H_z}{\partial\phi^2}-\frac{\omega\varepsilon_0}{r}\frac{\partial}{\partial r}\left(\frac{\mu_r\varepsilon_\phi}{q}\right)\frac{\partial E_z}{\partial\phi}+\beta\mu_z H_z=0. \tag{5.2}$$

Putting H_r and H_ϕ from Eqs. (4.6c) and (4.6d) in Eq. (4.5f), we get

$$\frac{\omega\varepsilon_0}{r}\frac{\partial}{\partial r}\left(\frac{\varepsilon_r}{p}r\frac{\partial E_z}{\partial r}\right)+\chi\frac{\beta}{r}\frac{\partial^2 H_z}{\partial r\partial\phi}+\frac{\omega\varepsilon_0\varepsilon_\phi}{q}\frac{1}{r^2}\frac{\partial^2 E_z}{\partial\phi^2}+\frac{\beta}{r}\frac{\partial}{\partial r}\left(\frac{1}{p}\right)\frac{\partial H_z}{\partial\phi}+\omega\varepsilon_0\varepsilon_z E_z=0. \tag{5.3}$$

Putting E_r and E_ϕ from Eqs. (4.6a) and (4.6b) in the Eq. (4.2a), we get

$$\frac{\beta}{r}\frac{\partial}{\partial r}\left(\frac{\varepsilon_r}{p}r\frac{\partial E_z}{\partial r}\right)+\chi_{\varepsilon\mu}\frac{\omega\mu_0}{r}\frac{\partial^2 H_z}{\partial r\partial\phi}+\frac{\beta\varepsilon_\phi}{q}\frac{1}{r^2}\frac{\partial^2 E_z}{\partial\phi^2}+\frac{\omega\mu_0}{r}\frac{\partial}{\partial r}\left(\frac{\varepsilon_r\mu_\phi}{q}\right)\frac{\partial H_z}{\partial\phi}+\beta\varepsilon_z E_z=0. \tag{5.4}$$

In Eqs. (5.1), (5.2), (5.3) and (5.3), we have defined

$$p = k_0^2 \varepsilon_r \varepsilon_\phi - \beta^2, \quad q = k_0^2 \varepsilon_\phi \varepsilon_r - \beta^2, \tag{5.5a}$$

$$\chi = \left(\frac{1}{p} - \frac{1}{q}\right), \quad \chi_{\varepsilon\mu} = \left(\frac{\varepsilon_r \mu_\phi}{p} - \frac{\varepsilon_\phi \mu_r}{q}\right). \tag{5.5b}$$

Combing Eqs. (5.1) and (5.2), we get

$$\left(\frac{\beta\chi}{\omega\varepsilon_0} - \frac{\omega\mu_0\chi_{\varepsilon\mu}}{\beta}\right)\left[\frac{\mu_r}{q}\frac{1}{r}\frac{\partial}{\partial r}\left(r\frac{\partial H_z}{\partial r}\right) + \frac{\partial}{\partial r}\left(\frac{\mu_r}{q}\right)\frac{\partial H_z}{\partial r} + \frac{\mu_\phi}{p}\frac{1}{r^2}\frac{\partial^2 H_z}{\partial \phi^2} + \mu_z H_z\right]$$
$$+\frac{1}{r}\frac{\partial E_z}{\partial \phi}\left\{\chi_{\varepsilon\mu}\frac{\partial}{\partial r}\left(\frac{1}{q}\right) - \chi\frac{\partial}{\partial r}\left(\frac{\varepsilon_\phi \mu_r}{q}\right)\right\} = 0, \tag{5.6}$$

and combining Eqs. (5.3) and (5.4), we get

$$\left(\frac{\beta\chi}{\omega\mu_0} - \frac{\omega\varepsilon_0\chi_{\varepsilon\mu}}{\beta}\right)\left[\frac{\varepsilon_r}{p}\frac{1}{r}\frac{\partial}{\partial r}\left(r\frac{\partial E_z}{\partial r}\right) + \frac{\partial}{\partial r}\left(\frac{\varepsilon_r}{p}\right)\frac{\partial E_z}{\partial r} + \frac{\varepsilon_\phi}{q}\frac{1}{r^2}\frac{\partial^2 E_z}{\partial \phi^2} + \varepsilon_z E_z\right]$$
$$+\frac{1}{r}\frac{\partial H_z}{\partial \phi}\left\{\chi_{\varepsilon\mu}\frac{\partial}{\partial r}\left(\frac{1}{p}\right) - \chi\frac{\partial}{\partial r}\left(\frac{\mu_r \varepsilon_\phi}{p}\right)\right\} = 0. \tag{5.7}$$

We see in the Eqs. (5.6) and (5.7) that the second, fifth and sixth terms, which are spatial derivatives of the material parameters, are extra terms. It would be absent in a homogeneously filled fiber. For inhomogeneous fibers, in the differential equation of H_z (5.6), we have one extra E_z term and vice versa (5.7). So the equations for H_z and E_z can not be decoupled and hence the fields can not be decomposed into independent transverse modes, while in case of homogeneous fibers it can be nicely decomposed. It means there must exist the hybrid modes even if there is PEC boundary conditions in the case of the inhomogeneous and anisotropic waveguides or fibers. In a very coarse approximation, if we derive the modal equation for TE or TM modes separately putting E_z or H_z to zero in the inhomogeneous medium, the quantities within the square brackets of Eqs. (5.6) or (5.7) still exist and the differential equation can not be solved for the general variation of the permittivity components. There are only few cases such as quadratic variation of the permittivity can be solved analytically in an approximate manner [116]. To solve such type of problems, numerical methods such as the FEM analysis [110–112] are used. In the case of cylindrical nanoporous alumina the permittivity components vary with different effective functions in different frequency ranges. Therefore, for the case of cylindrical nanoporous alumina fiber, we have implemented FEM analysis using the COMSOL Multiphysics simulation software.

5.4 Modal Analysis of Inhomogeneous and Anisotropic Nanoporous Alumina Coaxial Fiber

After the anodization of aluminium microwire, there remains an aluminium core at the center of the nanoporous alumina shell. By coating a metal at the outer surface of the cylindrical nanoporous alumina, we can approximate this system as composed of PEC-nanoporous alumina shell-PEC regrows. These PEC conditions at the inside and the outside of the alumina relax the use of extra boundary conditions. It has another importance that it can be used as an inhomogeneous metamaterial fiber in the coaxial geometry. For the case of air inclusions in the nanopores of the cylindrical nanoporous alumina, the air and alumina are the constituent materials. We incorporate the nanopores fill fractions of Eq. (3.9), constituent material alumina[1] [1], effective permittivity components ε_r and ε_ϕ of Eqs. (3.17) and (3.18) directly into the COMSOL for the modal analysis.

The dispersion of the first few modes in an inhomogeneously filled anisotropic coaxial waveguide (nanoporous alumina) is shown in Fig. 5.3 for the particular case of 50 nm nanopore diameter and 100 nm interpore distance. For calculating the dispersion, the core radius R_1 is taken to be 0.5 μm and outer shell diameter R_2 is taken as 12.5 μm with PEC boundaries applied at R_1 and R_2. We chosen 50 nm nanopore diameter to

---

[1] For simplicity, we used the Sellmeier equation for alumina from Ref. Weber, Handbook of Optical Materials, 2003.

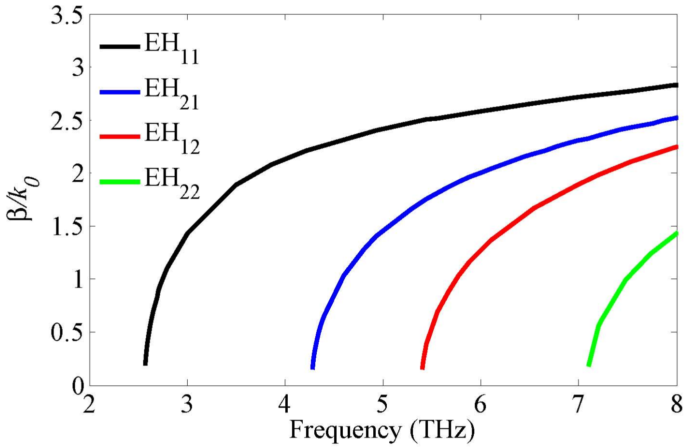

Figure 5.3: The modal dispersion plots for inhomogeneous and anisotropic cylindrical nanoporous alumina coaxial fiber obtained by the COMSOL simulation. The inner core radius $R_1 = 0.5\mu$m and the shell radius $R_2 = 12.5\mu$m. The nanopores diameter and inter-pore distance are 50 nm and 100 nm respectively at the outer surface of the nanopoorus alumina shell.

get sufficiently large anisotropy and inhomogeneity and at this nanopore diameter, the nanopore fill fraction is 0.23. So the Maxwell-Garnett homogenization is also valid. The dispersion will also change with change in these parameters. In Fig. 5.3, the dispersion of the are EH hybrid modes are shown. In the EH hybrid mode $|E_z| > |H_z|$ and in the HE hybrid mode $|E_z| < |H_z|$. We can see in the Eqs. (5.6) and (5.7) that there must exist hybrid modes even if there are PEC boundary conditions. We also found in the COMSOL numerical calculation that the zeroth order modes are pure TM modes. But the pure TE or TM modes are not obtained for the non-zero order modes. The cutoff frequencies of some EH hybrid modes are tabulated in Table 5.1 as obtained by the COMSOL numerical calculations.

Some plots of the modal fields in the inhomogeneous and anisotropic nanoporous alumina coaxial fiber at wavelength 632.8 nm are shown in Fig. 5.4 for the same parameters as was used for the calculation of the dispersion. We see that the light is highly concentrated near the center of the fiber in a very small volume even for the lower order modes also. We have seen in Chapter 4, that the anisotropy causes the more confinement

Table 5.1: The cutoff frequencies (in THz) of an inhomogeneous and anisotropic nanoporous alumina coaxial fiber. The cutoff frequencies were calculated for core and shell radius 0.5 μm and 12.5 μm. The nanopores diameter and interpore distance are 50 nm and 100 nm respectively at the outer surface of the nanoporus alumina shell.

Mode	f_c(THz)
EH$_{11}$	2.57
EH$_{12}$	5.40
EH$_{21}$	4.28
EH$_{22}$	7.10

of the light than the isotropic fiber, which could be seen clearly only for much higher modes. In the case of homogeneous anisotropic fiber, the lower order modes were spread over large volume but slightly more confined than the isotropic fiber. To confirm whether the extreme confinement is either due to inhomogeneity or a combination of inhomogeneity and anisotropy, the modal field plots in inhomogeneous and isotropic fibers are also shown in Fig. 5.4 where the dielectric permittivity is inhomogeneous with the same radial dependence but is isotropic with $\varepsilon = \varepsilon_r$ in case of rows 3 and 4 in Fig. 5.4 or $\varepsilon = \varepsilon_\phi$ in case of rows 5 and 6 in Fig. 5.4. We conclude from these diagrams that the extreme confinement is principally happening because of the inhomogeneity and the anisotropy only accentuates it, in the nanoporous alumina fiber. The field plot of Fig. 5.4 is only for a particular case and parameters. If we increase the inhomogeneity by increasing the nanopores diameter by pore widening while keeping the other geometrical parameters same then the confinement of light also increases. This is a very good thing about the cylindrical nanoporous alumina fiber because we can tune its properties very easily. The dispersion and the confinement behavior can be flexibly changed by filling the nanopores of the cylindrical nanoporous alumina by suitable materials.

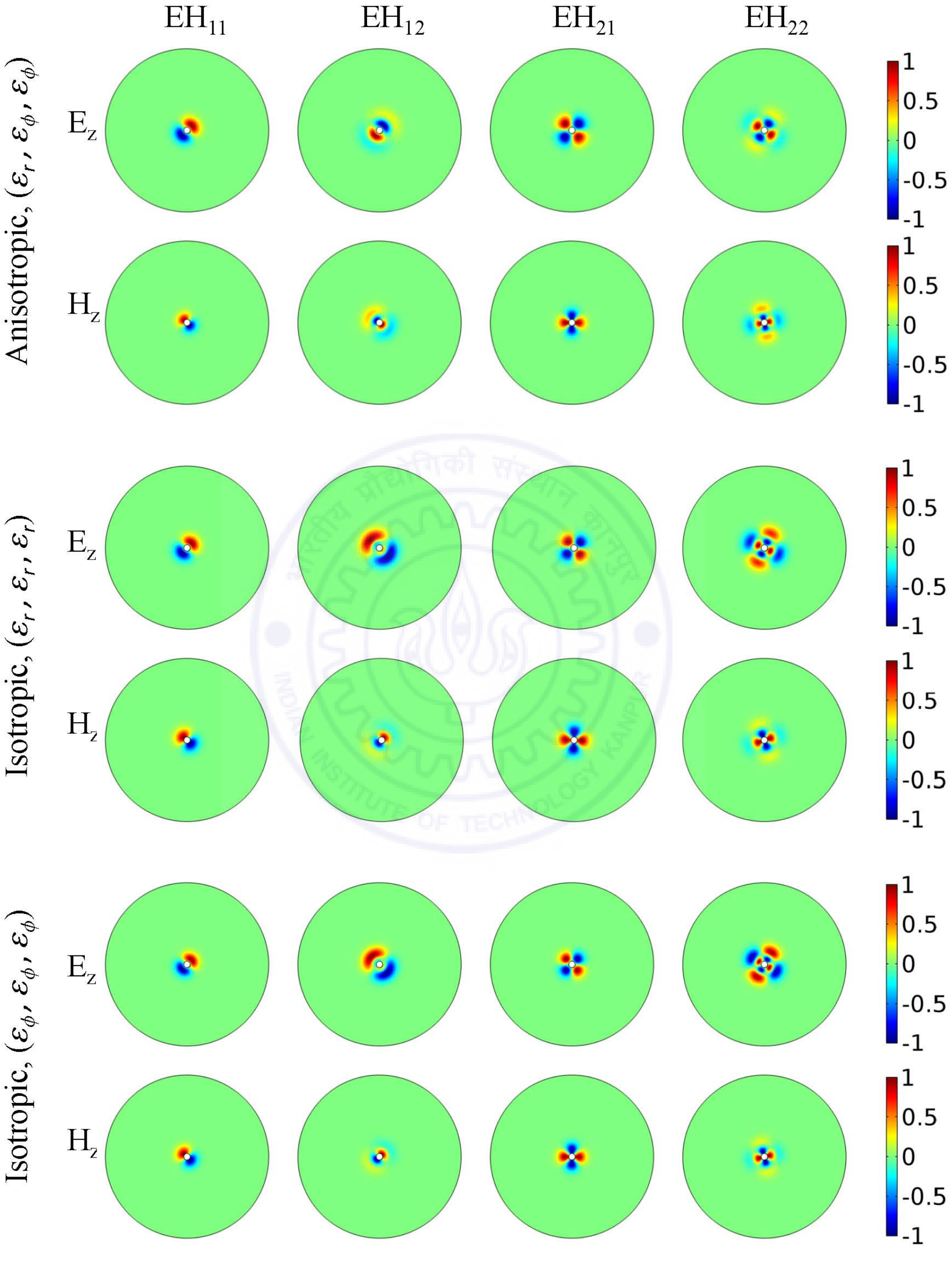

Figure 5.4: The COMSOL simulated field plots of some hybrid modes of nanoporous alumina fiber for air inclusion at wavelength $\lambda = 632.8$ nm, the inner core radius $R_1 = 0.5\mu$m and the shell radius $R_2 = 12.5\mu$m. The inner and outer boundaries are PEC. Here there exist only EH hybrid modes. Rows 1 and 2 for inhomogeneous and anisotropic fiber, and rows 3 to 6 for inhomogeneous and isotropic fiber.

5.5 Guided Modes in the Inhomogeneous and Anisotropic Nanoporous Alumina Fiber

In this section, we consider the most realistic case where the nanoporous alumina fiber refractively guides the modes by itself. The aluminium core presence will necessarily be dissipative although we approximately we have modeled it as a PEC. Here we remove that requirement as well. Let us consider that the core ($r < R_1$) and the outer region ($r > R_2$) of the inhomogeneous and anisotropic nanoporous alumina fiber are filled with the air. Since the both regions 1 and 3 have the same material, therefore, the nature of the field will be same either decaying or oscillating in both of them. For the guided field in the region 2 that is the inhomogeneous and anisotropic region, the electric and magnetic fields are the solutions of the Eqs. (5.7) and (5.6) respectively, and the field in the region 1 and 3 will be decaying with increasing radial distance. Since the region 2 is inhomogeneous and can not be treated analytically, therefore, the guided modes for this inhomogeneous and anisotropic nanoporous alumina fiber have been simulated by the COMSOL multiphysics software.

Some modal field plots of the guided modes in the inhomogeneous and anisotropic nanoporous alumina fiber with for inclusion are shown in Fig. 5.5. For comparison, modal field plots of inhomogeneous and isotropic fiber are also shown in Fig. 5.5 in rows 3 to 6. We see that here too there exist only the hybrid modes for non-zero m values and the fields are concentrated towards the inwards side in the region 2. The modal dispersions of the inhomogeneous and anisotropic nanoporous alumina hollow fiber for air inclusion are shown in the Fig. 5.6. It is very difficult to obtain the effective β value at near the cutoff frequencies, therefore, the cutoff frequencies could not be found.

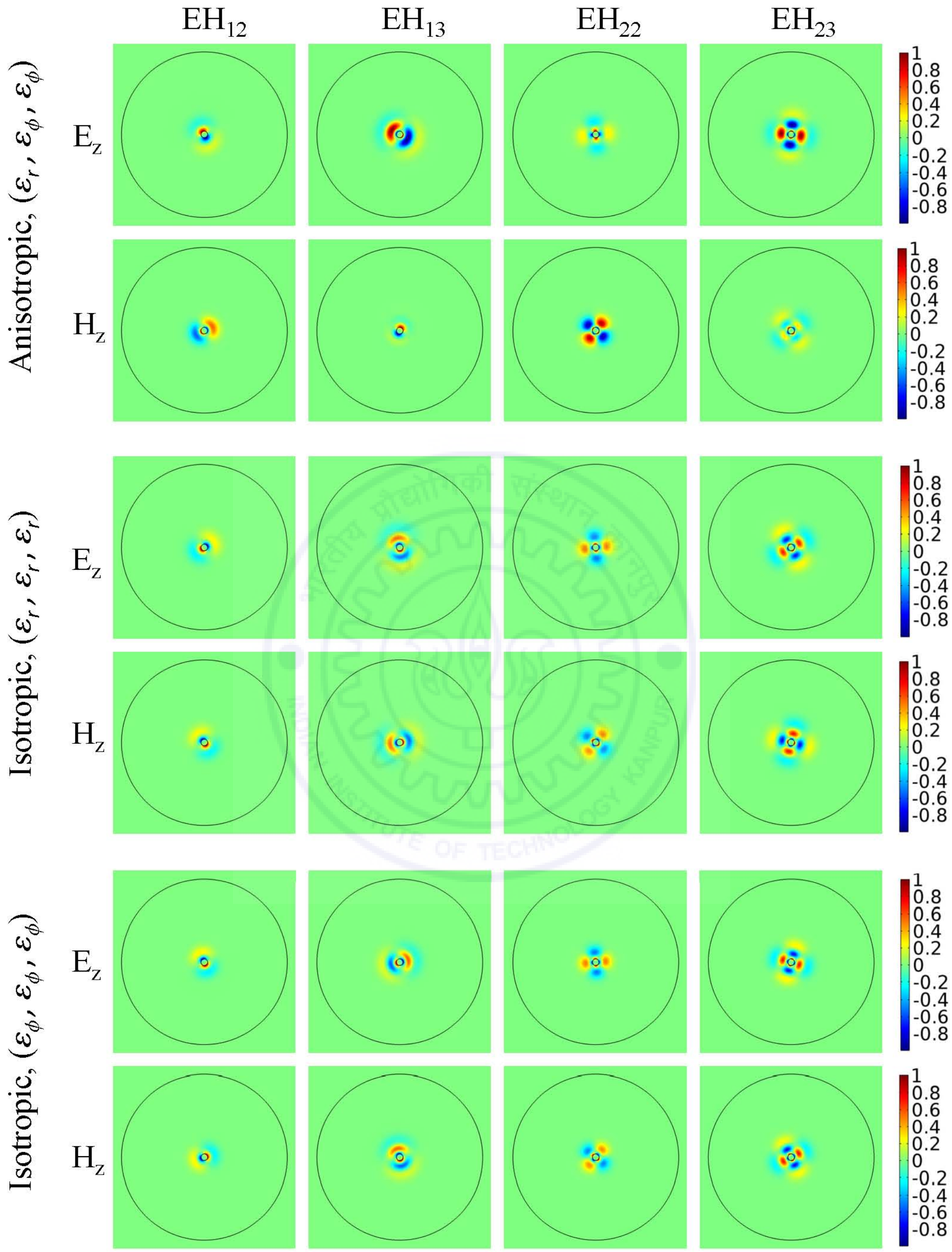

Figure 5.5: The COMSOL simulated field plots of some guided modes of nanoporous alumina fiber for air inclusion at wavelength $\lambda = 632.8$ nm, the inner core radius $R_1 = 0.5\mu$m and the shell radius $R_2 = 12.5\mu$m. Here the core and the outer regions are filled with air. The nanopores diameter and interpore distance are 50 nm and 100 nm respectively at the outer surface of the nanopoorus alumina shell. Modal field plots for inhomogeneous and anisotropic fiber are in rows 1 and 2, and for inhomogeneous and isotropic fiber are in rows 3 to 6.

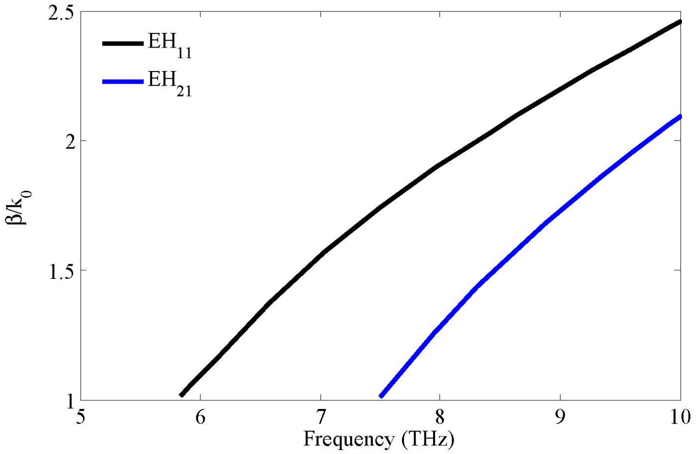

Figure 5.6: The modal dispersion plots for inhomogeneous and anisotropic cylindrical nanoporous alumina hollow fiber obtained by the COMSOL simulation. The inner core radius $R_1 = 0.5\mu$m and the shell radius $R_2 = 12.5\mu$m. The nanopores diameter and inter-pore distance are 50 nm and 100 nm respectively at the outer surface of the nanopoorus alumina shell.

5.6 Optical Charaterization of Inhomogeneous Anisotropic Nanoporous Alumina Fiber

Crystalline alumina is very transparent for a wide range of the visible frequencies. The crystal nature and optical characteristic of the anodized alumina depend on the growth conditions [117, 118]. We have seen in the Chapter 2 that anodizing a very high purity aluminium sheet or microwire in a ice cold 0.3 M oxalic acid at 40 V yields an optically transparent nanoporous alumina. But it does exhibit some scattering which depends on the wavelength because of the structured nature. In a sense this scattering due to the nano structure will be almost fundamental. Here we shall present some optical measurement on the cylindrical nanoporous alumina fiber. The cylindrical nanoporous alumina also is very brittle and its end can not be cleaved very clearly to leave a sharp interface. We have just bent the fiber to break it to obtain proper end facets that are roughly flat. If the cleaved edges are not extremely sharp then the mode characterization can not be done.

To characterize the nanoporous alumina fiber we only carried out some preliminary optical transmission experiments. A slightly bent cylindrical nanoporous alumina fiber of length 1.3 cm and diameter 80 μm with aluminium core of diameter 10 μm was used. The length of the fiber was kept short because for longer fiber lengths, the output would be lost by scattering. Some photographs of the fiber scattering and laser transmission output through the fiber are shown in Fig. 5.7. 532 nm green laser used to see the light scattering, while the transmission from the nanoporous alumina was examined with a 632.8 nm He-Ne laser. As stated before the nanoporous alumina fiber was intentionally bent slightly to distinguish the transmitted light from the uncoupled incident light. This bending of nanoporous alumina fiber was obtained by bending the aluminium micro wire prior to anodization as the nanoporous alumina was very delicate and it could not be bent after the anodizing a straight aluminium micro wire. We see that the light follows along the fiber with large amount of scattering. This scattering is primarily due to the large level of imperfections in the structure of the fiber, apart from the Rayleigh-like scattering from the nanostructure. This scattering can be minimized by reducing the nanopores diameters or using light of longer wavelength. The smaller nanopores, in general, can be obtained by anodizing aluminium microwire at low voltage. The anodization in sulfuric acid can also reduce the nanopore size substantially. For the present, we believe that the chemical synthesis process for the nanoporous alumina will have to be significantly improved and optimized to yield high quality fibers. Figure 5.7(b) shows the output of the nanoporous alumina fiber with 632.8 nm wavelength of He-Ne laser light. We chosen this wavelength because it is easily available and have longer wavelength also in the visible range, for which scattering would be lower and we would get more intensity in the output. Since the nanoporous alumina fiber was slightly bent, the direct laser light spot and the output of the fiber can be spatially separated and simultaneously photographed. We see that the nanoporous alumina fiber output is much concentrated than the direct laser output. We have seen in the previous section of this chapter that light in the modal field plots of nanoporous alumina fiber was concentrated near to the center of the fiber.

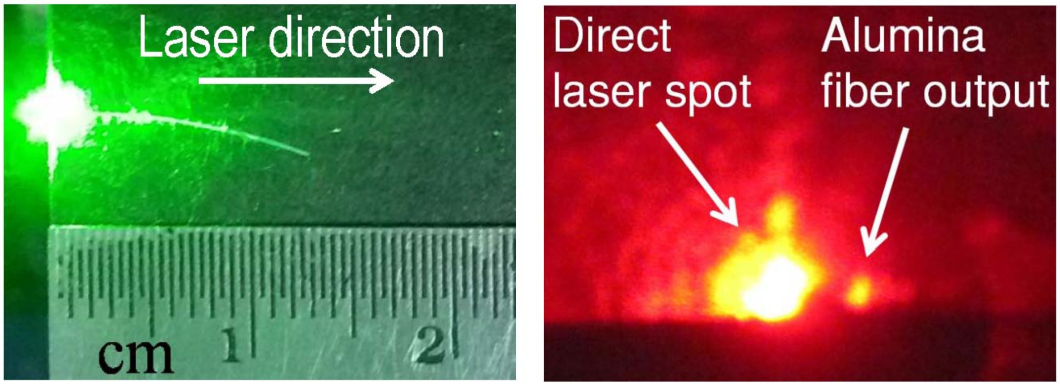

(a) (b)

Figure 5.7: (a) Photograph of light ($\lambda = 532$ nm) propagating across a bent nanoporous alumina fiber with an aluminum core, aluminium core diameter- 10 μm, nanoporous alumina shell diameter- 80 μm, length- 1.3 cm, nanopore diameter is 30 nm and nanopore periodicity is 100 nm at outer surface. The scale bar is shown for scale. (b) The output from the nanoporous alumina fiber at $\lambda = 632.8$ nm wavelength.

But in the experiment the fiber modes could not be resolved because the cleaved edges of the nanoporous alumina fiber were not sharp and we could only see the output light without any features. If the nanoporous alumina fiber can be cleaved sharply, then it would probably permit a mode analysis can be done.

5.7 Conclusions

We presented the cylindrical nanoporous alumina as an inhomogenesously filled anisotropic waveguide or fiber because of variation of the nanopore size with the radial distance in the volume of the fiber. In the visible frequency range, the approximately linear variation of the effective permiitivity components of the fiber with respect to the radius does not easily permit the analytic solution for the modes in the fiber, particularly in closed form. From the differential equation, we perceive that there must exist hybrid modes even for PEC boundary conditions, which are not possible in the conventional isotropic optical fibers. To carry out the modal analysis, we implemented the FEM using COMSOL Multiphysics software on the nanoporous alumina fiber. We have shown by simulations that the nanoporous alumina fiber has highly localized modes and the light near the center of the fiber. We have examined the modal fields and the dispersions of the modes for two kinds of boundary conditions: (i) when there are PEC at the central and the exterior of the anisotropic medium and (ii) when the anisotropic medium has air on both sides and the modes are entirely refractively guided.

The nanoporous alumina fiber synthesized was very brittle so it could not be cleaved sharply, but it was bent by using aluminium microwire bent prior to anodization. We shown the transmission of light through the nanoporous alumina fiber experimentally using light of visible frequency range. The fiber was found to exhibit high level of scattering presumably due to the imperfections and cracks in the structure. The output from the nanoporous alumina fiber was very highly localize focused than the direct laser output. The nanoporous alumina fiber is also expected to highly scatter light due to the nanostructure. These fibers may not be suitable for tele-communications purpose because of their scattering properties due to the nanostructured nature. But they could be excellent materials for use in the sensing, coupling and nonlinear application.

Chapter 6

Fluorescence from molecules on, and Scattering from Nanoporous Alumina

6.1 Introduction

The optical properties and applications of planar nanoporous alumina have been widely investigated in the literature [43,119–122]. The birefringent property of nanoporous alumina has been reported [119]. The optical properties of planar nanoporous alumina embedded with nanowires have also been investigated [120]. Chemical transport detection, medical applications and quantum dot confinement had been studied in nanoporous alumina using fluorescence [123–126]. All the mentioned studies have been carried out using planar nanoporous alumina with hexagonal arrangement of the nanopores, but the optical properties of planar nanoporous alumina with anisotropically organized nanopores was not known. Some nanoporous alumina coated microtubes with large diameters were proposed for use as catalyst in hydrocarbon conversion [65] and as a catalyst in the formation of ammonia [66]. Hence it would be very interesting to investigate the optical properties of nanoporous alumina in the cylindrical geometry, which is a new system developed by us.

In the Chapter 2, we have shown the fabrication of planar nanoporous alumina with hexagonal, random and linear arrangement of the nanopores and the cylindrical nanoporous alumina. We have also shown the electrodeposition of the silver nanowires in the nanopores of the planar as well as cylindrical nanoporous alumina. In this chapter, we shall show that how the linear arrangement of the nanopores in planar nanoporous alumina affects the fluorescence from Rhodamine-6G (R6G)dye and scattering from gold coated planar nanoporous alumina. We shall see that the planar nanoporous alumina with linearly organized nanopores show the polarization dependent scattering of light. In the cylindrical geometry, we shall investigate how the silver nanowires grown in the nanopores of a cylindrical nanoporous alumina microtube affects the darkfield and bright-field scattering. If the nanopores of the cylindrical nanoporous alumina is filled with R6G, then how will the fluorescence from molecules deposited on the alumina be affected. First we shall discuss the radiation and scattering in the planar geometry and then in the cylindrical geometry.

6.2 Fluorescence and Scattering from Planar Nanoporous Alumina

6.2.1 Sample Fabrication

The planar nanoporous alumina were used as templates to study the darkfield spectra and fluorescence of active probe molecules such as R6G deposited on the templates. To make the nanoporous alumina plasmonically active, we deposited 25 nm thick gold film by thermal evaporation onto these templates prior to the deposition of fluorescent molecules. The R6G dissolved in polymethylmethacrylate (R6G+PMMA) at a concentration of 50 μM was spin coated at 3000 rpm on to these gold coated templates.

Surface morphology and the porous nature of the prepared aluminium sheet and planar nanoporous alumina were investigated by a field emission scanning electron mi-

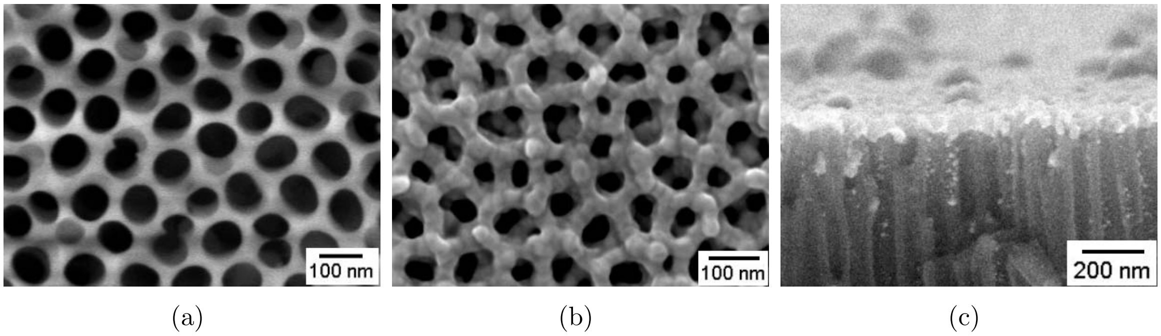

(a) (b) (c)

Figure 6.1: FESEM images of the front surface of planar nanoporous alumina: (a) before and (b) after the deposition of a 25 nm thick Au film. Image (c) is the cross sectional image of the Au-coated planar nanoporous alumina showing the pores and the top gold coating.

croscope (FESEM: Zeiss Supra 40VP). The optical properties of the prepared samples were studied by an optical polarizing microscope Olympus BX51 in the brightfield and the darkfield illumination modes. The fluorescence was measured by Olympus BX51 fluorescence microscope through a 100X objective. The wavelength bands 488 nm (blue) and 548 nm (green) with FWHM of 23 nm and 5 nm respectively were used as excitation sources and appropriate filters were used to reject the excitation light for the collection of the fluorescence spectra. The spectra were measured by an Ocean Optics HR2000 spectrometer connected to the trinocular part of the micoscope by an optical fiber.

6.2.2 Morphology of Linearly Organized Nanopores

Figure 6.1(a) and Fig. 6.1(b) show the FESEM images of a bare planar nanoporous alumina and a planar nanoporous alumina with a 25 nm thick gold film deposited by thermal evaporation process. The planar nanoporous alumina in both cases has randomly oriented pores. In Fig. 6.1(c) the cross section of the gold coated planar nanoporous alumina is shown. We see that the gold primarily gets deposited on the bridges between the pores and may partially cover the holes. The gold does not appear to coat inner surface of the pore walls except for about 25 nm from the surface of the planar nanoporous alumina. Thus we end up with a network of thin metallic bridges that span the surface of the planar nanoporous alumina. Such thin bridge metallic structures are known to support strongly localized electromagnetic modes [127]. In the sequel, we would examine plasmonic properties of such materials.

6.2.3 Darkfield Spectroscopy

Broadband white light scattering from the alumina surfaces was studied using white light reflection in the brightfield and darkfield modes. Primarily reflected light at small scattering angles including a strong specular component is obtained with bright field illumination, while light scattered at large angles are detected with darkfield illumination where light is incident on the sample from large oblique angles through a darkfield condenser lens. Darkfield optical microscope spectroscopy is known to yield a wealth of information about localized plasmonic resonances of metallic nanostructures [128, 129]. The polarization of the incident light was adjusted to be such that the electric field of radiation was either parallel to the direction of linearly aligned pores (parallel polarization) or perpendicular to the direction of linearly aligned pores (perpendicular polarization). We had used linearly organized planar nanoporous alumina and randomly ordered planar nanoporous alumina for the study unless otherwise stated.

The scattering spectra from the darkfield images and the reflection spectra from the bright field images are shown in the Figs. 6.2(a), 6.2(b) and Figs. 6.2(c), 6.2(d) respectively. It was observed that in the case of scattering spectra the signal was large only for incident light with parallel polarization compared to incident light with perpendicular polarization. The scattered light spectra for the cases of linearly organized pores without gold coating were seen to be low for either polarization of incident light. Interestingly, a similar trend of low scattered light was seen for the cases of randomly oriented pores with and without gold coating.

Comparatively, the reflection spectra obtained from the planar nanoporous alumina

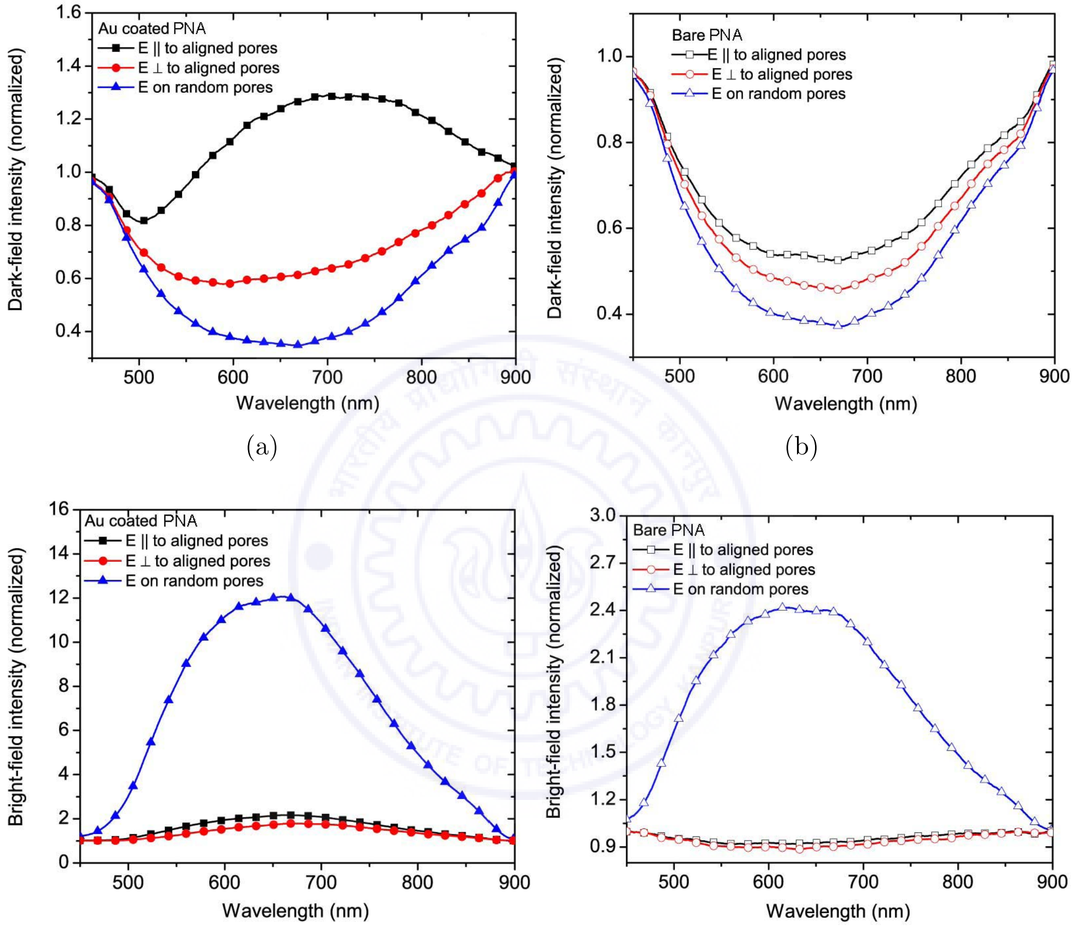

(a) (b)

(c) (d)

Figure 6.2: The large-angle scattering and reflectivity spectra obtained by darkfield and brightfield microscopic measurements. (a) The darkfield (scattering) spectra when the planar nanoporous alumina (PNA) is coated with 25 nm thick gold film, (b) the darkfield (scattering) spectra from bare PNA, (c) the brightfield (reflection) spectra when the PNA is coated with 25 nm thick gold film and (d) the brightfield spectra (reflection) from the bare PNA.

(brightfield mode) was quite different from the scattering spectra for both the polarizations. The reflectivity obtained from the linearly organized porous alumina templates with and without gold coatings have similar spectral characteristics as shown in Figs. 6.2(c), 6.2(d). The light scattering from the randomly oriented porous alumina templates without gold coating was also seen to be similar except for the case of gold coated random planar nanoporous alumina when the reflectivity is relatively strong (Fig. 6.2(a)). The polarization of the incident light in all these cases causes only marginal differences to the reflectivity of the samples.

It should be noted that while there are not much differences with respect to the polarization for the reflection spectra, the electric field direction of the incident light with respect to the lines of the nanopores plays a significant role in the darkfield scattering spectrum. We also note that there was significant disorder in the positioning of the nanopores along the lines and also in the line spacing. Differences in the back scattering of light from random gratings of metal or dielectrics for different polarizations had been well studied [130–134]. These random gratings consist of randomly modulated surfaces with some average spacing that can be defined for the spacing and the randomness is characterized by the extent of deviations from this average spacing. Enhanced back scattering was reported for shallow metallic random gratings for electric field of incident light polarized perpendicular to the gratings (p-polarized [130, 132]), while enhanced backscattering was reported for incident light with electric field parallel to the gratings (s-polarized [130,133]), only for deep metallic gratings. Further, the surface plasmon excitation mechanism was dominant for the perpendicular polarization (p-polarization [133]). In our case, the gold coated planar nanoporous alumina could be envisaged as network of thin metallic bridges as seen from the SEM images. Hence, the gold coated planar nanoporous alumina with the linearly organized pores along the scratch lines could essentially be considered to be shallow metallic random gratings. There was additional sub-wavelength structuring along the line due to the presence of the pores. We noted that the lines of pores themselves were not of sub-wavelength size or spacing, as they were organized by the scratches of larger thickness.

The bright field reflection data indicate that the enhanced specular backscattering was comparable in both cases of polarization for the incident light. The dark field scattering spectra indicate that a large angle scattering predominates for parallel polarized light compared to perpendicular polarized light. This implies that a large band of plasmonic resonances are excited, over the wavelength band of 600-800 nm. The disorder in the structure produces localized surface plasmon resonances at a variety of wavelengths. Our observation was in contrast to the reports by Maradudin et al. [130,131] with smooth grating lines, where large plasmonic excitation and scattering enhancements were obtained for incident light polarized perpendicular to the lines (p-polarization). This difference probably arises from the excitation of local surface plasmon (LSP) on the holes along the lines in our case. It is also noted from Fig. 2.4 that the inter pore distance along the lines is smaller than the inter pore distance perpendicular to the lines (line spacings). The reduced distance between the pores along the lines would facilitate the interactions of LSP on the holes within a line. Detailed computer simulations of the 2D structured random gratings would be required to study these aspects.

6.2.4 Fluorescence Spectroscopy

Fluorescence spectra obtained from R6G deposited on the planar nanoporous alumina templates were excited by either using blue light or green light as explained in the previous section and the fluorescence measured is shown in Fig. 6.3. It was noted that large fluorescence was obtained from the R6G molecules deposited on bare planar nanoporous alumina surfaces with no gold coating. This large fluorescence from the planar nanoporous alumina surfaces compared to the fluorescence from molecules on plain glass surface was clearly due to the multiple scattering of both the excitation and fluorescence light within the planar nanoporous alumina. The excitation light was thereby confined vicinity of the absorbing molecules by multiple scattering in a manner akin to that of random lasers [135].

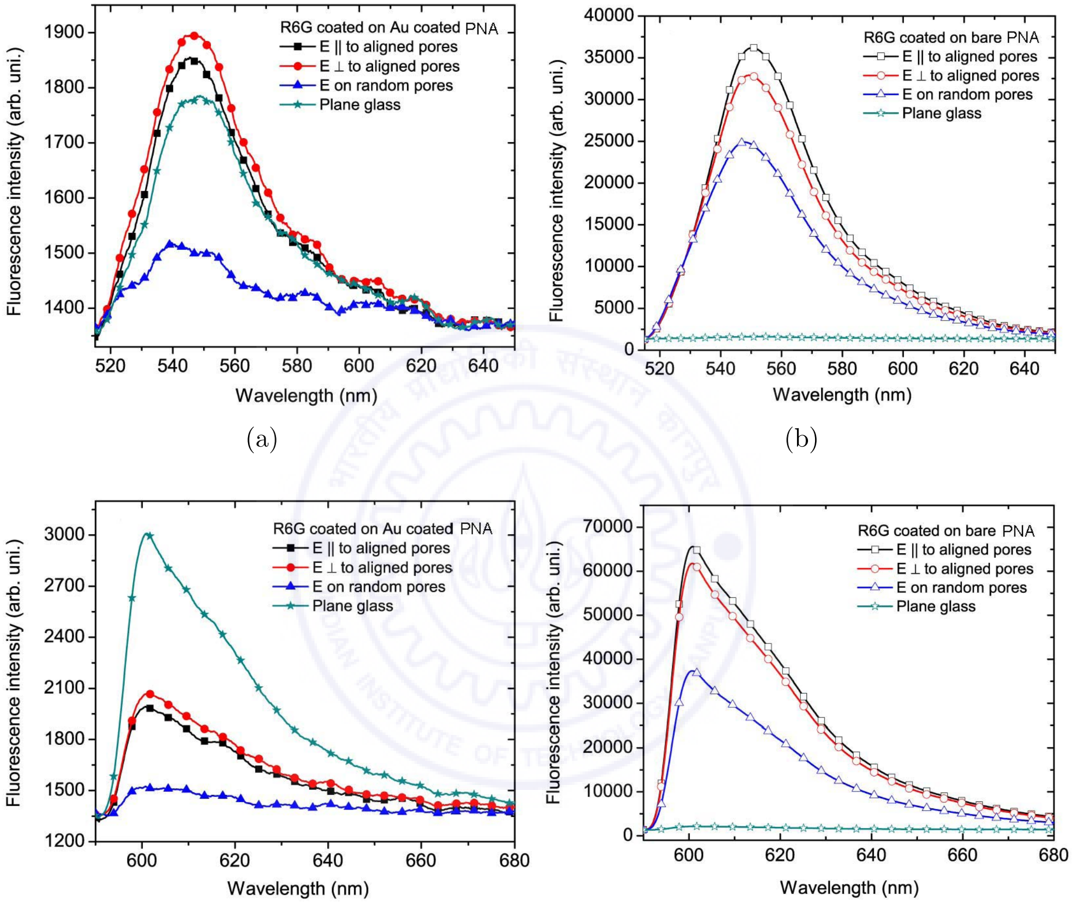

(a) (b)

(c) (d)

Figure 6.3: Fluorescence spectra obtained from R6G doped PMMA spin coated on the planar nanoporous alumina (PNA) with and without gold coating using (a and b) 488 nm and (c and d) 548 nm wavelength excitations. (a) Fluorescence spectra when R6G coated on Au-coated PNA, (b) fluorescence spectra when R6G coated on bare PNA, (c) fluorescence spectra when R6G coated on Au coated PNA and (d) fluorescence spectra when R6G coated on bare PNA.

Further, all the fluorescent light was scattered backwards in contrast to the molecules on a glass slide where the fluorescent light was also emitted in the forward directions. The fluorescence from molecules on anisotropic planar nanoporous alumina surfaces with linear organization was higher than the fluorescence from molecules on the randomly oriented nanoporous planar nanoporous alumina surfaces. Further, the fluorescence emitted by the molecules on the anisotropic planar nanoporous alumina surfaces show a marginal but consistent dependence on the orientation of polarization of the incident light with respect to the linear rows of the pores. The fluorescence was higher when the excitation light was polarized parallel to the rows of the nanopores. The more effective scattering as measured in the darkfield spectra (Fig. 6.3) for the case of excitation light polarized parallel to the linear rows of nanopores possibly gives rise to the higher fluorescence in this case. It should be emphasized that the above effects are observable with both blue and green excitations.

When molecules were deposited on the gold coated planar nanoporous alumina surfaces that are plasmonically active a strong quenching of the fluorescence (about 20 times lower) was seen. This results from the large coupling of the excited dye molecules to the localized near-fields of the surface plasmons whereby the energy was coupled into free space modes. Quenching of the fluorescence was well known [136–138], but such a quenching that was independent of the excitation wavelength is probably due to the random nature of the plasmonic surface that enables coupling to a variety of surface plasmon modes at any emission wavelength. Comparatively, molecules on lithographically fabricated ordered gratings can show excitation wavelength dependent enhancements of the fluorescence as the excited molecules can couple their energy into surface plasmon modes only when available [139].

6.3 Fluorescence and Scattering from Cylindrical Nanoporous Alumina

6.3.1 Sample Fabrication

The electrodeposition of silver nanowires into the nanopores of the cylindrical nanoporous alumina have been described in Chapter 2. Here we describe the effects of doping Rhodamine-6G (R6G) molecules into the nanopores of the cylindrical nanoporous alumina.

After the anodization of electropolished aluminium micro wire and electrodeposion of silver nanowires in the anodized aluminium wire were properly dried. We made a 50 μM solution of R6G by dissolving it in benzene chloride. The R6G solution was properly stirred to mix it well so that aggregates are avoided while doping in to the nanopores of alumina. The dried samples were immersed into the R6G solution. While sample were immersed, after each 30 minutes interval the solutions was shaken to remove some micro size air bubbles that emanated from the nanoporous microtube. After two hours the samples were taken out from the R6G solution and dried in air at room temperature for optical studies. A schematic of the R6G doped anodized wire is shown in Fig. 6.4(a). A photograph of the R6G doped anodized wire exited by 548 nm wavelength light is shown in Fig. 6.4(b). The anodized wire diameter was 70 μm.

6.3.2 Darkfield Spectroscopy of Nanowire Embedded Cylindrical Nanoporous Alumina

The darkfield and brightfield of cylindrical nanoporous alumina with and without silver nanowires were studied by a Olympus BX51 optical microscope. The spectra were recorded by Ocean Optics HR2000 connected to the trinocular port optical microscope by an optical fiber. Figure 6.5 show the dark and bright filed spectra of silver nanowire deposited cylindrical nanoporous alumina and a bare cylindrical nanoporous alumina for

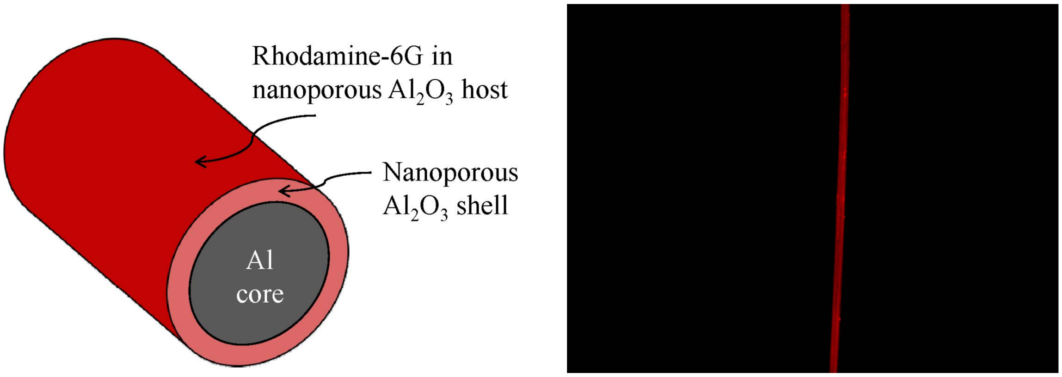

(a) (b)

Figure 6.4: (a) Schematic of R6G doped nanoporous alumina shell and (b) Fluorescence photograph of R6G coated nanoporous alumina shell excited by 548 nm wavelength light. The diameter of the anodized wire was 70 μm.

comparison. The dark and bright field spectrum were normalized with an electropolished aluminium micro wire. The reason of using the cylindrical references is that we wanted to compare the scattering and fluorescence enhancement from the same geometry but it can also be compared with flat references. As in Fig. 6.5(a) the bare alumina shows less scattering in the darkfield mode. While the silver nanowire deposited shows much higher level of scattering more than the electropolished aluminium micro wire due to an increased rough surface and, perhaps, surface plasmon resonances on the silver nanowires. The nanoporous alumina shell thickness is very small and after the electrodeposition of nanopores some amount of silver also gets deposited on the outer surface of the anodized wire and the outer surface becomes very rough as shown in Figs. 6.5(c) and 6.5(d). The deposition of silver on the outer surface is because of the non-uniform deposition process and could not be controlled by several methods tried by us. So in attempting to fill the nanopores completely, some amount of silver gets deposited on the outer surface of the cylindrical nanoporous alumina. This roughness could not be removed because the anodized wire had sub-hundred μm diameter and was extremely delicate precluding mechanical cleaning methods. Some other non-contact techniques such as chemical or ion beam cleaning methods can be used. In the darkfield spectra of Fig. 6.5(a), there is small dip in the nanowire embedded cylindrical nanoporous alumina which is presumably due to the surface plasmon of nanowire mdedia while the bare cylindrical nanoporous alumina does not show this resonance. The resonance appears highly broadened and inhomogeneity seems rather large. An optical photograph of the light scattering in darkfield mode from the surface of cylindrical nanoporous alumina with and without silver nanowire is shown in Fig. 6.5(c). We see that the nanowire deposited cylindrical nanoporous alumina is highly scattering comparatively.

In the case of the brightfield measurements, the situation is just opposite compared to the darkfield mode case. As Fig. 6.5(b) shows that in the brightfield mode, the scattering of bare cylindrical nanoporous alumina is approximately same as the electropolished aluminium micro wire while the silver nanowire embedded cylindrical nanoporous alumina is less scattering compare to the electropolished aluminium micro wire. An optical photograph of samples in the brightfield mode is shown in Fig. 6.5(d). We see that the in this case, the silver nanowire embedded cylindrical nanoporous alumina appear much darker than the bare cylindrical nanoporous alumina. This is due to the large absorption of light that happens due to the silver nanowires.

6.3.3 Fluorescence from Rhodamine-6G coated Cylindrical Nanoporous Alumina

To study the fluorescence properties of the R6G coated cylindrical nanoporous alumina two wavelengths 488 nm and 548 nm of light were used as excitation sources, which had full-width and half-maxima (FWHM) of 23 and 5 nm, respectively. For the collection of fluorescence signals, appropriate filters were used to cut-off the excitation light and pass the fluorescence light only. The fluorescence spectra are shown in Fig. 6.6. The obtained fluorescence spectra of samples as obtained by excitation wavelengths 488 nm (blue light) (Fig. 6.6(a)) and 548 nm (green light) (Fig. 6.6(b)) have similar characteristics, but a large difference in the amplitudes because the fluorescence efficiency fro

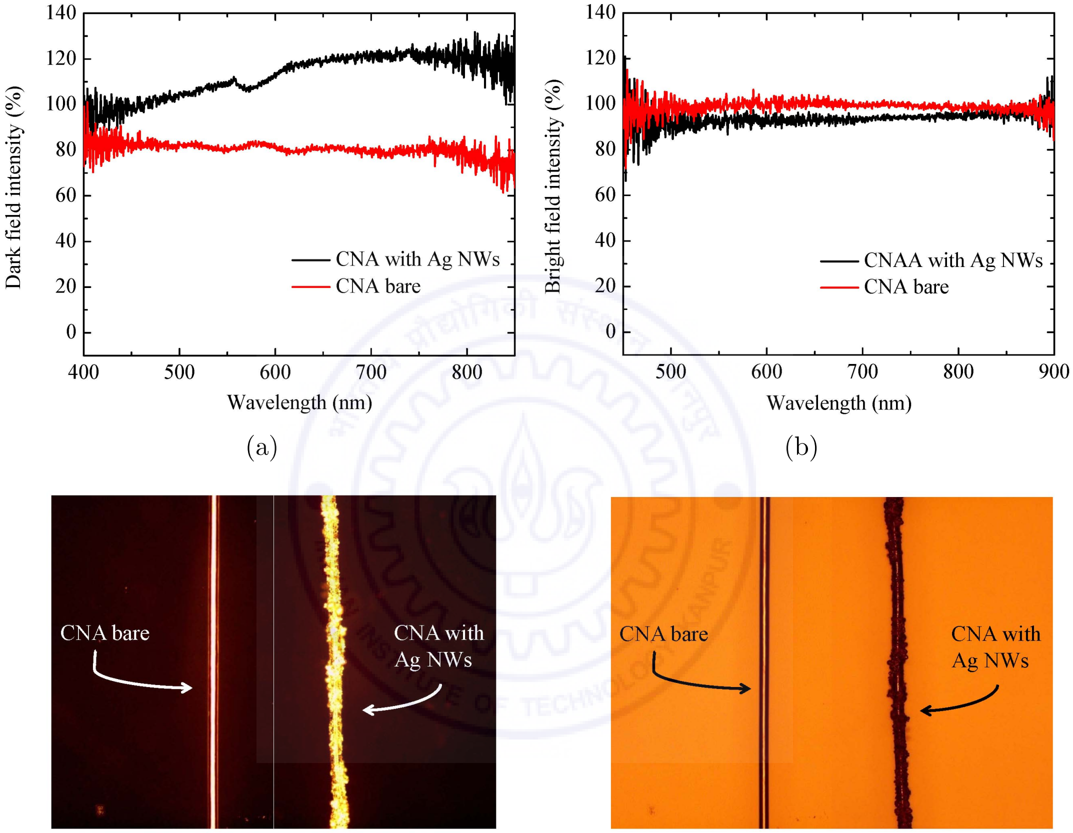

(a) (b)

(c) (d)

Figure 6.5: (a) The darkfield and (b) the brightfield spectra of silver nanowires (NWs) embedded cylindrical nanopoorus alumina (CNA). All the spectra had been normalized with an electropolished aluminium micro wire. (c) and (d) are the optical photograph of the bare CNA and silver nanowire embedded CNA in the darkfield and the brightfield mode respectively.

excitation of R6G is very much higher for green light than blue light. We see that when there are no nanowires in the alumina matrix then the signal is much larger than if there were nanowires in the alumina matrix. We believe that the fluorescent signal is quenched by the excitation of local surface plasmons on the silver nanowires to which the fluorescent light directly couples [140, 141]. For reference, we coated R6G on a plane electropolished aluminium micro wire. We see in Fig. 6.6 that the fluorescence signal from the R6G coated plane aluminium micro wire was also highly quenched. This is only a rough measure as the amount of R6G on the metal surface and the nanoporous alumina would be very different. A similar characteristic was also observed in the case of the planar nanoporous alumina [142]. This enhancing and quenching properties of R6G coated cylindrical nanoporous alumina can be potentially used for bio-sensors. The enhancement of the fluorescence signal for R6G doped cylindrical nanoporous alumina with respect to the R6G doped silver nanowires embedded cylindrical nanoporous alumina was nearly 900% higher for 488 nm wavelength while this enhancement was higher by 400% for 548 nm wavelength. The maximum fluorescence intensity of R6G doped cylindrical nanoporous alumina for 548 nm wavelength was nearly two times higher than maximum fluorescence intensity of R6G doped cylindrical nanoporous alumina for 488 nm wavelength.

6.4 Conclusions

In this chapter, we reported preliminary examination of the light scattering and fluorescence of dye doped nanoporous alumina in the planar and cylindrical geometries. Planar nanoporous alumina having linearly arranged nanopores were shown to effectively become anisotropic and the surface showed scattering that was sensitive to polarized light. The anisotropic planar nanoporous alumina with linearly organized pores show interesting polarization dependent scattering which has earlier been seen in random grating structures. This suggests that these system could be treated as random grating structures for theoretical analysis. Fluorescence from R6G molecules deposited on these scattering

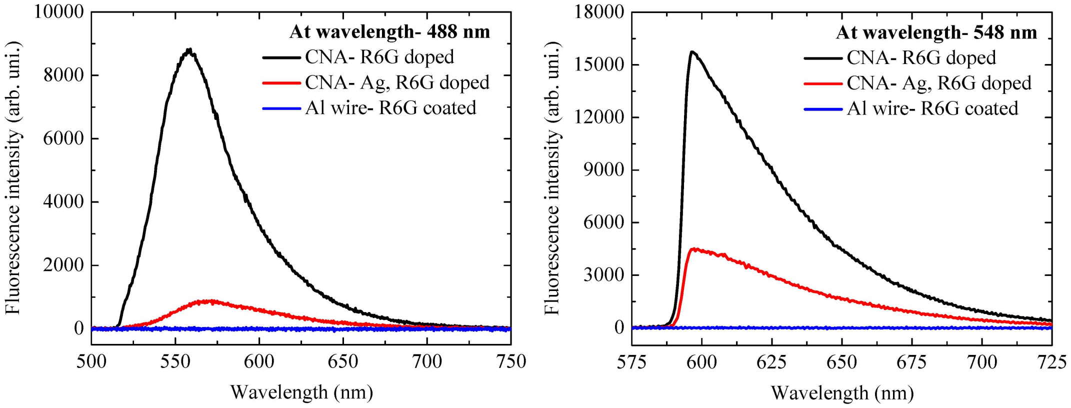

(a) (b)

Figure 6.6: Fluorescence spectra of R6G doped in cylindrical nanoporous alumina excited by (a) 488 nm wavelength and (b) 548 nm wavelength lights.

planar nanoporous alumina surfaces show a large enhancement, while fluorescence from R6G molecules deposited on gold coated planar nanoporous alumina surface was strongly quenched.

The darkfield and the brightfield scattering of the cylindrical nanoporous alumina with and without silver nanowires was studied. The darkfield spectra of silver nanowire embedded nanopoorus alumina had high signal levels and show a plasmonic resonance, while the bare cylindrical nanopoorus alumina show much lower levels of scattering as required for fiber applications. The brightfield scattering by the cylindrical nanoporous alumina with and without silver nanowires had reversed brightens levels as expected. The R6G doped cylindrical nanoporous alumina had enhanced fluorescence signals, while R6G doped cylindrical nanoporous alumina with silver nanowires embedded, quenched the fluorescence signal drastically.

Chapter 7

Summary and Future Directions

7.1 Summary

In this thesis, we presented a three dimensional cylindrical metamaterial made of nanoporous alumina, and nanotructured in the azimuthal and axial directions. We presented the details of its fabrication and the structural characterization. We found that the radially emanating nanopores size vary linearly with the radius of the metamaterial, making this metamaterial radially inhomogeneous and cylindrically anisotropic. We could also make a cylindrical nanowire medium by electrodepositing metal nanowires in the nanopores of the metamaterial. To the best of our knowledge, we believe such metamaterials with cylindrical anisotropy and wave propagation in these metamaterials have been studied here for the first time. We homogenized this cylindrical anisotropic metamaterial by using techniques of transformation optics and Maxwell-Garnett homogenization theory. We saw that this cylindrical metamaterial can also exhibit indefinite permittivity or the hyperbolic dispersion. This cylindrical nanoporous alumina can be used as waveguide or optical fiber that can be operated over a very wide range of frequencies, from the terahertz to the visible part of the electromagnetic spectrum. We investigated the light guiding properties of this anisotropic cylindrical metamaterial and found that in these waveguides, there exist some unique type of modes described byBessel functions with fractional and imaginary or even complex orders. These waveguides can support modes of large angular momentum and exhibit a high level of light confinement. In this waveguide there are frequency bands when backward wave propagation occurs. We also made preliminary studies of the light scattering on planar and cylindrical metamaterials and fluorescence from dye molecules coated on the planar as well as cylindrical metamaterials.

We have only studied the waveguide, light scattering and fluorescence properties of this cylindrical metamaterial. This newly developed system appear to have a plethora of properties and potential applications that need to be investigated in details in the future. In the next section, we shall discuss about the future uses and applications of the novel cylindrical metamaterials introduced in this thesis.

7.2 Future Directions

One very important result of the thesis was the discovery of waveguide modes in the cylindrical anisotropic system that are described by Bessel functions of imaginary orders. So we first discuss here what are the possible potential applications of the imaginary or complex order modes.

The special case in which the core is hollow but PEC boundary conditions at $r = R_2$ are maintained, is in fact, an anisotropic metamaterial-lined circular waveguide. When the metamaterial liner exhibits certain properties, e.g., a permittivity tensor containing negative and near-zero elements, these waveguides permit propagation well below their natural cutoff frequencies [98]. This has important applications in the miniaturization of microwave waveguide systems requiring access to the interior volume such as in fluid heating, electron-beam propagation, and traveling-wave magnetic-resonance imaging. As open-ended waveguide probe antennas, these structures may enable subwavelength spatial-resolution measurements with high efficiency in near-field antenna characterization [31]. We also note the case of TM modes with imaginary orders that have no cutoff frequency when $\varepsilon_z < 0$ and $\varepsilon_r > 0$, as then $\beta^2 = k_0^2\varepsilon_r + \varepsilon_r/|\varepsilon_z|k_\tau^2$ that are distinct from the quasi-static TEM mode.

The Bessel modes with imaginary orders or complex orders have enormous implications for coupling to the near-field modes of small sources as they have fast varying fields along both the radial and azimuthal directions localized near the center of the fiber. The subwavelength image resolution possible with near-field imaging by a hyperlens is also due to this effect [12,104]. Usually, one is able to couple light to the whispering gallery modes only though the cladding due to the localization of these modes at the edges. The Bessel modes with imaginary orders can enable a butt-coupling to the high order m modes to couple to the near-field modes of a radiating source. Further, these Bessel modes with imaginary orders occupy the entire cross section of the fibre and have implications for the amplification of these modes in the presence of gain media without spatial hole burning effects. The presence of plasmonic nanorods inside the medium results in large local electromagnetic fields that are crucial for nonlinear interactions. The guidance of fields within the fiber with large nonlinear interactions has immense implications for effects like super-continuum generation due to dispersion of ultra-short pulses. The enormous surface areas available within the nanopores for adsorbing molecules coupled with the fiber geometry and resonant modes makes this system highly suitable for sensor applications. In case of hollow core fibers, liquids can be flown through the central microtube and the enhanced fields of the higher order m modes localized near the center could be a very useful for detecting molecules in the liquids.

With respect to the optical characterization of the cylindrical nanoporous alumina as an optical fiber, we have shown only the laser light transmission/output. The fabrication process developed yields waveguides with imperfections and cracks which appears to create large scattering, thereby preventing single mode excitation in the fiber. Thus the new fiber modes predicted by us are yet to be imaged and confirmed. Further optical characterization for attenuation, coupling etc. still remains and is a good area for further study. This thesis discusses the fabrication of cylindrical nanoporous alumina at some fixed parameters. But these parameters need to be optimized well for achieving high quality nanoporous microwires as well as some other purposes too. The inverse replica of the cylindrical nanoporous alumina with metal or polymer is also possible. Radially emanating plasmonic nanowires may form a nice sensor materials.

One very nice point is that the nanopores of cylindrical nanoporous alumina can be filled with a variety of materials to investigate other physical phenomena or applications. Because of the nanopopores, the surface area of cylindrical nanoporous alumina becomes very large and the microwires can be very useful for heat exchanging at micron level which is studied by our collaborators [143]. This was made by anodizing an aluminium microwire to get a nanoporous alumina shell at outer side. The experiment was done in a water boiling chamber. The heat transfer coefficient was enhanced due to the nanopores. The heat transfer coefficient can be enhanced also by coating of nanowires of very high thermal conductive materials, such as metals, using the nanoporous alumina on the aluminium microwire. Using the nanowires on heat exchanger, the effective surface area will increase and if nanowires made of high conductivity materials then its heat exchanging capacity can be enhanced enormously. There are other elements, such as silicon, zinc, titanium etc., might be used in place of aluminium.

By removing the aluminium core, we obtained hollow nanoporous alumina micro tubes. These micro tubes can be used as novel micro fluidic devices with very large nanoporous surface area. The nanoporous alumina microtubes are the good candidates for bio-sensors with appropriate fictionalization of their surfaces.

The anodization is a highly established technique and widely used in research and industrial purposes. It is a simple and good tool to make the various nanomaterials and the hyperbolic metamaterials for research and new technological applications. Using the anodization technique, various types of surface texturing can be obtained and even super-hydrophilic and super-hydrophobic surfaces can be made [144, 145]. The large surface area available the planar nanoporous alumina can also be used in thermal engineering. It makes for a very good heat exchanger. It changes the condensation and the evaporation behavior of a liquid on the surface depending on the porous nature. The thermal properties have been found by us to also depend on the organization of the nanopores [142]. The planar nanoporous alumina is being used in gas sensing and chemical sensing too. Like the nanowire coating on the cylindrical nanoporous alumina, the nanowires can be grown on the planar nanoporous alumina also to increase the thermal properties. It is noted that the deposition of nanowires on the planar nanoporous alumina is easier than the cylindrical nanoporous alumina.

Finally, there are other several metals such as silicon, zinc, magnesium, tantalum etc. which can be anodized. The different types of anodized metals are used in different applications. Particularly, nanoporous silicon and titanium may make for some wonderful applications. Anodization technique also used in coloring, resistible surface, cleaning etc. It is an environment friendly very good technique for metal finishing and recycling. This method is now days used to make heat efficient household tools too.


भारतीय प्रौद्योगिकी संस्थान कानपुर
INDIAN INSTITUTE OF TECHNOLOGY KANPUR

Bibliography

[1] M. J. Weber, *Handbook of Optical Materials*, 1st ed. (CRC Press, USA, 2003).

[2] A. K. Ghatak and K. Thyagarajan, *Optical Electronics* (Cambridge University Press, New Delhi, 1989).

[3] P. Y. Amnon Yariv, *Optical Waves in Crystals: Propagation and Control of Laser Radiation* (John Wiley, USA, 2002).

[4] A. Yariv, *Optical Electronics* (Oxford University Press, Virginia, 1990).

[5] A. Ghatak, *Optics* (McGraw-Hill, New Delhi, 2005).

[6] F. Capolino, *Metamaterials Handbook* (CRC Press, USA, 2009).

[7] S. A. Ramakrishna and T. M. Grzegorczyk, *Physics and Applications of Negative Refractive Index Materials*, 1st ed. (CRC Press, New York, 2009).

[8] W. Cai and V. Shalaev, *Optical Metamaterials: Fundamentals and Applications*, 1st ed. (Springer, New York, USA, 2010).

[9] D. R. Smith and D. Schurig, Phys. Rev. Lett. **90**, 077405 (2003).

[10] J. B. Pendry, A. J. Holden, W. J. Stewart, and I. Youngs, Phys. Rev. Lett. **76**, 4773 (1996).

[11] J. B. Pendry, A. J. Holden, D. J. Robbins, and W. J. Stewart, Journal of Physics: Condensed Matter **10**, 4785 (1998).

[12] Z. Liu, H. Lee, Y. Xiong, C. Sun, and X. Zhang, Science **315**, 1686 (2007).

[13] H. Lee, Z. Liu, Y. Xiong, C. Sun, and X. Zhang, Opt. Express **15**, 15886 (2007).

[14] Y. Huang, Y. Feng, and T. Jiang, Opt. Express **15**, 11133 (2007).

[15] S. Schwaiger, A. Rottler, M. Bröll, J. Ehlermann, A. Stemmann, D. Stickler, C. Heyn, D. Heitmann, and S. Mendach, Phys. Rev. B **85**, 235309 (2012).

[16] D. Schurig, J. J. Mock, B. J. Justice, S. A. Cummer, J. B. Pendry, A. F. Starr, and D. R. Smith, Science **314**, 977 (2006).

[17] W. Cai, U. K. Chettiar, A. V. Kildishev, and V. M. Shalaev, Nature photonics **1**, 224 (2007).

[18] A. Rottler, B. Krüger, D. Heitmann, D. Pfannkuche, and S. Mendach, Phys. Rev. B **86**, 245120 (2012).

[19] M. Born, E. Wolf, A. Bhatia, D. Gabor, A. Stokes, A. Taylor, P. Wayman, and W. Wilcock, *Principles of Optics: Electromagnetic Theory of Propagation, Interference and Diffraction of Light* (Cambridge University Press, UK, 2000).

[20] W. J. Padilla, M. T. Aronsson, C. Highstrete, M. Lee, A. J. Taylor, and R. D. Averitt, Phys. Rev. B **75**, 041102 (2007).

[21] H. Chen, W. J. Padilla, J. M. O. Zide, S. R. Bank, A. C. Gossard, A. J. Taylor, and R. D. Averitt, Opt. Lett. **32**, 1620 (2007).

[22] H. Chen, J. F. O'Hara, A. J. Taylor, R. D. Averitt, C. Highstrete, M. Lee, and W. J. Padilla, Opt. Express **15**, 1084 (2007).

[23] F. J. Garcia-Vidal, L. Martn-Moreno, and J. B. Pendry, Journal of Optics A: Pure and Applied Optics **7**, S97 (2005).

[24] A. K. Sarychev and G. Tartakovsky, Phys. Rev. B **75**, 085436 (2007).

[25] D. Artigas and L. Torner, Phys. Rev. Lett. **94**, 013901 (2005).

[26] S. Linden, C. Enkrich, G. Dolling, M. Klein, J. Zhou, T. Koschny, C. Soukoulis, S. Burger, F. Schmidt, and M. Wegener, Selected Topics in Quantum Electronics, IEEE Journal of **12**, 1097 (2006).

[27] G. Dolling, M. Wegener, C. M. Soukoulis, and S. Linden, Opt. Express **15**, 11536 (2007).

[28] J. Yao, Z. Liu, Y. Liu, Y. Wang, C. Sun, G. Bartal, A. M. Stacy, and X. Zhang, Science **321**, 930 (2008).

[29] P. Russell, Science **299**, 358 (2003).

[30] C. Fan, C. Chiang, and C. Yu, Optics express **19**, 19948 (2011).

[31] S. Hrabar, J. Bartolic, and Z. Sipus, IEEE Transactions on Antennas and Propagation **53**, 110 (2005).

[32] J. G. Pollock and A. K. Iyer, IEEE Transactions on Microwave Theory and Techniques **61**, 3169 (2013).

[33] A. V. Novitsky and L. M. Barkovsky, Journal of Optics A: Pure and Applied Optics **7**, S51 (2005).

[34] A. V. Novitsky, Journal of Optics A: Pure and Applied Optics **8**, 864 (2006).

[35] H. Cory and T. Blum, Microwave and Optical Technology Letters **44**, 31 (2005).

[36] B. Ghosh and A. B. Kakade, Electromagnetics **32**, 465 (2012).

[37] E. J. Smith, Z. Liu, Y. Mei, and O. G. Schmidt, Nano Letters **10**, 1 (2010), pMID: 19368372.

[38] M. Yan, N. Mortensen, and M. Qiu, Frontiers of Optoelectronics in China **2**, 153 (2009).

[39] S. Atakaramians, A. Argyros, S. C. Fleming, and B. T. Kuhlmey, J. Opt. Soc. Am. B **29**, 2462 (2012).

[40] S. Atakaramians, A. Argyros, S. C. Fleming, and B. T. Kuhlmey, J. Opt. Soc. Am. B **30**, 851 (2013).

[41] N. Singh, A. Tuniz, R. Lwin, S. Atakaramians, A. Argyros, S. C. Fleming, and B. T. Kuhlmey, Opt. Mater. Express **2**, 1254 (2012).

[42] H. Masuda and K. Fukuda, Science **268**, 1466 (1995).

[43] A. Santos, T. Kumeria, and D. Losic, Materials **7**, 4297 (2014).

[44] O. Jessensky, F. Müller, and U. Gösele, Applied Physics Letters **72**, 1173 (1998).

[45] H. Masuda, H. Yamada, M. Satoh, H. Asoh, M. Nakao, and T. Tamamura, Applied Physics Letters **71**, (1997).

[46] S. Shingubara, J. Nanoparticle Research **5**, 17 (2003).

[47] G. Sauer, G. Brehm, S. Schneider, K. Nielsch, R. Wehrspohn, J. Choi, H. Hofmeister, and U. Gösele, Journal of Applied Physics **91**, 3243 (2002).

[48] X. Zhao, S. Seo, U. Lee, and K. Lee, Journal of The Electrochemical Society **154**, C553 (2007).

[49] P. Forrer, F. Schlottig, H. Siegenthaler, and M. Textor, Journal of Applied Electrochemistry **30**, 533 (2000).

[50] G. Sharma, M. Pishko, and C. Grimes, Journal of Materials Science **42**, 4738 (2007).

[51] J. Yao, Y. Wang, K. Tsai, Z. Liu, X. Yin, G. Bartal, A. M. Stacy, Y. Wang, and X. Zhang, Philosophical Transactions of the Royal Society of London A: Mathematical, Physical and Engineering Sciences **369**, 3434 (2011).

[52] E. Matei, C. Florica, A. Costas, M. E. Toimil-Molares, and I. Enculescu, Beilstein Journal of Nanotechnology **6**, 444 (2015).

[53] B. D. F. Casse, W. T. Lu, Y. J. Huang, E. Gultepe, L. Menon, and S. Sridhar, Applied Physics Letters **96**, (2010).

[54] M. Sadiku, *Elements of Electromagnetics*, *The Oxford series in electrical and computer engineering* (Oxford University Press, USA, 2014).

[55] M. Larson and F. Bengzon, *The Finite Element Method: Theory, Implementation, and Applications*, *Texts in Computational Science and Engineering* (Springer Berlin Heidelberg, Germany, 2013).

[56] A. Greenbaum, *Iterative Methods for Solving Linear Systems*, *Frontiers in Applied Mathematics* (Society for Industrial and Applied Mathematics, USA, 1997).

[57] A. Ghali, A. Neville, and T. Brown, *Structural Analysis: A Unified Classical and Matrix Approach* (Taylor & Francis, NY, 2003).

[58] T. A, J. Volakis, and I. of Electrical Engineers, *Approximate Boundary Conditions in Electromagnetics*, *IEE Publication Series* (Institution of Electrical Engineers, UK, 1995).

[59] M. Sadiku, *Numerical Techniques in Electromagnetics, Second Edition* (Taylor & Francis, USA, 2000).

[60] A. Datta and V. Rakesh, *An Introduction to Modeling of Transport Processes: Applications to Biomedical Systems*, *An Introduction to Modeling of Transport Processes: Applications to Biomedical Systems* (Cambridge University Press, UK, 2010).

[61] M. Fiddy and R. Ritter, *Introduction to Imaging from Scattered Fields* (Taylor & Francis, USA, 2014).

[62] C. Balanis, *Advanced Engineering Electromagnetics*, *CourseSmart Series* (Wiley, USA, 2012).

[63] F. Li, L. Zhang, and R. M. Metzger, Chemistry of Materials **10**, 2470 (1998).

[64] W. Lee, K. Nielsch, and U. Gösele, Nanotechnology **18**, 475713 (2007).

[65] S. Niwa, M. Eswaramoorthy, J. Nair, A. Raj, N. Itoh, H. Shoji, T. Namba, and F. Mizukami, Science **295**, 105 (2002).

[66] T. Mizushima, K. Matsumoto, J. Sugoh, H. Ohkita, and N. Kakuta, Applied Catalysis A: General **265**, 53 (2004).

[67] W. Chae, S. Im, J. Lee, and Y. Kim, Bulletin of the Korean Chemical Society **26**, 409 (2005).

[68] Y. W. Wang, L. D. Zhang, G. W. Meng, X. S. Peng, Y. X. Jin, and J. Zhang, The Journal of Physical Chemistry B **106**, 2502 (2002).

[69] S. Ono, M. Saito, and H. Asoh, Electrochimica Acta **51**, 827 (2005).

[70] A. K. Kasi, J. K. Kasi, N. Afzulpurkar, M. M. Hasan, and B. Mahaisavariya, Journal of Vacuum Science & Technology B **30**, 031805 (2012).

[71] J. Choi, G. Sauer, K. Nielsch, R. B. Wehrspohn, , and U. Gösele, Chem. Mater. **15**, 776 (2003).

[72] A. Maria Chong, L. K. Tan, J. Deng, and H. Gao, Advanced Functional Materials **17**, 1629 (2007).

[73] J. Choi, Y. Luo, R. B. Wehrspohn, R. Hillebrand, J. Schilling, and U. Gösele, Journal of Applied Physics **94**, 4757 (2003).

[74] C. Liu, A. Datta, and Y. Wang, Applied Physics Letters **78**, 120 (2001).

[75] N. Liu, A. Datta, C. Liu, and Y. Wang, Applied Physics Letters **82**, 1281 (2003).

[76] J. D. Jackson, *Classical Electrodynamics* (Wiley India, New Delhi, 2011).

[77] L. Yi, L. Zhiyuan, H. Xing, L. Yisen, and C. Yi, RSC Adv. **2**, 5164 (2012).

[78] J. Yao, K. Tsai, Y. Wang, Z. Liu, G. Bartal, Y. Wang, and X. Zhang, Opt. Express **17**, 22380 (2009).

[79] W. S. W. A. Lakhtakia, *Introduction to Complex Mediums for Optics and Electromagnetics*, 1st ed. (SPIE Press, Washington, USA, 2003).

[80] V. A. Podolskiy and E. E. Narimanov, Phys. Rev. B **71**, 201101 (2005).

[81] Y. Liu, G. Bartal, and X. Zhang, Opt. Express **16**, 15439 (2008).

[82] W. S. Weiglhofer, A. Lakhtakia, and B. Michel, Microwave and Optical Technology Letters **15**, 263 (1997).

[83] A. Lakhtakia, Microwave and Optical Technology Letters **17**, 276 (1998).

[84] T. G. Mackay and A. Lakhtakia, Optics communications **234**, 35 (2004).

[85] T. G. Mackay, Electromagnetics **25**, 461 (2005).

[86] A. J. Ward and J. B. Pendry, Journal of Modern Optics **43**, 773 (1996).

[87] J. B. Pendry, D. Schurig, and D. R. Smith, Science **312**, 1780 (2006).

[88] D. Pratap, S. A. Ramakrishna, J. G. Pollock, and A. K. Iyer, Opt. Express **23**, 9074 (2015).

[89] S. Chakrabarti, S. A. Ramakrishna, and H. Wanare, Opt. Lett. **34**, 3728 (2009).

[90] J. Elser, R. Wangberg, V. A. Podolskiy, and E. E. Narimanov, Applied Physics Letters **89**, (2006).

[91] J. Pendry, Opt. Express **11**, 755 (2003).

[92] C. F. Bohren and D. R. Huffman, *Absorption and scattering of light by small particles*, 1st ed. (John Wiley, New York, USA, 1983).

[93] R. C. Jones, Phys. Rev. **68**, 93 (1945).

[94] A. Nicolet, F. Zolla, Y. O. Agha, and S. Guenneau, COMPEL - The international journal for computation and mathematics in electrical and electronic engineering **27**, 806 (2008).

[95] F. Zolla, G. Renversez, A. Nicolet, B. Kuhlmey, S. Guenneau, D. Felbacq, A. Argyros, and S. Leon-Saval, *Foundations of Photonic Crystal Fibres*, 1st ed. (Imperial College Press, Londan, 2008).

[96] M. Farhat, S. Enoch, S. Guenneau, and A. B. Movchan, Phys. Rev. Lett. **101**, 134501 (2008).

[97] A. Ghatak and K. Thyagarajan, *An Introduction To Fiber Optics*, 1st ed. (Cambridge University Press, New Delhi, India, 1998).

[98] J. Pollock and A. Iyer, Antennas and Wireless Propagation Letters, IEEE **10**, 1491 (2011).

[99] T. M. Dunster, SIAM Journal on Mathematical Analysis **21**, 995 (1990).

[100] C. J. Chapman, Proceedings of the Royal Society of London A: Mathematical, Physical and Engineering Sciences (2012).

[101] R. Grimshaw, K. Khusnutdinova, and L. Ostrovsky, European Journal of Mechanics - B/Fluids **27**, 24 (2008).

[102] G. Arfken, H. Weber, and F. Harris, *Mathematical Methods for Physicists: A Comprehensive Guide* (Elsevier, UK, 2012).

[103] F. Olver, N. I. of Standards, and T. (U.S.), *NIST Handbook of Mathematical Functions* (Cambridge University Press, USA, 2010).

[104] Z. Jacob, L. V. Alekseyev, and E. Narimanov, Opt. Express **14**, 8247 (2006).

[105] K. Z. Rajab, M. Naftaly, E. H. Linfield, J. C. Nino, D. Arenas, D. Tanner, R. Mittra, and M. Lanagan, Journal of microelectronics and electronic packaging **5**, 2 (2008).

[106] M. Ordal, L. Long, R. Bell, S. Bell, R. Bell, R. Alexander, and C. Ward, Applied Optics **22**, 1099 (1983).

[107] G. Keiser, *Optical Fiber Communications*, 4th ed. (Tata McGraw-Hill Education, New Delhi, India, 2008).

[108] M. S. Sodha and A. K. Ghatak, *Inhomogeneous Optical Waveguides*, 1st ed. (Plenum Press, New York, USA, 1977).

[109] C. Kurtz and W. Streifer, IEEE Transactions on Microwave Theory and Techniques **17**, 11 (1969).

[110] C. Yeh, K. Ha, S. B. Dong, and W. P. Brown, Appl. Opt. **18**, 1490 (1979).

[111] Y. Lu and F. Fernandez, IEEE Transactions on Microwave Theory and Techniques **41**, 1215 (1993).

[112] L. Valor and J. Zapata, IEEE Transactions on Microwave Theory and Techniques **43**, 2452 (1995).

[113] H. Lin and P. Palffy-Muhoray, Opt. Lett. **17**, 722 (1992).

[114] A. Ferrando, M. Zacares, P. F. de Cordoba, D. Binosi, and J. Monsoriu, Opt. Express **11**, 452 (2003).

[115] L. Cui, X. Li, and N. Zhao, Phys. Rev. A **85**, 023825 (2012).

[116] M. Dalarsson, M. Norgren, and Z. Jaksic, Progress In Electromagnetics Research **151**, 109 (2015).

[117] H. Uchi, T. Kanno, and R. Alwitt, Journal of the Electrochemical Society **148**, B17 (2001).

[118] T. Masuda, H. Asoh, S. Haraguchi, and S. Ono, Materials **8**, 1350 (2015).

[119] A. Lutich, M. Danailov, S. Volchek, V. Yakovtseva, V. Sokol, and S. Gaponenko, Applied Physics B **84**, 327 (2006).

[120] S. Green, A. Cortes, G. Riveros, H. Gmez, E. A. Dalchiele, and R. E. Marotti, Physica Status Solidi (c) **4**, 340 (2007).

[121] C. J. Ingham, J. ter Maat, and W. M. de Vos, Biotechnology Advances **30**, 1089 (2012).

[122] A. Santos, V. S. Balderrama, M. Alba, P. Formentn, J. Ferr-Borrull, J. Pallars, and L. F. Marsal, Advanced Materials **24**, 1050 (2012).

[123] S. S. Penumetcha, R. Kona, J. L. Hardin, A. L. Molder, and E. D. Steinle, Sensors **7**, 2942 (2007).

[124] K. E. L. Flamme, K. C. Popat, L. Leoni, E. Markiewicz, T. J. L. Tempa, B. B. Roman, C. A. Grimes, and T. A. Desai, Biomaterials **28**, 2638 (2007).

[125] K. C. Popat, K.-I. Chatvanichkul, G. L. Barnes, T. J. Latempa, C. A. Grimes, and T. A. Desai, Journal of Biomedical Materials Research Part A **80A**, 955 (2007).

[126] J. Xu, J. Xia, J. Wang, J. Shinar, and Z. Lin, Applied Physics Letters **89**, (2006).

[127] A. B. Movchan, N. V. Movchan, S. Guenneau, and R. C. McPhedran, Proc. Roy. Soc. A **463**, 1045 (2007).

[128] W. Cao, N. Huang, S. H. N. Xu, and H. E. Elsayed-Ali, J. Appl. Phys. **109**, 34310 (2011).

[129] Y. Song, P. D. Nallathamby, T. Huang, H. E. Elsayed-Ali, and X. H. N. Xu, J. Phys. Chem. C **114**, 74 (2010).

[130] A. A. Maradudin and T. Michel, Annals of Physics **203**, 255 (1990).

[131] V. Celli, A. A. Maradudin, A. M. Marvin, and A. R. McGurn, J. Opt. Soc. Am. A **2**, 2225 (1985).

[132] A. R. McGurn, A. A. Maradudin, and V. Celli, Phys. Rev. B **31**, 4866 (1985).

[133] A. A. Maradudin, E. R. Mendez, and T. Michel, Opt. Lett. **14**, 151 (1989).

[134] A. R. McGurn and A. A. Maradudin, J. Opt. Soc. Am. B **4**, 910 (1987).

[135] H. Cao, J. Phys. A: Math. Gen. **38**, 10497 (2005).

[136] G. Schneider, G. Decher, N. Nerambourg, R. Praho, M. H. V. Werts, and M. B. Desce, Nano Lett. **6**, 530 (2006).

[137] J. R. Lakowicz, J. Malicka, S. DAuria, and I. Gryczynski, Analytical Biochemistry **320**, 13 (2003).

[138] V. N. Pustovit and T. V. Shahbazyan, J. Chem. Phys. **136**, 204701 (2012).

[139] P. Mandal, P. Gupta, A. Nandi, and S. A. Ramakrishna, Journal of Nanophotonics **6**, 10497 (2012).

[140] E. Dulkeith, A. C. Morteani, T. Niedereichholz, T. A. Klar, J. Feldmann, S. A. Levi, F. C. J. M. van Veggel, D. N. Reinhoudt, M. Möller, and D. I. Gittins, Phys. Rev. Lett. **89**, 203002 (2002).

[141] P. Anger, P. Bharadwaj, and L. Novotny, Phys. Rev. Lett. **96**, 113002 (2006).

[142] S. K. Singh, S. Khandekar, D. Pratap, and S. A. Ramakrishna, Colloids and Surfaces A: Physicochemical and Engineering Aspects **432**, 71 (2013).

[143] M. Arya, S. Khandekar, D. Pratap, and S. A. Ramakrishna, Heat and Mass Transfer **Accepted, DOI 10.1007/s00231-015-1692-2**, .

[144] C. Ran, G. Ding, W. Liu, Y. Deng, and W. Hou, Langmuir **24**, 9952 (2008), pMID: 18702472.

[145] R. Liao, Z. Zuo, C. Guo, Y. Yuan, and A. Zhuang, Applied Surface Science **317**, 701 (2014).